ALMA MATER STUDIORUM · UNIVERSITÀ DI BOLOGNA

Scuola di Scienze
Corso di Laurea Magistrale in Fisica del Sistema Terra

Topographic and geomorphologic modeling and analysis of the bedrock surface beneath Ultimi Lobe ice-cap (South Pole, Mars) using MARSIS high-resolution data.

Relatore:

Prof. Andrea Morelli

Presentata da:

Giacomo Di Silvestro

Correlatori:

Prof. Roberto Orosei

Dott. Luca Guallini

Sessione III

Anno Accademico 2019/2020

ABSTRACT

Lo scopo del presente lavoro è stato quello di definire la topografia e le principali morfologie del basamento roccioso al di sotto di una porzione, Ultimi Lobe (UL), della calotta polare meridionale di Marte. Tramite l'analisi dei radargrammi MARSIS per mezzo di una procedura di mappatura semi-automatica sviluppata in MATLAB, è stato possibile ricavare i dati altimetrici della superficie subglaciale in questione. Successivamente, attraverso il metodo di interpolazione noto come Natural Neighbor (Sibson, 1981), è stato possibile creare in ambiente software ESRI ArcGIS un modello di elevazione digitale della superficie.

Quest'ultima ha permesso un'analisi innovativa delle geomorfologie presenti sul basamento della calotta polare al fine di comprenderne i processi geologici di formazione, l'eventuale correlazione tra ciò che viene osservato in superficie e quanto già scoperto alla base della calotta polare (vedi regione dei laghi; Orosei et al., 2018) e, infine, i possibili eventi che hanno caratterizzato la suddetta porzione del ghiacciaio in periodi remoti. In particolare, i risultati ottenuti hanno contribuito: 1) A fornire nuove prove sull'origine tettonica di alcune morfologie superficiali note come Large Asymmetric Polar Scarps (LAPS; Grima et al., 2011); 2) A descrivere ed analizzare possibili morfologie glaciali; 3) Ad individuare in corrispondenza del lago subglaciale individuato da Orosei et al. (2018) una serie di alti e bassi topografici funzionali al contenimento d'acqua.

Tutti questi elementi suggeriscono un lento scorrimento di parte della calotta glaciale di UL in tempi remoti, forse favorito da un flusso di acqua di fusione alla sua base come la rete di laghi subglaciali scoperta da Orosei et al. (2018) e Lauro et al. (2021) sembrerebbe suggerire. Questi ultimi, infatti, potrebbero essere ciò che rimane di più ampi deflussi passati.

SUMMARY

1 INTRODUCTION

Human curiosity has always brought people to look at the night sky and wonder what there could be above our heads and what is our place in this vast sea of emptiness that we called the Universe. This search for an understanding has accompanied Humankind since the dawn of civilization all around the globe. The first moon landing was not only a technological success but also a giant evolutionary leap that humanity achieved as a species. Preparing the ground for the next space exploration is the first task to complete to see Humankind leaving its cradle and cooperating under the same flag. Mars is our closest neighbor with similar properties to the Earth, being not only a suitable candidate for a hypothetical colony but a window for a better understanding of our planet and the solar system. Its current state may shed light on eventual future problems that could strike Earth, whether for natural or anthropic reasons. Therefore, understanding its evolution is critical either for both to predict a possible change in climatic and geological conditions that may occur on Earth, and thus prevent problems related to it, and to better understand geological and physical mechanisms that we are not yet able to explain or fully understand. The technological discoveries that research in the space field has brought have found application in the most diverse fields, offering a significant contribution even in those disciplines distantly related to it. The benefits that space exploration has brought, and those that it promises to bring, have led several nations to invest in it. The number of missions launched towards the Red Planet in the last decades has reached remarkable dimensions, seeing the entry into the game also of China, India, and Arabs Emirates. The economic potential present in space research has also led private companies to join the table of contributors, becoming the visionary protagonists of what could be the same story that more than 500 years ago has radically changed the geopolitical situation of the Earth. It is not clear what could be the new Palos of the XXI century, and little we care, but the premises that bring with them a possible (but I dare to define, even for idealistic spirit, certain) success of Mars colonization plans are revolutionary. The changes that this event promises to bring about are not only economic, social, and technological, but also philosophical and existential. Recent discoveries made below the Martian south polar cap, which will be mentioned several times later in this paper, are nothing short of amazing. The presence of a network of subglacial lakes (Orosei et al. 2018 and Lauro et al. 2021) in a hostile environment, characterized by extreme physical conditions, ignites a glimmer of hope regarding the possibility of finally answering one of the most complex questions that have accompanied humankind for millennia: are we the only

sailors adrift in interstellar space aboard a gravitational prison, or is our existence not something so unique and rare? It is clear that if it is shown that not only the conditions that have allowed the existence of these bodies of water also support the existence of complex molecules, but that these conditions are even found in multiple places on the planet, the discovery of extraterrestrial life forms would not be so unlikely. On the tail of these recent discoveries, the main aim of the present work is to provide a better understanding of the topographic, morphological, and geological context of the buried region located under the south polar ice-cap and encompassing the water reservoirs defined by Orosei et al. (2018) and Lauro et al. (2021) based on radar permittivity. In particular, using selected orbits collected by the MARSIS radar instrument aboard the European probe Mars Express, net of the limitations imposed by the instrument, by the data density, and by the processing algorithms, we defined a three-dimensional model of the bedrock underlying a portion of the ice-sheet known as Ultimi Lobe. This model facilitates the identification of peculiar geomorphologies, allowing us to give a plausible interpretation of the possible causes and events that led to the formation of these structures and, thus, to give a valid interpretation, under a strict geological point of view, on the origin of the subglacial lakes of Orosei et al. (2018). To achieve this purpose, several processing and interpretational steps have been necessary, starting from the writing of a code in MATLAB for the analysis and recovery of data from radargrams collected by MARSIS. Through that, we calculated the elevation of the basal surface of the cap in the points where the probe has made sampling. We then proceeded with the interpolation of the data to create a georeferenced map aimed at studying the topographic and morphological properties that characterize the buried bedrock surface. This allowed us to identify geological structures probably related to past glacial movements and basal melting, and also to define a series of basins and depressions consistent with the accumulation of subglacial lakes (in contrast with the conclusions of previous authors, i.e., Arnold et al., 2019 and Sori and Branson, 2019, suggesting local thermal anomalies). Among those, the study also helped to understand the origin of some structures in UL known as LAPS and studied by Grima et al (2011).

Schematically, the present manuscript has been organized:

- Describing the geological context of Mars and the Martian poles, along with the description of the physical properties of the planet and the most important missions and instruments by NASA and ESA.

- Describing the geodetic techniques and instruments used in the space missions that enabled the collection of the data used in the present work.
- Describing and analyzing the used software and algorithms, the data, and the methodologies used.
- Analyzing and interpreting the topography, geomorphology, and geology of the modeled bedrock surface in comparison with what is observed at the surface and on Earth in similar environments.

2 MARS PHYSICAL PROPERTIES

2.1 GEOPHYSISCAL MEASUREMENTS AND ORBITAL PARAMETERS

The orbit of a body around a center of mass is described in geodesy by six Keplerian parameters, three accounting for the orientation of the orbit and three for its dimension and shape (the sixth parameter is the current position of the object in the orbit in a specific instant of time expressed as the fraction of the orbital period) [Tab. 1].

Tab. 1 Orbital properties of Mars

Semimajor axis	2.2792×10^{8} km
Eccentricity	0.0933941
Inclination	1.84969142
Longitude of ascending node	49.55953891°
Longitude of perihelion	336.0563704°
Sideral orbital period	686.98 days
Synodic orbital period	779.94 days
Mean orbital velocity	24.13 km s^{-1}
Maximum orbital velocity	26.50 km s^{-1}
Minimum orbital velocity	21.97 km s^{-1}
Obliquity	25.19°
Perihelion	2.066×10^{8} km
Aphelion	2.492×10^{8} km

Source: JPL Solar System Dynamics page: ssd.jpl.nasa.gov/ and NSSDC Mars Fact Sheet: nssdc.gsfc.nasa.gov/planetary/factsheet/marsfact.html

Mars is the fourth planet from the sun with a distance of 2.2792×10^{8} km (semimajor axis). The shape of the orbit, as suggested by the eccentricity ‘e’, is not perfectly a circle but rather an ellipse, characterized by a minor and a minor axis orthogonal to each other.

$$e = \frac{\sqrt{a^2 - b^2}}{a} \quad (1)$$

$$e' = \frac{\sqrt{a^2 - b^2}}{b} \quad (2)$$

$$f = \frac{a - b}{a} \quad (3)$$

with a=semimajor axis and b=semiminor axis, f=flattening

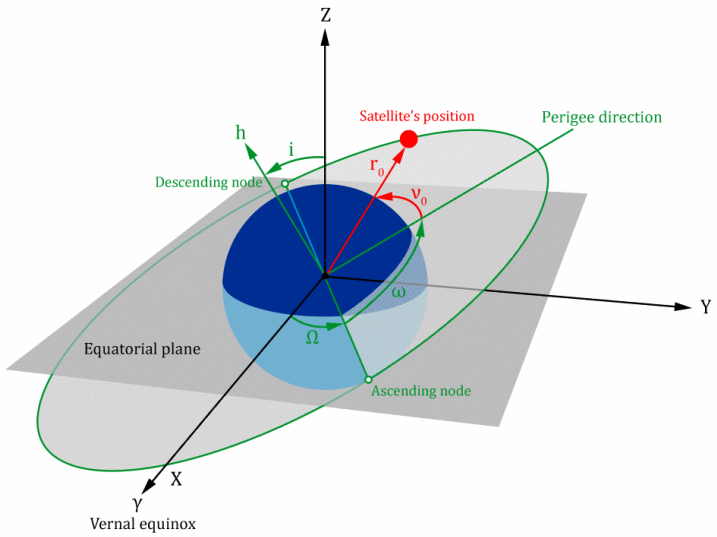

Figure 1 Keplerian parameters

source: https://it.mathworks.com/matlabcentral/fileexchange/72098-keplerian-orbit

A Martian year corresponds to 686.98 Earth days and a sidereal day is 24h 37m 22.65s, slightly longer than the terrestrial period of 23h 56m 4.09s. Due to the oblateness of the orbits and the obliquity of the rotational axis, the Mars surface is subject to change in the degree insolation. For the vernal equinox, first day of spring in the northern hemisphere, the longitude of the Sun (L_s) as seen from Mars is L_s=0°. Northern hemisphere summer solstice occurs at L_s=90°, northern autumnal equinox is at L_s=180°, and northern winter solstice occurs at L_s=270° (Carr, 1981). The southern hemisphere experiences warmer summer than the northern cause the perihelion (position of maximum proximity to the Sun) occurs near L_s=250° near the summer solstice and as a consequence,

a colder winter. During the cold seasons, Mars atmosphere start to condensate on the poles, forming the seasonal caps thanks to the precipitation of CO_2 ice with smaller amounts of H_2O ice and dust. Activity begins around L_s=185° for the northern hemisphere, during the autumnal equinox, and near L_s=50° for the southern hemisphere, mid-autumn (Dollfus et al., 1996), and becomes visible near L_s=10° in the north and L_s=180° in the south. Image 3 and 2 shows thickness and precipitation variations.

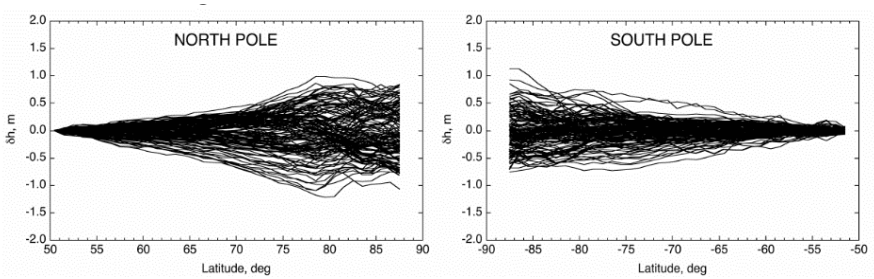

Figure 3 Elevation residuals referenced to 50N & S. The figure, obtained from the MOLA data, shows ~160 profiles in each hemisphere of the mean residual in each 1-degree latitude band.

Source: Smith & Zuber, 2018

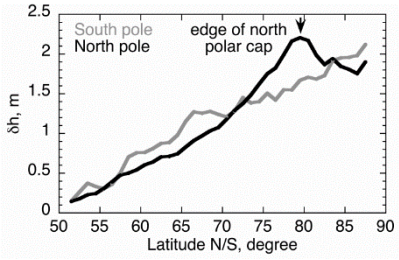

Figure 2 Maximum accumulation of CO_2 vs latitude. The average increase in depth is ~5 cm/degree. The maximum depth in the northern hemisphere occurs at the edge of the permanent cap. In the southern hemisphere the precipitation appears to increase almost linearly with altitude. Source: Smith & Zuber, 2018

The influence of the solar system celestial bodies, and its two moons Phobos and Deimos, causes perturbation of the Martian orbit resulting in variations in Mars Orbital parameters [a precession with a rate of -7576 milli-arcseconds yr^{-1} (Folkner et al.1997).]. These variations are mostly periodical and alter the amount of radiation that reaches the surface at different latitudes, in the case of obliquity and eccentricity variations. Due to the spin-orbit resonance, Mars rotational axis inclination undergoes a short-term variation with a ~120 kyr period (Ward, 1973). Also, the eccentricity varies with periods of about 95 to 99 kyr and 2400 kyr of a value between 0 and 0.12 (Laskar et al., 2001; 2004). The argument of perihelion varies with a period of 51kyr and the orbital inclination varies between 0 and 8° occurring every 1.2 Ma (Fishbaugh et al., 2008). Obliquity varies from 0 to 80° with a most probable value of 41.8° (Laskar et al., 2004) and with a 63% probability of it being >60° in the past billion years (Fishbaugh et al., 2008). The Martian obliquity exerts the greatest influence, oscillating about its present mean value (25°) with a period of $1.2x10^5$ y and with an amplitude of oscillating that varies with a period of $1.3x10^6$ y (Ward, 1992; Laskar & Robutel, 1993; Touma and Wisdom, 1993; Laskar et al., 2004). The main influence on the ice caps bulk, as has been previously

said, is the distribution of solar radiation on the surface which dictates the annual rate of accumulation and sublimation of H_2O and CO_2 ice.

Tab. 2 Physical properties of Mars

Mass	6.4185×10^{23} kg
Volume	1.6318×10^{11} km^3
Mean density	3933 kg m^{-3}
Mean radius	3389.508 km
Mean equatorial radius	3396.200 km
North polar radius	3376.189 km
South polar radius	3382.580 km
Sidereal rotation period	24.622958 h
Solar day	24.659722 h
Flattening	0.00648
Precession rate	-7576 milli-arcseconds yr^{-1}
Surface gravity	3.71 m s^{-2}
Escape velocity	5.03 km s-1
Bond albedo	0.250
Visual geometric albedo	0.150
Blackbody temperature	210.1 K

Source: Data from Smith et al. (2001) and NDSSDC Mars.

Fact Sheet: nssdc.gsfc.nasa.gov/planetary/factsheet/marsfact.html

Another parameter to consider is the percentage of dust in the atmosphere, that absorbs the solar radiation coming directly from the Sun and reflected by the surface. Dust deposition also lower the ice-surface albedo, increasing the amount of radiation absorbed at the surface. The albedo is predominantly controlled by the amount of CO_2 deposited during the fall and winter seasons and carbon dioxide ice clouds may affect infrared emission. The PLD (polar layered deposits, see section 2.2.1.3 & 2.2.2.3) may undergo variations due to impacts of meteorites and volcanic eruptions which melts the ice and alter the amount of dust diluted in the atmosphere. However, volcanic influences

during the Deposits lifetime are extremely rare and so not responsible for the bulk impurities of ice. There are many ways in which the obliquity may affect the climate, but the effects are not easily predictable. For example, the climate warming might lead to an increase in surface pressure, increasing the dust deposit and lowering the albedo, hence leading to cooling. At the same time, a decreasing climate temperature may lead to an increased ice stability and consequently a higher albedo. At very low obliquity 10°-15°, the atmosphere collapses and condenses onto the surface, with distribution controlled by topography (Kreslavsky and Head, 2005). At present-day low obliquity, ground ice is stable only at latitudes above 60°-70° (Mellon and Jakosky, 1995). There is a global distribution of ground ice a few meters above the regolith when the obliquity reaches 32° and the temperature at the equator gets lower (Mellon and Jakosky, 1995).

But at the same time, the climate at the poles gets warmer and the ice is unstable (Mischna et al.,

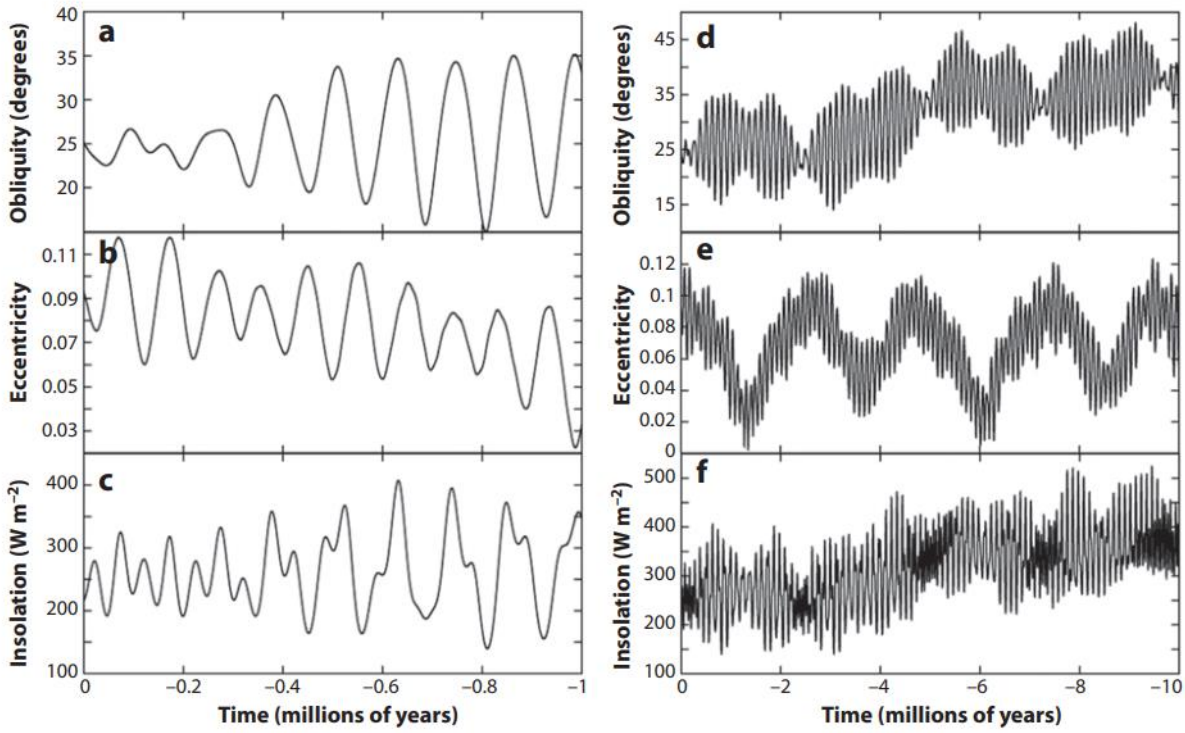

Figure 4 The diagrams represent the quasi-periodic variation of the insolation with respect to Mars orbital eccentricity and axial obliquity astronomic cycles during the last million year (left) and ten million years (right). Credits: Images adapted from Grima (2009) (top-left) and Laskar et al. (2002) © Nature (bottom)

2003). Glacial features at mid-latitudes, such as lobate debris aprons and lineated valley fills, may testify for these assumptions. The Hesperian-aged south circumpolar Dorsa Argentea formation has

been interpreted to be an ancient polar deposit underlying the present SPLD and extending over twice the area of the current PLD (Head & Pratt 2001).

2.2 MARS POLAR ICE CAPS

Before going deep with the data analysis, we will discuss the main properties of the north and south ice caps. The general structure of both polar caps consists of an upper seasonal CO_2 dome (Forget

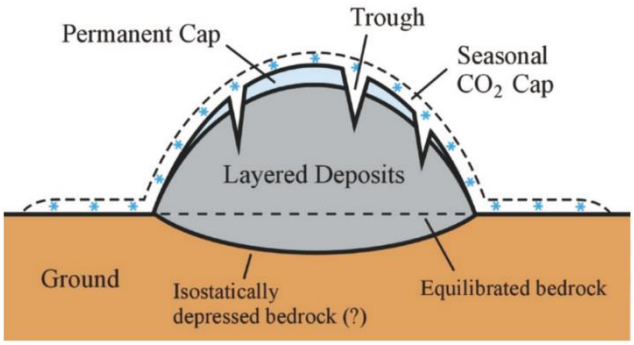

Figure 5 Polar caps structure schematic representation. Vertical scale exaggerated by a factor 150 for the layered deposit, by an unknown factor for the permanent cap and a factor 50000 for the seasonal cap. Source: Greve 2008

1998), a permanent water-ice cap (Kiefferet al.,1976; Kiefferet al.,1979; Paige et. al 1990 polar ice caps), and a Polar Layered Deposits unit (PLD) lying above the Martian bedrock (Fig. 5).

As previously said, to obtain information regarding the thickness and composition of the caps we need to understand the dielectric properties of the materials that are distributed within and underneath the polar caps. The bedrock composition varies depending on the geological history of the planet and the degree of porosity which cause a mixture of rocks and liquid or glacial intrusion by the overlain Polar Layered Deposits. As suggested by the NASA Pathfinder APXS and the chemical classification of lava (Picardi et al., 2005), the dielectric constants, within which the

Martian surface materials may vary, are proper of Basalt and Andesite, two igneous rocks of low and intermediate silica content respectively (Tab. 3).

Tab. 3 Dielectric properties of the subsurface materiel Source: Picardi et al., 2005		
	Basalt	Andesite
ε_r	7.1	3.5
tanδ	0.014	0.005

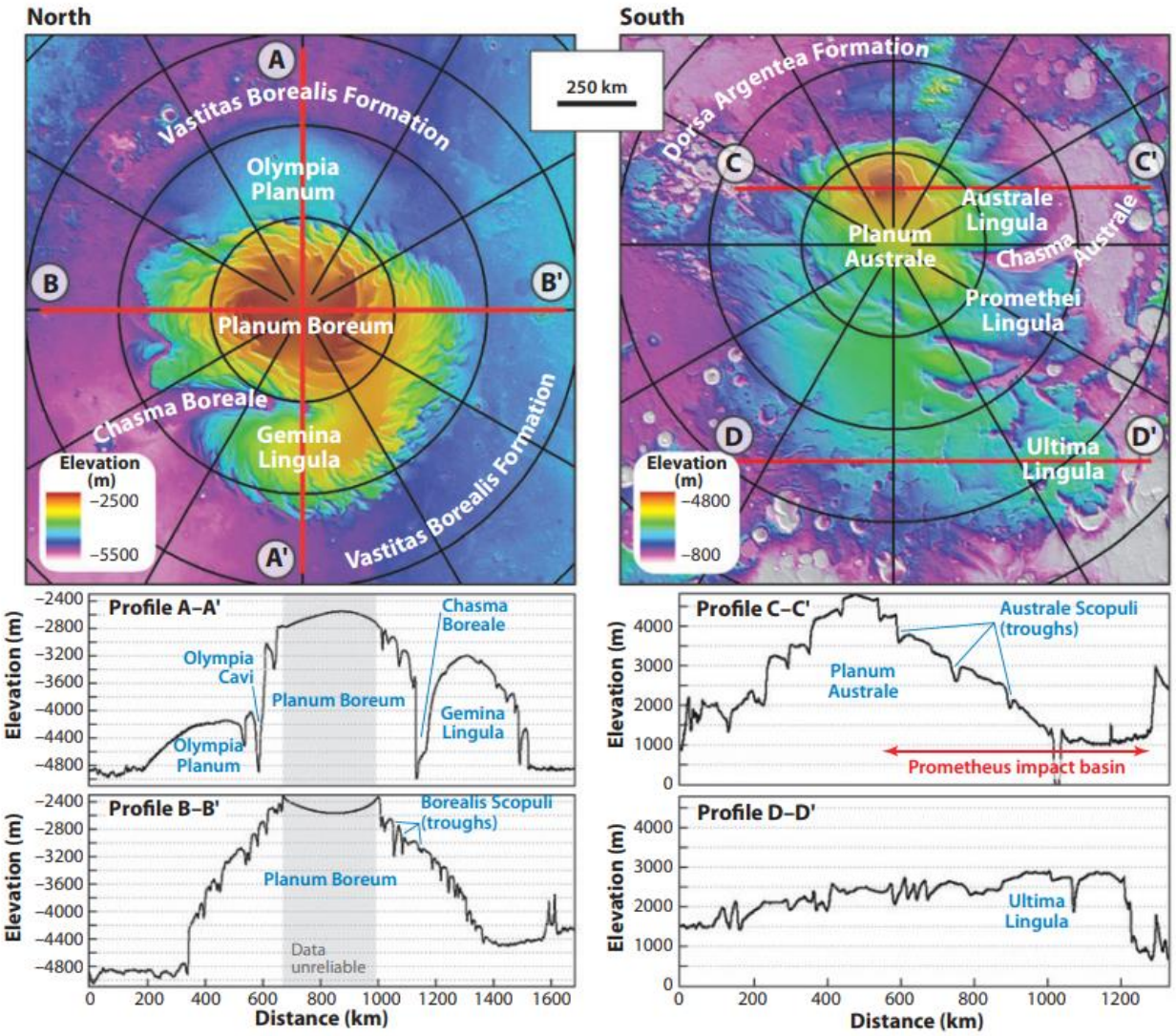

Figure 6 Regional MOLA topographic maps showing the north (left) and south (right) polar regions at the same scale. Red lines indicate locations of topographic profiles. Gray shading in north polar profiles indicates the region for which topographic data are unreliable. Parallels are plotted every 5◦. 0◦E is at the bottom in the north polar view and at the top in the south polar view.

Source: Byrne, 2009

2.2.1 NORTHERN POLAR ICE-CAP: PLANUM BOREUM

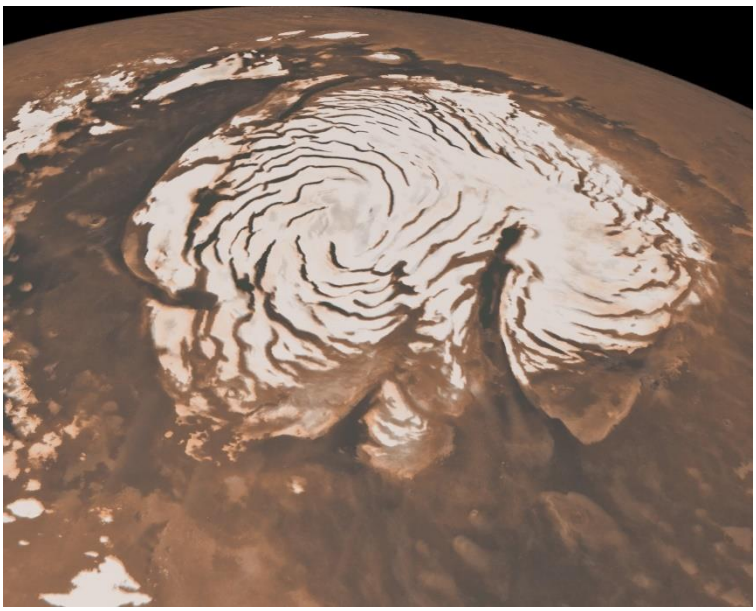

Figure 7 Northern ice cap picture from Mars Orbiter Camera of the MGS orbiter

Source: https://www.nasa.gov/mission_pages/MRO/multimedia/pia13163.html

2.2.1.1 NORTHERN SEASONAL ICE-CAP

Many of the characteristics of the northern Northern Ice Cap (NIC) are in common with those described in the southern one. Structures and composition are almost the same with some distinctions mostly due to the different degrees of insolation caused by the orbit eccentricity around the Sun. The northern pole, in fact, is characterized by warmer winters, resulting in an overall seasonal ice cap thinner than the southern one (it is generally 1.5-2 m thick) that sublimates completely during the summer (Mesick & Feldman 2020). Another difference is that while the southern Seasonal Ice Cap (SIC) rises above the surrounding terrain, the northern one, extending to 60°N symmetrically to the pole, lies near the bottom of the North Polar basin (Zuber et al., 1998; Head et al., 1999).

2.2.1.2 NORTHERN RESIDUAL ICE-CAP

With a volume of 1.1-2.3x10^6 and a diameter of 1100km (Zuber et al., 1998; Smith et al., 2001), the northern Residual Ice Cap (RIC) mostly covers Planum Boreum reaching a height of 3 km (the highest region of the north cap approximates the position of the present rotational pole; Fishbaugh & Head, 2001). On the contrary to the southern pole, the northern RIC does not contain CO_2 layers but

only water ice. Moreover, the albedo of the surface (Bass et al., 2000; James and Cantor, 2001; Kieffer and Titus, 2001; Malin and Edgett, 2001; Hale et al., 2005) suggests the presence of dust impurities in the icy layers and changes of grain size (Warren and Wiscombe, 1980; Kieffer, 1990; Langevin et al., 2005). OMEGA instrument, which provides the mineralogical and molecular composition of the surface of Mars through imagery and infrared spectrometry, indicates a maximum dust content of about 6% (Langevin et al., 2005). The northern RIC surface is characterized by different morphological features, resulting from the ablation of the ice and erosion by strong wind and forming pits, cracks, and knobs. Also, the RIC displays a series of spiral troughs that reach the underneath North PLD (i.e., depths up to 1km) with a clockwise pattern (Zuber et al.,1998).

2.2.1.3 NORTH POLAR LAYERED DEPOSITS (NPLD)

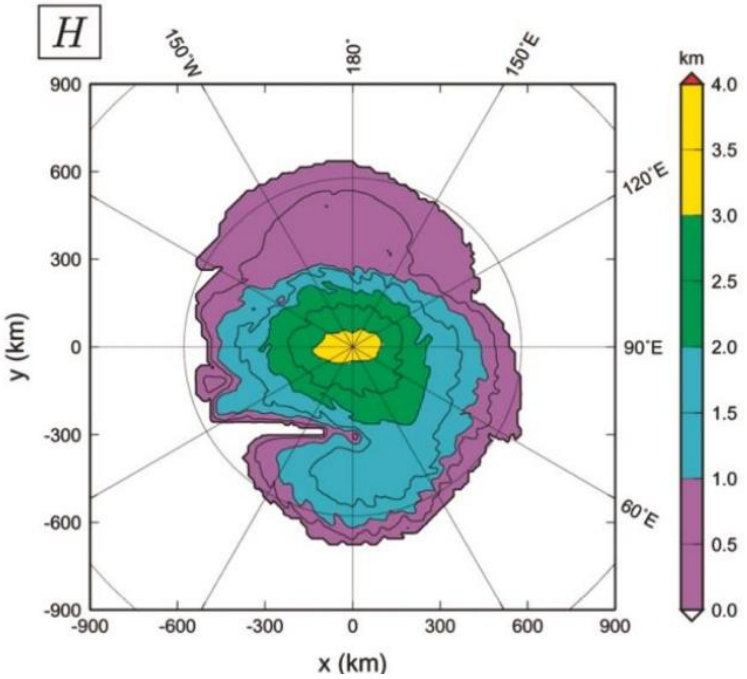

Figure 8 North polar layered deposit computed thickness

Source: Greve, 2008

Similar to the South PLD, the NPLD are composed of different strata of ice up to ten meters of thickness (Brothers et al., 2015) accumulated throughout its depositional history with various ice-dust fractions (e.g., Cutts & Lewis, 1982; Hvidberg et al., 2012). In particular, it is generally

accepted that 95% of the composition of the layers, showing a regional dielectric constant value of 3.15, consists of water ice (Grima et al., 2009; Picardi et al., 2005). The NPLD has a volume of $1.2\pm0.2\times10^6$ km^3 (polar ice caps) and their bulk density is 1,126 ± 38 kg/m^3 (Ojha et al., 2019). The center of the NPLD unit is offset toward a 0°W longitude due to the retreat of the cap predominantly from the 180°W direction. At the same time, the highest elevation of the cap approximates the position of the present rotational pole (Fishbaugh & Head 2001). Like in the southern hemisphere, the NPLD are cut by a reentrant valley (i.e., Chasma Boreale), supposed to be originated by katabatic wind erosion (Kolb e Tanak, 2001) or catastrophic floods (Anguita et al., 2000), and a series of spiral troughs (far more numerous than in the south).

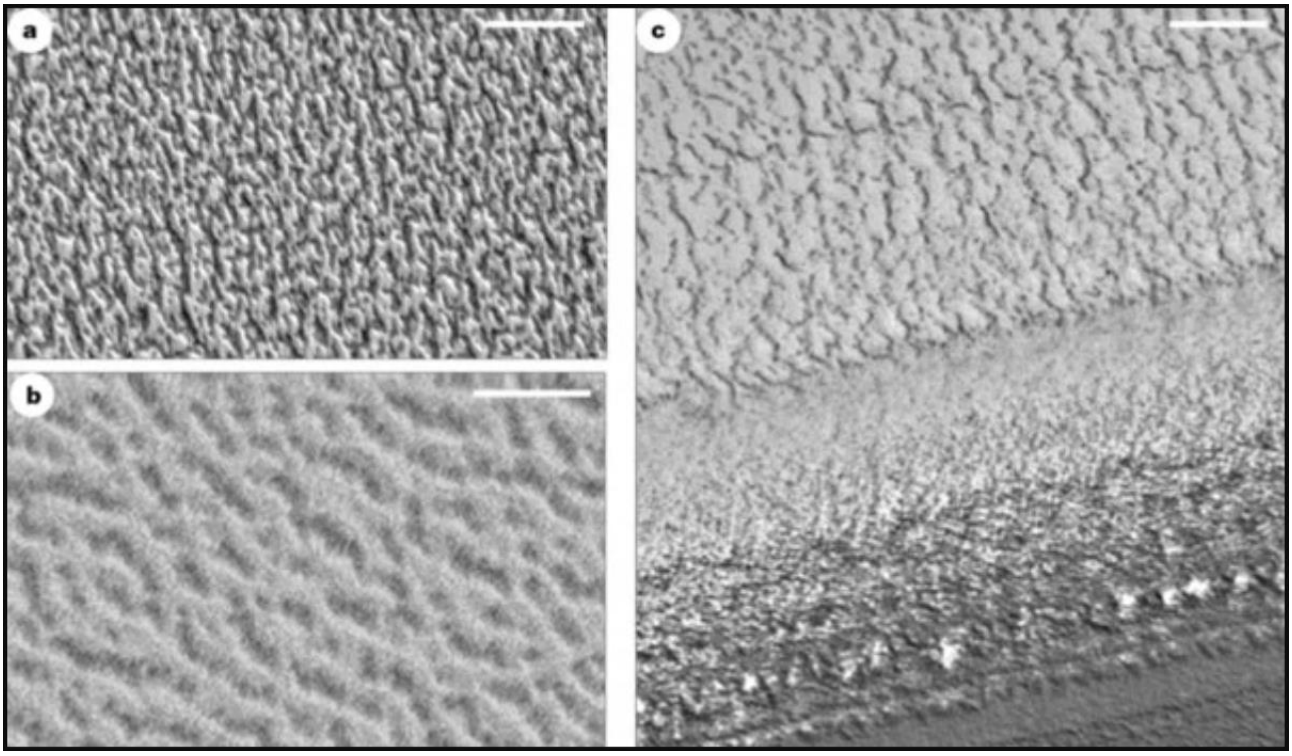

Figure 9 ***a****, Individual and connected pits in surface of residual cap. Portion of Mars Orbiter Camera (MOC) image M00-00547 (mapping phase 0, image 547), 82.1° N, 329.6° W, solar incidence angle* i *= 73°. Texture on most of the north-polar residual cap is a variant of pitting of approximately similar width depressions; length and connectivity of depressions varies. Depths inferred from minimal evidence of shadows are probably less than 2 m. Scale bar is 200 m. Illumination is from upper right. Aerocentric longitude of the sun (*L_s*) is 120° (0° is northern spring equinox). 5 April 1999. This and other images shown have been contrast enhanced.* ***b****, North-polar residual cap surface, portion of image CAL-00433; 86.9° N, 207.5° W; scale bar is 50 m. Illumination is from upper right.* L_s *= 107°. 8 March 1999.* ***c****, merging of pits and fissures of residual cap topography with exposure of layers in walls of one of the dark lanes (troughs with wall slopes generally less than 10°) that traverse much of the northern layered deposits; area at bottom of image is largely frost-free. Portion of MOC image M00-02072; 85.9° N, 258.1° W;* i *= 70°. Scale bar is 100 m. Illumination is from upper right.* L_s *= 124°. 13 April 1999. Source: Thomas et al., 2000*

2.2.2 SOUTHERN POLAR ICE CAP: PLANUM AUSTRALE

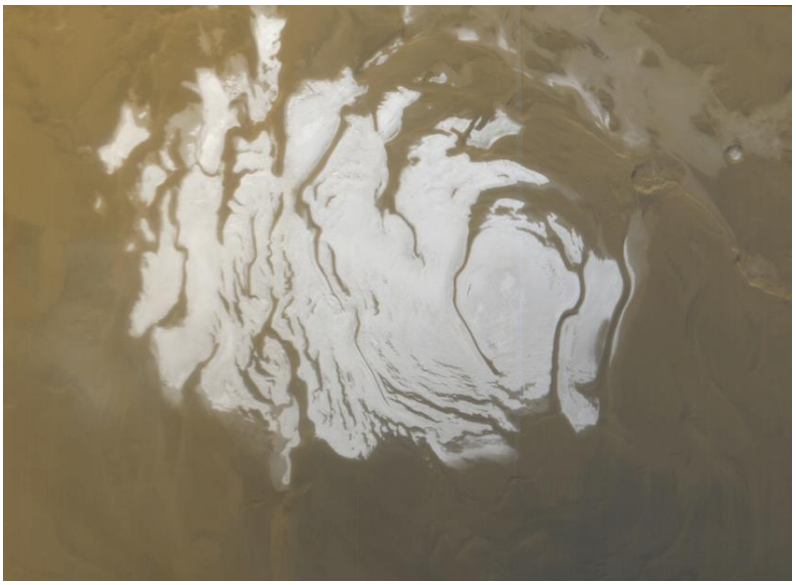

Figure 10 South polar cap picture from Mars Orbiter Camera of the MGS orbiter

Source: https://www.nasa.gov/centers/ames/multimedia/images/2005/marscap.html

2.2.2.1 SOUTHERN SEASONAL ICE-CAP

The Seasonal Ice Cap (SIC) is centered around the geographic pole (Barlow, 2014) and extends to a latitude of 50°S during the winter (Hansen et al., 2010). In the southern hemisphere, the SIC is characterized by thin layering -ten centimeters to meters- of CO_2 ice (showing high reflectivity) that sublimates during the summer and deposits during the winter. This mechanism is part of a seasonal cycle as a result of the planet's axial inclination and during which the carbon dioxide sublimates from one pole to move to the opposite one. This periodic process involves almost 25% of the atmospheric CO_2 (Mesick & Feldman, 2020). The sublimation is helped in the southern hemisphere because it is affected by higher temperatures than in the northern. In fact, at the south pole, the summer season occurs when the planet reaches the perihelion (Greve, 2018).

2.2.2.2 SOUTHERN RESIDUAL ICE-CAP

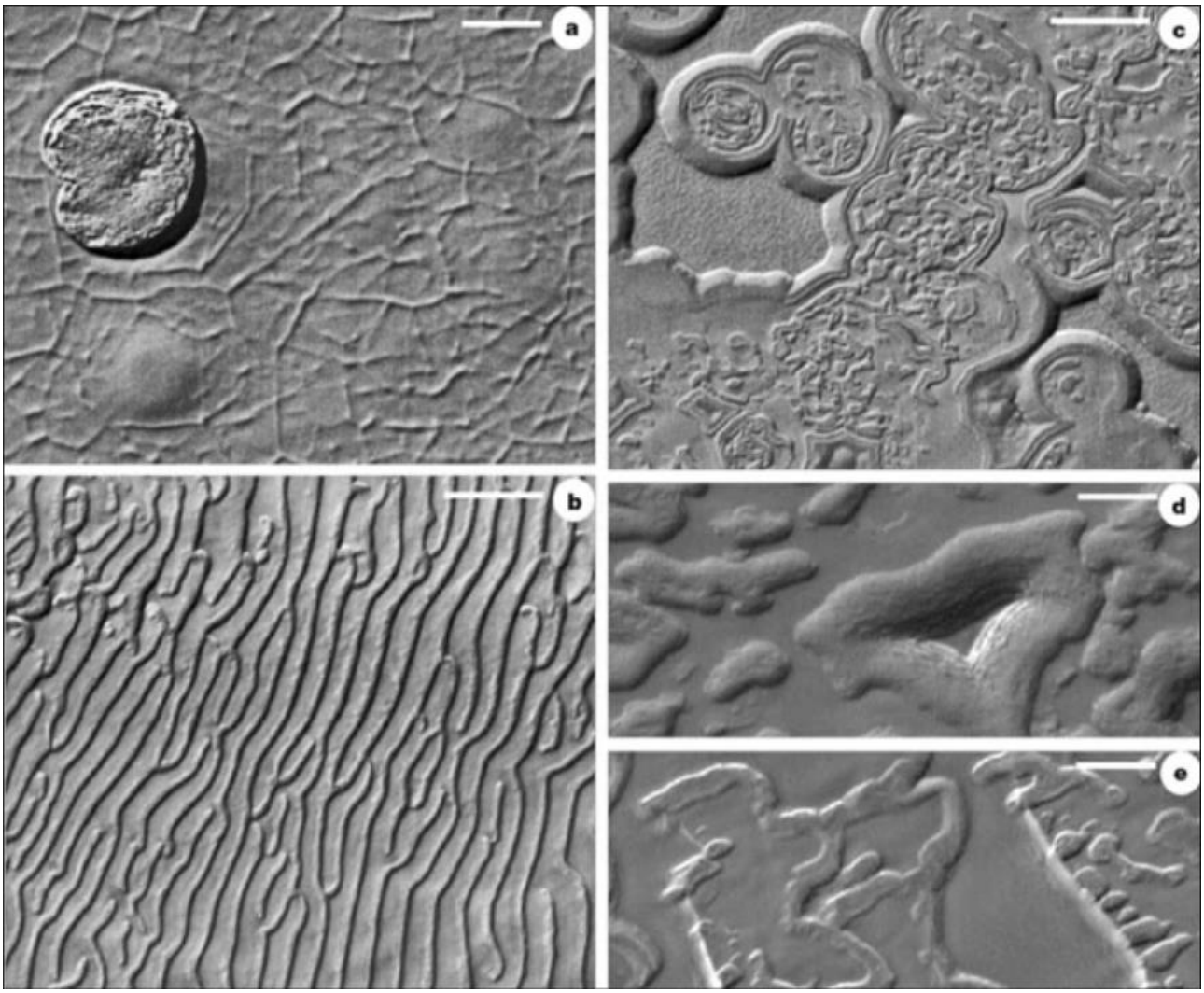

Figure 11 12 ***a****, Nearly circular depression and nearby sag surface on top layer. Polygonal cracks are prominent on undisturbed sections of the upper layer surface, but do not affect the margins of circular depressions. Portion of MOC image M09-00609; 87.0° S, 5.9° W;* i *= 70°. Scale bar is 100 m. Illumination is from lower right.* L_s *= 237°. 3 November 1999.* ***b****, 'Fingerprint' pattern of depressions. Elongated sags in other areas of residual cap suggest precursors of this topography. Steeper sides (right) of the troughs face in a more northerly direction, suggesting sublimation in expanding depressions, as with the more circular ones. Portion of MOC image M03-06756; 86.0° S, 53.9° W;* i *= 88°. Illumination is from lower right. Scale bar is 500 m.* L_s *= 182°. 4 August 1999.* ***c****, Circular collapse features, leaving mesas on upper surface with debris aprons and moats. Largest scarps here are about 4 m high. The uppermost layer is capable of supporting scarp slopes of ~20°; the aprons frequently have slopes of order 1°–3° (Fig. 2b); slopes are estimated from presence or absence of shadows as the sun gained elevation in the southern spring. Portion of MOC image M03-06646; 85.6° S, 74.4° W;* i *= 88°. Scale bar is 500 m. Illumination is from lower right.* L_s *= 181°. 3 August 1999.* ***d****, Residual mesa exposing four layers and surrounding moat. Formation of moats probably requires additional deposition and sublimation or compaction following removal of material from height of top layer exposed here. Portion of MOC image M07-02129; 86.9° S, 78.5° W;* i *= 81°. Scale bar is 100 m. Illumination is from bottom, right.* L_s *= 204°. 11 September 1999.* ***e****, Complex covering of depressions which suggest burial and exhumation of topography on part of the southern residual cap area. Portion of MOC image M04-03877; 84.6° S, 45.1° W,* i *= 81°, scale bar is 200 m. Illumination is from lower right.* L_s *= 196°. 29 August 1999.*

Source: Thomas et al., 2000

The southern Residual Ice-cap (RIC) is characterized by an elevation 6 km higher than the northern one and is offset with respect to the planet rotational axis toward the 180°W longitude (Fishbaugh & Head, 2001). The RIC estimated volume is about 1.2-2.7x10^6 km^3 (Smith et al., 2001) and it has a diameter of about 400 km (Barlow, 2014). Data collected from Viking (Mouginot et al., 2008) and Mars Express orbiter indicate that the RIC is composed of a permanent upper CO2 ice-cap overlapping water-ice layers. The residual cap is characterized by a thickness of 8 meters (Stevens, K. W. 2007) and by a dielectric constant of 2.2 (Mouginot et al., 2009). The sublimation and collapse of carbon dioxide veneer (Byrne & Ingersoll, 2003) produce a variety of morphologies, such as depressions with a wide variety of shapes (Thomas et al., 2000b).

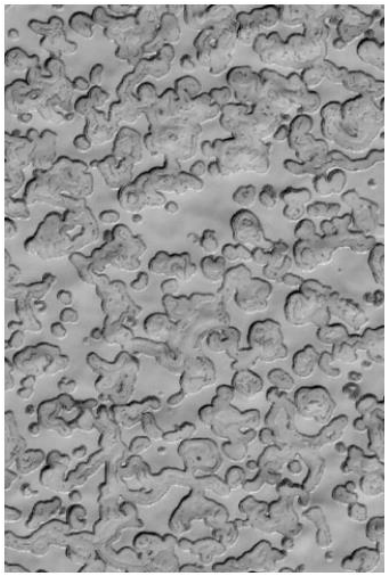

Figure 13 swiss-cheese' terrain caused by the sublimation of CO_2 ice on the southern ice cap. (MOC image MOC2-780, NASA/JPL/MSSS)

2.2.2.3 SOUTH POLAR LAYERED DEPOSITS (SPLD)

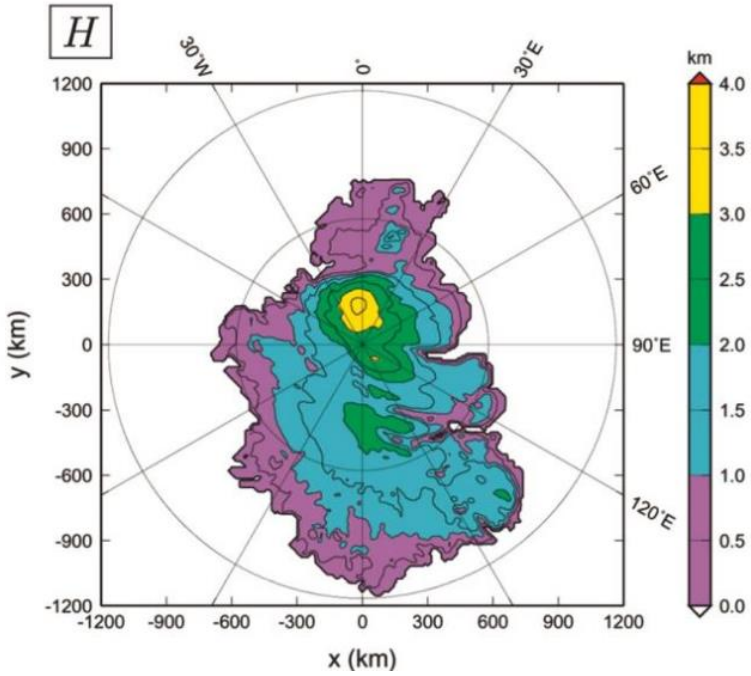

Figure 14 South polar layered deposit computed thickness

Source: Greve, 2008

The South Polar Layer Deposits (SPLD) underlies the RIC and represents the oldest unit of the southern polar-cap. SPLD are characterized by stratified layers of water ice and, in low percentage (5-10%; Heggy, 2006) of dust mixture silicate. Besides, composition models have shown dielectric constant consistent with the local interbedding presence of CO_2 ice (Liu et. al, 2014). Also, the SHARAD instrument has displayed CO_2 deposits below Australe Mensa, having a volume of about 16,500 km^3 (Putzig 2018). The deposits are offset from the pole by ~2° and are asymmetrically distributed between latitudes 70° and 80°S. It has been estimated (Herkenhoff & Plaut, 2000) that the surface age of the South Polar Layered Deposits (about 10 Ma) is two orders of magnitude greater than the surface age of the NPLD (at most 100 ka). The centers of symmetry of the northern and southern planform shapes are asymmetrical about the current rotational pole; therefore, they are offset few degrees from the pole in antipodal directions from each other (Tanaka and Scott 1987, Smith et al., 1999, Fishbaugh and Head 2000a, Ivanov and Muhleman 2000). The ice-dome shows spiral scarps that have a counter-clockwise pattern extending from the pole, dissecting the residual cap, outward into the PLD to 82.5°S; this feature could be caused (both in the southern and northern)

by the preferential sublimation of ice from the sun-facing slopes (Howard et al., 1982), enhanced by strong katabatic winds produced by the sublimation and deflected by the Coriolis force (Howard, 2000). As an alternative, it could be modeled by non-homogenous ice-flows from the accumulation center of the ice-cap toward the ablating edges (Fisher 1993; Fisher 2000). A large reentrant valley, Chasma Australe, cut the deposit for several hundred kilometers with a width of about 20 km (Anguita et al., 2000). The volume of SPLD has been evaluated around $1.6\pm0.2\times10^6$ km^3 (Plaut et al., 2007), while the unit reaches a maximum thickness of 3.7±0.4 km in correspondence of the highest MOLA elevation, close to 0°E (Plaut et al., 2007). Among the large variety of geomorphological structures and findings on Planum Australe, two of them represent the departure point of the object of the present study: 1) A series of scarps with a unique shape. Grima et al. (2010) analyzed and described some morphologies, distributed all over the SPLD, but condensed in Ultimi Lobe. These features appear to be arch-shaped with a cross-section characterized by a trough between a straight slope on one side with outcrops of layered deposits and a convex upward slope on the other one that flattens as it rises. These semicircular structures, defined as Large Asymmetric Polar Scarps (LAPSs) can reach a length in the order of tens of kilometers. Furthermore, some of them are aligned and/or appear connected with a relatively uniform direction (Fig. 15), where the concave sides never face the South Pole, and the dominant orientation is not toward the azimuth. The extremely deep troughs formed by LAPSs in the ice create scarps whose height ranges from 200 to 700 m with an average of 400 m, penetrating the glaciers to part of its thickness. The side of the

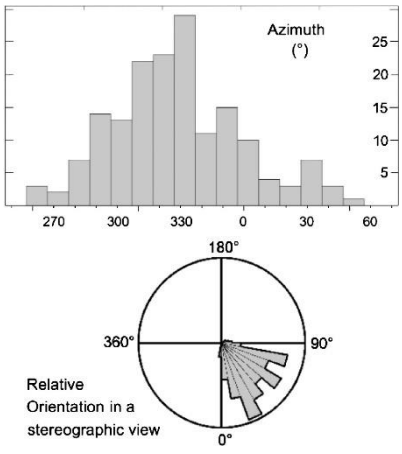

Figure 15 (Top) Histogram of the LAPS azimuths. The Y-axis is the number of occurrences. A concavity facing north has an azimuth equal to 0. A concavity parallel to a longitude and facing decreasing west-longitudes has an azimuth equals 90. (Bottom) Circular histogram of the relative orientation of the LAPSs in a regional context. The circle border represents 25 occurrences. Source: Grima et al., 2011

scarps with a convex slope shows a more complex topography. The ascending wall gently curves

until it flattens out. Along certain scarp crests ridge similar to elongated hillocks may overly these formations.

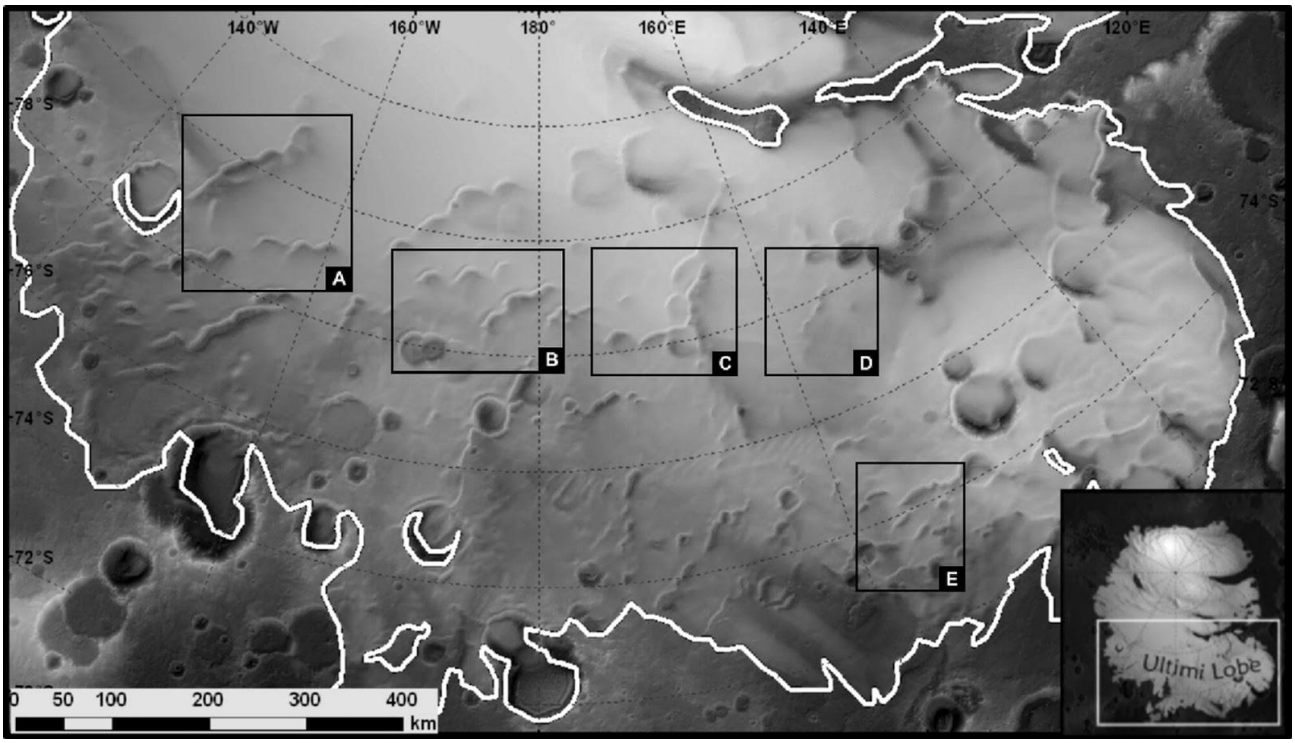

Figure 16 Shaded topography of UL (stereographic projection with illumination from the bottom-right). The white line is the Planum Australe boundary. The bottom-right insert locates UL within the entire polar plateau. Black boxes (A, B, C, D, E) outlining the LAPSs. Source: Grima et al., 2011

2) Recent studies made by Orosei et al. (2018) based on the high value of the medium permittivity have shown the presence of liquid water beneath the SPLD in a 20 km wide zone centered at 193°E, 81°S, then confirmed by further geological and physical studies of a wider zone (Lauro et al., 2021).

3 OBSERVATIONS AND MARS MISSIONS

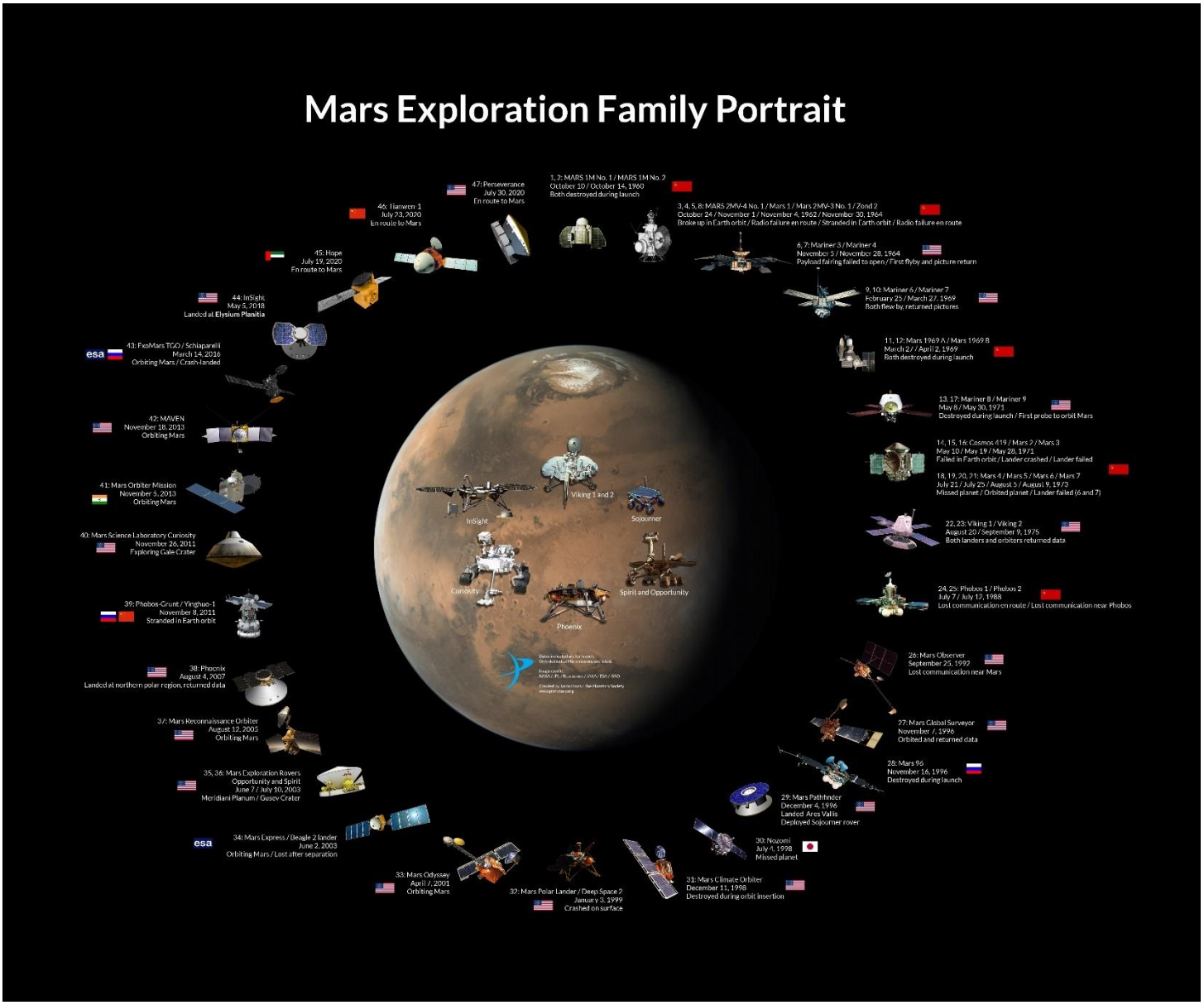

Figure 17 All Spacecraft Missions to Mars since 1960. Planetary society https://www.planetary.org/space-images/the-mars-exploration-family-portrait

First observations with a telescope, were made by Galileo in 1609 followed by many others such as Huygens with the first report of albedo marking, Cassini who noticed for the first time the bright polar caps, and Herschel in 1783 when he determined the inclination of Mars' rotation axis. Mars has been a major spacecraft destination ever since the early days of space exploration mostly cause one of the biggest questions was concerning the possibility to find alien life on other planets besides Earth. Until these days many nations have been involved in the production and expedition of Orbiters

and Landers toward the Martian body (Fig. 17), the more important missions regarding the recent observation of the Polar Caps are Mars Global Surveyor, Mars Odyssey, Mars Express, Mars Reconnaissance Orbiter, and ExoMars.

3.1 MARS MISSIONS

3.1.1 Mars Global Surveyor

The Mars Global Surveyor spacecraft reached mars' orbit in 1997 with an average altitude of about 378 km. The observations made, have provided information regarding the state of the magnetic field (which has ceased to exist -except some remnant magnetization within the rocks- caused by the recent absence of an internal dynamo), the thickness variation of the crust on both hemispheres, the shape of the gravitational potential, general surface and polar caps composition based on the albedo, erosional effects of wind and water fluxes on the ground and atmospheric circulation. The instruments that made possible these evaluations were: Mars Orbiter camera, an imaging system designed to take high spatial resolution images of the surface and lower spatial resolution, synoptic coverage of the surface and atmosphere, Mars Orbiter Laser Altimeter, a laser pulse altimeter able to determine globally the topography of Mars by generating high-resolution topographic profiles, Thermal Emission Spectrometer to study trough the thermal infrared emission of the planet the surface and the atmosphere of Mars and a Magnetometer/Electron Reflectometer suitable for the study of any magnetic fields (Albee et al., 2001).

3.1.2 Mars Odyssey

The Mars Odyssey spacecraft reached the Martian orbit in 2002 with an orbit of 370 to 432 km above the ground and in an inclination of 93.1°. The goal was to map the elemental composition of the surface, determine the abundance of hydrogen in the shallow subsurface, acquire high spatial and spectral resolution images of the surface mineralogy, provide information on the morphology of the surface, and characterize the Martian near-space radiation environment as related to radiation-induced risk to human explorers. The instruments onboard were: Thermal emission Imaging System to determine the mineralogy using multispectral, thermal- infrared images, Gamma Ray Spectrometer for a full planet mapping of elemental, hydrogen, and CO_2 abundances through

gamma-ray and neutron spectroscopy, and the Martian Radiation Environment Experiment to measure the exposure of tissues to radiation (Saunders et al., 2004)

3.1.3 Mars Express

The ESA Mars Express mission was launched in June 2003 from the Baikonur Cosmodrome in Kazakhstan over a Soyuz rocket and reached Martian orbit in December of the same year. The mission carried an orbiter and a lander, Beagle 2, which never sent any signal back from the surface of the planet, to study together with the inventory of water or ice in the Martian crust and to gather evidence about any form of life, if ever there was one. Beagle 2 was supposed to land on Isidis Planitia, an impact basin characterized by layered deposits of sedimentary rocks probably generated by the water and surrounded by a variety of igneous rocks and craters of different ages, to study the geology of the ground together with the mineralogical and chemical composition. The spacecraft carrying the lander separated from the orbiter during the collision course, crossing the atmosphere in 5 minutes, five days after the split. The actual condition of Beagle2 is still unknown. The orbiter was placed in an elliptical near-polar orbit of 86.5° inclination and a period of about 7.5h with an apocenter of 11500 km and a pericenter of 250km(sci.esa.int). The spacecraft consists of various instruments for the breakdown of the surface and subsurface properties and the analysis of the atmosphere. There are 6 instruments, in addition to a radio-science experiment, which deals with the solid (HRSC; OMEGA; MARSIS) and those analyzing the atmosphere (PFS; SPICAM; ASPERA). The MaRS radio science experiment provides insights into the internal gravity anomalies, the surface hardness, the neutral atmosphere, and the ionosphere of Mars. The PFS is an IR spectrometer for atmospheric studies. The main goal is to observe the variations of the global temperature in the long-term along with the chemical composition of the aerosol. SPICAM is a UV and IR spectrometer which studies photochemistry and the density-temperature structure of the atmosphere (0 - 150km), the upper atmosphere-ionosphere escape process, and the effect of the solar wind. The ASPERA experiment focuses on the upper part of the atmosphere affected by the solar wind; moreover, it analyzes the interaction with the near-Mars plasma and neutral gas environment. HRSC instrument consists of a very high-resolution camera that captures all the geomorphological features to comprehend the influence of the water and weathering on the surface. The near-IR spectrometer OMEGA uses the signals in the infrared spectrum to differentiate the mineralogy of the surface and analyze the distribution of CO_2, CO, H_2O, dust, aerosol in the atmosphere. Mars Advanced Radar

for Subsurface and Ionosphere Sounding (MARSIS) is a low-frequency nadir-looking radar sounder and altimeter with ground-penetration capabilities operated. It uses synthetic aperture techniques (Chicarro et al., 2004).

3.1.4 Mars Reconnaissance

The Mars Reconnaissance Orbiter spacecraft entered Mars' orbit in 2006 with a low near-polar orbit of 255 to 320 km. The main objective was to gain information concerning the geology, geophysics, climate, and volatile characteristics of the planet, find a clue about the possible presence of life forms and assess the nature and inventory of resources on Mars in preparation for human exploration. The observations were conducted with the help of different instruments such as the Mars Color Imager consisting of two framing cameras for the investigation of the weather conditions and the ozone for the evaluation of water vapor content in the atmosphere. The Mars Climate Sounder, a remote sensing device that works in the spectrum of the thermal infrared, provides a vertical profile for water vapor, dust, and temperature. Compact Reconnaissance Imaging Spectrometer for Mars uses detectors that see in visible, infrared, and near-infrared wavelengths to search for the residue of minerals that form in the presence of water, perhaps in association with ancient hot springs, thermal vents, lakes, or ponds that may have existed on the surface. The High-Resolution Imaging Science Experiment and the Context Imager can take pictures from orbit respectively at high and moderate resolution. The Shallow Radar works this the same principle of the MARSIS instrument with the focus on Martian regolith (Zurek et al., 2007). The data collected from the Mars Advanced Radar for Subsurface and Ionosphere Sounding of the ESA's mission Mars Express and the Mars Orbiter Laser Altimeter on the Mars Global Surveyor spacecraft have been used in this work.

3.1.5 ExoMars

The ExoMars program, which has seen an enormous contribution from Italy, is split into two parts. The first one concerns the launch, which happened in 2016, of an orbiter -the Trace Gas Orbiter (TGO)- around Mars and a lander -Schiaparelli- which never reached the surface. The second part consists of a rover and a surface platform which will be sent to the Red Planet in 2022. TGO is concerned with the detection of trace gases, gases that are present in small concentrations in the atmosphere, and their spatial and temporal evolution. What we are trying to do with this probe is to

define in a detailed way the atmosphere of Mars, observe the characteristics of the Martian soil to identify the sources of these gases, and map the subsurface hydrogen.

The tools it carries are: Nadir and Occultation for MArs Discovery (NOMAD) which features three spectrometers for identifying atmospheric components. Atmospheric Chemistry Suite (ACS) three infrared instruments that will support NOMAD. Color and Stereo Surface Imaging System (CaSSIS), a high-resolution camera to determine the geologic context of gas sources. Fine Resolution Epithermal Neutron Detector (FREND), which can detect hydrogen up to one meter deep and detect water ice in the subsurface.

The Schiaparelli lander consists of a platform (DREAMS) for sensing wind speed and direction, humidity, pressure, near-surface atmospheric temperature, atmospheric transparency (Solar Irradiance Sensor, SIS), and atmospheric electrification (Atmospheric Radiation and Electricity Sensor; MicroARES). The COMARS+ instrument would be responsible for detecting temperature and heat flux during the descent phase. The descent camera (DECA) on Schiaparelli had the task of imaging the landing site as it approaches the surface, as well as providing a measure of the atmosphere's transparency. INRI consists of a series of retroreflectors that turn towards the zenith, useful for localization of the module by other spacecrafts. The Exomars rover will perform electromagnetic and neutronic surveys of the subsurface to understand the geological context of the landing site. The ultimate goal would be to identify traces of life forms, present or past. The rover will bring with it different instruments to solve these questions.

- The Panoramic Camera (PanCam) for the digital mapping of the terrain.
- Infrared Spectrometer for ExoMars (ISEM) for mineralogical analysis of the soil.
- Close - UP Imager (CLUPI) for capturing high-resolution images of Martian rocks, outcrops, and cores.
- Water Ice and Subsurface Deposit Observation on Mars (WISDOM) and Adron for characterization of subsurface stratigraphy and detection of subsurface water.
- Mars Multispectral Imager for Subsurface Studies (Ma_MISS) will contribute to the mineralogical and petrographic identification of recovered samples.
- MicrOmega infrared spectrometer for mineralogical study.
- Raman Spectrometer (RLS) that will perform a task similar to MicrOmega with the addition of the identification of organic traces.

- Mars Organic Molecule Analyzer (MOMA) that will search for biomarkers.

The platform will remain stationary and study the surface at the landing site. It will capture images of the landing ground, monitor the atmosphere and climate, study the distribution of water in the subsurface, measure the exchange of volatiles between the surface and atmosphere, perform geophysical surveys, and monitor the radiation environment (sources: https://www.cosmos.esa.int/web/exomars/instruments; https://www.asi.it/esplorazione/sistema-solare/exomars).

3.2 INSTRUMENTS AND TECHNIQUES

3.2.1 MARSIS

The radar can work at altitudes lower than 900 km at frequencies that ranges from 1.3 to 5.5 MHz for subsurface sounding, with a bandwidth of 1Mhz, and 0.1 to 5.5 MHz for ionospheric sounding. These features allow us to map the distribution of liquid or solid water in the upper part of the crust and to put constraints on the electron content during a sol (Martian solar day) of the ionosphere which influences the measurements. The subsurface sounder has two channels comprised in the Radio Frequency Subsystem: the first is connected to a dipole antenna and contains both a receiver and a transmitter meanwhile the second has only a monopole antenna that can receive the signals off-nadir. The antenna subsystem hence consists of a monopole and a dipole antenna respectively 7 and 40, restricted to 20 for dynamical purposes, meters long. The MARSIS antenna, and consequently the very large footprint (~3 to 5 km), does not provide high spatial resolution, severely limiting the ability to define those micro- and meso-scale structures otherwise observable with higher resolution Radars, such as SHARAD (Orosei et al., 2018). The Transmitter controls the signal flow between the antenna and the receive electronics. The Digital Electronics Subsystem (DES) resides in the same box as the radio frequency electronics receiver, it selects the frequencies to be used during the sounding and includes a reference oscillator, timing, and control unit, and the processing unit (Jordan et al., 2009).

3.2.2 MOLA

The main objective of the Mars Orbital Laser Altimeter is to obtain a topographic map of the whole planet thanks to his spacecraft quasi-polar orbit. This instrument uses a technique similar to the RADAR inspections for altimetry, called LIDAR, and has provided a high-resolution measurement of the topography of Mars. Specifically, MOLA uses infrared pulses at a rate of 10Hz and has a spatial resolution of ~1° with an absolute accuracy of 13 m with respect to Mars' center of mass (https://tharsis.gsfc.nasa.gov/MOLA/mola.php, Smith et al., 1999). The laser beam has a footprint on the surface of ~160 m and shot-to-shot spacing of ~330m. The Orbiter sends pulses to the ground and receives the returned signal reflected from the Planet's surface. The altitude (observable) is calculated from the travel time and the known speed of light through a simple formula:

$$a = c\frac{\Delta t}{2} \tag{4}$$

With the altitude, the speed of light, and the travel time. The satellite height over the reference geoid is subtracted from the values measured from the instrument, representing the elevations in terms of topography and eliminating the contribution due to rotation. The gravitational field model used for the geoid is the MGM890i, derived from MGS orbit calibration and tracking and older mission data (Smith et al., 1999). If additional corrections are at first neglected, we find the basic simplified altimeter equation:

$$h = N + H + a \tag{5}$$

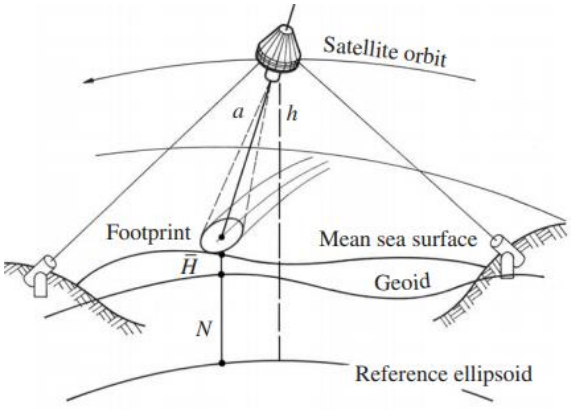

Figure 18 Basic concept of satellite altimetry. Source: Seeber, Satellite Geodesy

With the computed height above the ellipsoid, the surface topography above the geoid, and the distance between geoid and ellipsoid. (Fig. 18). The accuracy of the measurement includes contributions from radial orbit error. Instrument error, and geoid error.

3.2.3 REMOTE SENSING AND SAR

A remote sensing image is characterized by pixels with a horizontal and a vertical resolution. Giving a beamwidth of $\Delta\theta$ (radians), with the antenna pointing perpendicularly to the ground, the azimuth resolution is simply:

$$\Delta x = h\,\Delta\theta \tag{6}$$

Where:

$$\Delta\theta = \frac{\lambda}{L} \tag{7}$$

λ is the signal wavelength and L is the aperture of the antenna. For what concerns the vertical resolution, considering a dipole antenna without an angular aperture of the beam in the range direction, we have to consider the rise time, that is the time that takes for the detected signal to go from zero to the maximum power.

$$\Delta z = \frac{c\,t_r}{2\,S} \tag{8}$$

With S the signal-to-noise ratio

Another important thing is the frequency at which the pulses are emitted. If the frequency is high enough and the platform speed is low, the footprints (area on the surface illuminated by the beam) will overlap. Since each one of these samples is independent, and there are ($\frac{f\,h\,\Delta\theta}{v}$) of them, the vertical resolution when these samples are averaged becomes:

$$\Delta z = \frac{c\, t_r}{2S}\sqrt{\frac{v}{f\, h\, \Delta\theta}} \tag{9}$$

This operation can improve the resolution, but if the Pulse Repetition Frequency (PRF) is too high, it would be difficult for the system to distinguish each pulse. So, the PRF must be lower than $\frac{c}{2h}$ to avoid the signals flying simultaneously. We will try to better understand the concept of 'rise time'. Assuming an ideal flat plane without scatterers, the received power will simply be proportional to the area illuminated by the beam. The transmitting pulse duration is t_p and can be visualized as a 'scattering zone' of thickness $\frac{c\, t_p}{2}$ propagating away from the antenna. The first signal will be received at $\frac{2h}{C}$. At a time Δt greater than this one but smaller than t_p, the wave intersects the surface in a disk of radius r, see figure19. This disk expands over time until $t = \frac{2h}{c} + t_p$ when the trailing edge of the scattering zone just touches the surface. At $t = \frac{2h}{c} + \Delta t$, where Δt is greater than t_p, the scattering zone intersects the surface in an annulus with inner radius r_1 and outer radius r_2, as shown at the right of figure 19. In the first case

$$r \approx \sqrt{c\, h\, \Delta t} \tag{10}$$

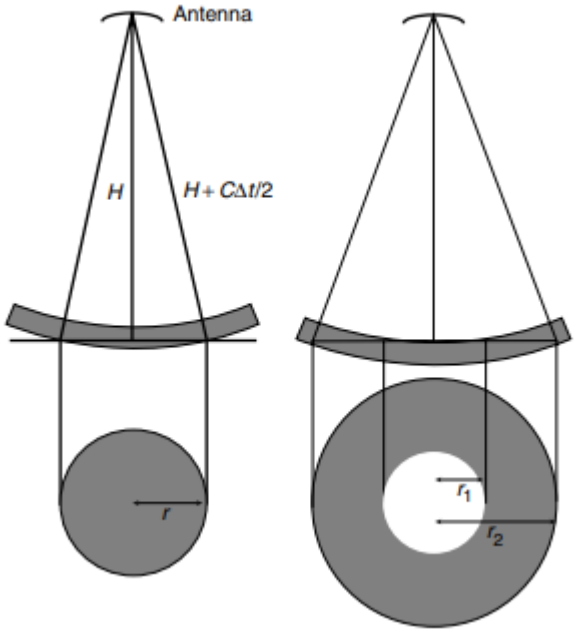

Figure 19 Simplified geometry of a radar altimeter pulse. (Adapted from Rees 2001.). Source: Rees, Remote sensing of snow and ice

In the second case

$$r_1 \approx \sqrt{ch(\Delta t - t_p)} \tag{11}$$

And

$$r_2 \approx \sqrt{c\, h\, \Delta t} \tag{12}$$

The energy received rises from zero, at $\frac{2h}{c}$, to a maximum and then remains constant.

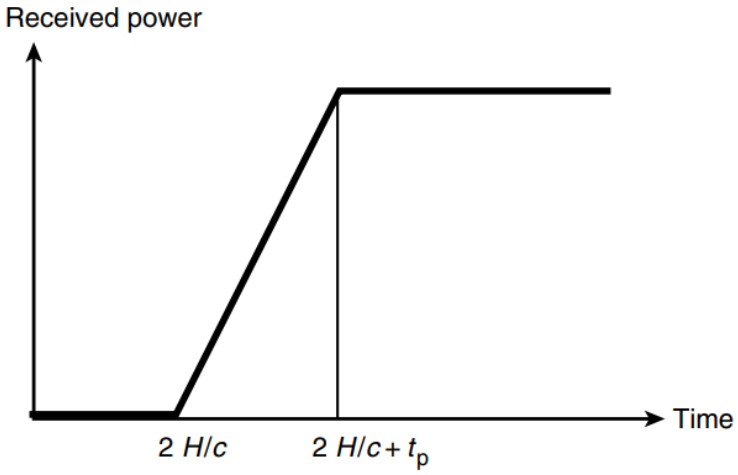

Figure 20 Waveform from a flat surface, using the simple model developed in the text. Source: Rees, Remote sensing of snow and ice

This range of time is the observable that we use in our measurements and it's called rising time t_p, which also resembles the duration of the emitted pulse. The effective horizontal resolution of the altimeter is thus determined by the maximum size of the illuminated disk, just before it becomes an annulus (2 times r).

$$\Delta x = 2\sqrt{c\, h\, t_p} \tag{13}$$

This can be corrected for the fact that the Earth is not flat by replacing h with an effective height h', where $\frac{1}{h'} = \frac{1}{h} + \frac{1}{R}$ and R is the Earth's radius of curvature. The vertical resolution for a single pulse, as has already been told, is:

$$\Delta z = \frac{c\ t_p}{2} \tag{14}$$

The shape of the registered returning wave can give information about the geometry of the scattering surface. For a surface with roughness on a scale shorter than the horizontal resolution Δx, the signal will be broadened by an amount proportional to the roughness, therefore changing the ramp structure already mentioned (Fig. 20) and increasing the time t'_p in this way:

$$t'_p = t_p^2 + \frac{\sigma_h^2}{c^2} \tag{15}$$

σ_h^2 the variance of the surface height. The waveform can indicate if the scattering does not all take place from the surface but contains a significant proportion of volume scattering. This can occur over terrestrial ice masses; if the surface snow is very dry, the microwave radiation from the altimeter can penetrate it to a significant extent. Other delays are caused by the atmosphere. Expressing the lag in the flight time as P, this value varies based on the water vapor content but not on the frequency. For a dry atmosphere, P is 2.33 m per air mass whilst it is 7.1 m per meter of precipitable water. The ionosphere also intervenes in this problem. This delay depends on the frequency *f* of the transmitted pulse and the ionosphere total electron content N_t.

$$\left(\frac{P}{m}\right) = 4.0\left(\frac{N_t}{10^{17}m^{-2}}\right)\left(\frac{f}{GHz}\right)^{-2} \tag{16}$$

We can apply a simple formula to eliminate the ionosphere effect if the Radar works on two broadly different frequencies.

$$s = \frac{(s_1 f_1^2 - s_2 f_2^2)}{f_1^2 - f_2^2} \tag{17}$$

Being '*s',* the distance measured.

One big problem of orbital Radar is the low resolution of the electromagnetic wave $\Delta\theta$. To obtain good quality images is necessary an antenna of several meters, if not kilometers, wide which is not feasible. We can overcome this problem combining the collected signals along the track creating a synthetic aperture during the data processing. By doing so, we can have the advantages of long-wavelength signals such as gathering data despite the weather conditions and penetrate soil and ice for surface and subsurface analysis without worrying about the image quality. So, each pulse defines a pixel, in which dimensions are determined by the resolution in range and azimuth, with a brightness dependent on the back-scattered radiation from a surface element on the ground (Remote sensing of ice and snow; Rees, 2005). If the Radar has an angular aperture in elevation other than in azimuth and the incident angle of the beam is not perpendicular to the ground, the pixels dimensions can be defined by

$$\Delta z = \frac{h\theta_{el}}{\cos\theta_i} \tag{18}$$

$$\Delta x = \frac{h\theta_{az}}{\cos\theta_i} \tag{19}$$

$$\Delta z = \frac{ct_p}{2\sin(\Delta\theta)} \textit{(for a single dipole antenna)} \tag{20}$$

$\theta_i = incident\ angle\ of\ the\ beam$

$h = range\ satellite - surface$

$\theta_{el}, \theta_{az} = respectively\ the\ angular\ aperture\ of\ the\ beam\ in\ range\ and\ azimuth$

$\Delta z, \Delta x = respectively\ the\ dimension\ of\ the\ pixel's\ axes$

$perpendicular\ and\ parallel\ to\ the\ direction\ of\ the\ track$

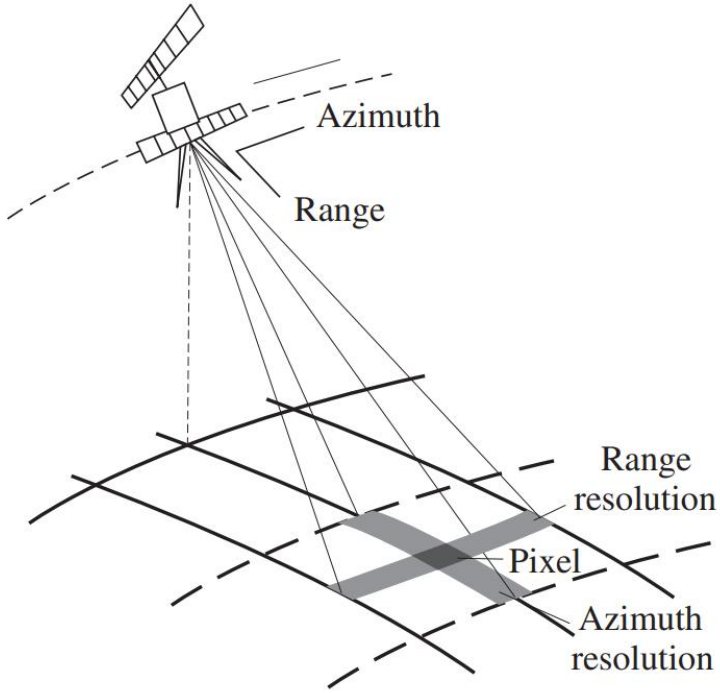

Figure 21 Visualization of a pixel defined by the resolution and the range of the satellite from the planet (Satellite Geodesy, Seeber)

In conclusion, Remote Sensing satellites observable is the interval time that passes since when an electromagnetic signal is sent by the antenna, gets backscattered by a surface, and is collected by the receiver. Another important observable is the strength of the returned signal that gives information - knowing the wavelength, the surface humidity, and the impulse incident angle- about the dielectric properties of the surface materials (Satellite Geodesy, Seeber 2003), but we will discuss this issue in the next chapter.

3.2.4 RADAR ECHO SOUNDING

Radar Echo Sounding is a technique based on the emission and detection of electromagnetic waves that range from 1 to 1000 MHz in frequency.

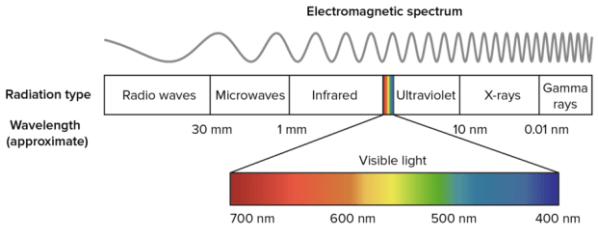

Figure 22 electromagnetic spectrum

This method can investigate the internal and basal proprieties of ice masses, determine the differences between dry and wet regolith based on the presence of water whether it is liquid or solid. As has already been said, the time observable gives the spacecraft height above ground $t = \frac{2h}{c}$ where c is the velocity of the light in the vacuum (The real velocity needs correction based on the atmosphere pressure, water vapor content, and ionosphere influence). However, part of the power transmitted gets lost during the journey for many reasons. Obviously, one of these causes is the geometric spreading of an electromagnetic wave. This problem is stated in the monostatic Radar equation (for Radar that uses the same antenna for transmission and reception) in which we have to take into account, at first, the power P_t emitted, the area illuminated A_t, and its distance r from the platform. So, the power intercepted on the ground is:

$$P_\sigma = \frac{GP_tA_t}{4\pi r^2} \tag{21}$$

Where 'G 'is the gain of the antenna. The reflected signal that gets back to the spacecraft intercepts the areal aperture of the antenna A_e with a power P_r.

$$P_r = \frac{P_\sigma A_e}{4\pi r^2} \tag{22}$$

Substituting P_σ

$$P_r = \frac{GP_tA_tAe}{(4\pi r^2)^2} \tag{23}$$

Which, giving $G = \frac{4\pi A_e}{\lambda^2}$ and considering the fundamental quantity measured by an imaging Radar σ_0 (*backscattering coefficient*) becomes

$$P_r = \frac{\lambda^2 G^2 P_t}{(4\pi)^3 \eta r^4} \sigma_0 A_e \quad (24)$$

η is the efficiency. Is best to specify the backscattering coefficient value logarithmically, in decibels:

$$\sigma_0(dB) = 10\, log_{10}(\sigma_0) \quad (25)$$

The variable received from an imaging radar system is normally not σ_0 but the related value β_0, defined in words as the mean radar brightness per unit pixel area and quantitatively through:

$$\sigma_0 = \beta_0\, sin\, \varphi \quad (26)$$

Where φ is the incident angle. This equation is referred to as the measurement applied to an immediate surface to identify its topographic properties. The backscattering coefficient specifies the scattered intensity logarithmically and the uncertainty of the determination of σ_0 tells the radiometric resolution of an imaging radar or scatterometer.

Remote sensing involves making inferences about the nature of the planet's surface from the characteristics of the electromagnetic radiation received at the sensor. This process requires that we establish the relationship between the physical properties of the materials and the radiation. For the sake of this work, we will discuss mostly ice and snow. Snow is, in general, a mixture of ice crystals, liquid water, and air; its principal characteristic is density. This parameter varies as time passes, as a result of wind and gravity. An empirical model is given by the equation (Martinec 1977):

$$\rho(t) = \rho_0(1 + t)^{0.3} \quad (27)$$

Where t is the elapsed time in days and ρ_0= 0.1 Mg m^{-3}. For different reasons, the grain size is the most important parameter of the snow. The gap between the crystals can contain water, air, solid ice, and other materials. The snow wetness w is defined as the proportion of the snowpack that is in the form of liquid water expressed in volume. For a pack of snow with a total density of ρ_s, giving the

density of water ρ_w, the total mass of ice is defined **as** ρ_s - $w\,\rho_w$ ($w\,\rho_w$ is the mass of water in the pack in proportion to the total mass). If the mean volume occupied by an ice crystal is V, the *mean number density n* of the ice crystals in the snowpack is therefore given by:

$$n = \frac{\rho_s - w\rho_w}{\rho_i V} \tag{28}$$

Where ρ_i is the density of ice. Assuming the ice crystals shaped as spheres of radius **r,** $V = \frac{4}{3}\pi r^3$**.** The porosity is defined as the fraction of volume that is occupied by air. For wet snow, it follows that:

$$p = 1 - \frac{\rho_s - w(\rho_w - \rho_i)}{\rho_i} \tag{29}$$

The high albedo of the snow causes it to reflect almost every electromagnetic wave within the frequency range of the visible light. This is due to the dielectric properties of the ice composing the snow and the high porosity of the pack. Pure ice normally appears nearly invisible to determined frequencies, which means it has a low absorption length. This characteristic is defined as the distance which radiation has to travel inside a medium in order that its intensity is reduced by a factor of e. In fact, the probability of finding a particle at depth *x* into the material is calculated by:

$$P(x) = e^{-\frac{x}{\Lambda}} \tag{30}$$

Λ is material and energy dependent. For example, the absorption length in ice is 10 m. It means that in a 2 m slab of snow with a meter of ice, the possibility that a photon (visible light range) gets absorbed is very low. On the other hand, the photon will encounter of a few thousand of air-ice and ice-air interfaces. Thus, is almost certain that the photon will be scattered back. Moreover, the reflection coefficient of a snowpack should be inversely proportional to the grain size since the number of air-ice interfaces decreases as the crystals dimension increases. Furthermore, as shown by Choudhury and Chang 1979, the increasing absorption at longer wavelengths implies a reduction in reflectance at these wavelengths. After all these statements, an increase in density causes a decrease in the number of interfaces hence, a reduction of the reflectance. Likewise, the absorption

phenomenon, this effect is called *scattering length*, namely the distance that radiation has to travel inside a medium until its intensity in the direction of propagation is reduced by a factor of e as a result of scattering. So, the opacity of a snowpack varies proportionally to its actual thickness and it's defined as *optical thickness*, the ratio between stratum thickness and scattering length of the material. Following this reasoning:

$$\text{scattering length} \propto \frac{1}{n \cdot A_{grains}} \rightarrow \propto \frac{r_{grains}}{\rho_s}$$

Remember n being the mean number density of grains. It is also proportional to the wetness. A significant fraction of the energy transmitted propagates inside the ice medium with a decreased velocity inversely proportional to the refractive index. Being this index, just like the attenuation of the signal, dependent on the dielectric constant of the ice (ε), we can obtain some valuable information about the composition and topography of the mass analyzed. Another property to consider, other than the electrical permittivity, is the electrical conductivity (EC in mS m^{-1}). EC describes the ability of a material to conduct an applied electrical current and is dependent on the temperature and pressure (Glen and Paren, 1975, Fujita, 1993 Plewes 2001) but is principally controlled by the impurity content. The dielectric constant is composed of two parts, the real one ε_r - which alters the velocity of the radiation traveling through a medium, also known as refractive index- and the imaginary part ε_i - which determines the absorption degree of the material-. This complex number can be expressed as

$$\varepsilon = \varepsilon_r - i\varepsilon_i = \varepsilon_r - \frac{i\sigma}{\varepsilon_0 \omega} \tag{31}$$

Where σ is EC, $\omega = 2\pi f$ is the angular frequency of the transmitted wave, and ε_0 the permittivity of vacuum. The loss tangent tanδ (= $\varepsilon_i/\varepsilon_r$), is derived from the loss factor often expressed relative to the real part ($p = \sigma\omega\varepsilon_r$). For the determination of the altered velocity v, we can neglect ε_i and just consider the real part of the permittivity.

$$v = \frac{c}{\sqrt{\varepsilon_r}} \tag{32}$$

We can notice that this is the refractive index and it also depends on the density of the body ($\varepsilon_r = 1 + k\rho_s$ where k is a coefficient depending on the material). The imaginary part depends on the type and number of impurities, on temperature (Dowdeswell and Evans 2004), is proportional to conductivity, related to acidity, and depend on the frequency. The difference in the dielectrics constant between two adjacent media provokes reflection and, the higher this difference, the higher the reflection index. The difference in the dielectrics constant between two adjacent media provokes reflection and, the higher this difference, the higher the reflection index. As already mentioned, the power of the backscattered beam is important to the detection of the signal and the data interpretation. For our purposes is used the Fresnel power reflection coefficient R. To quantify the fraction of reflected to incident power, we can use, for normal incidence,

$$R = \left(\frac{\sqrt{\varepsilon_1} - \sqrt{\varepsilon_2}}{\sqrt{\varepsilon}, + \sqrt{\varepsilon_2}}\right)^2 \tag{33}$$

The subscripts indicate the two materials. Moreover, variations in the terms of the permittivity can induce these changes:

$$R = \left(\frac{1}{4}\frac{\Delta\varepsilon_r}{\varepsilon_r}\right)^2 \tag{34}$$

$$R = \left(\frac{1}{4}\Delta(tan(\delta))\right)^2 \tag{35}$$

Where $\Delta\varepsilon_r = \varepsilon_1 - \varepsilon_2$, $\Delta\varepsilon_i$ is the change in the imaginary part, $\Delta(tan(\delta)) = \Delta\varepsilon_i \,/\, \varepsilon_r$. All of these considerations can be combined in the Radar equation:

$$P_r = \frac{P_t G^2 \lambda^2 \varepsilon_r}{(4\pi)^2 (2z)^2}\frac{R_r}{L} \tag{36}$$

The factor ε_r stands for the mean permittivity of ice. The factor z in the denominator, being the depth of the interface, results from geometric spreading. The second quotient considers, through the power reflection coefficient R_r, the reflection loss at the interface. The loss L includes attenuation

caused by impurities and reflection losses from inhomogeneities along the propagation path between the surface and the reflecting interface (Remote sensing of ice and snow; Rees, 2005; Remote sensing of glaciers: techniques for topographic, spatial, and thematic mapping of glaciers; Pellikka, 2009).

The loss of energy of the signal, already mentioned, is also caused by geometric spreading, and scattering (Reynolds, 1997):

$$a = \omega \left\{ \left(\frac{\varepsilon_r}{2}\right) \left[\left(\frac{1+\sigma^2}{\omega^2 \varepsilon_r^2} \right)^{1/2} - 1 \right] \right\}^{1/2} \quad (37)$$

'a' is the attenuation coefficient expressed in decibel (dB). The reflectivity is the one who causes the returned signals, but it also generates noise. To obtain good quality data is necessary to have a high energy returned to the receiver and to optimize the signal-to-noise ratio (*S)*. Is also important to consider that different materials have their refractive index, dependent on the permittivity (Arcone et al., 1995). To summarize, dielectric absorption occurs via conduction and relaxation which causes loss of energy through the oscillation and water molecules. Geometrical spreading depends on the distance traveled by the signal, causing the decreasing of the energy density transported by the wave proportional to $1/r^2$ (r = distance). Through this radar technique, we can separate the upper and lower surface of a glacier to determine the thickness, and its variations, along the satellite track (Weber and Andrieux, 1970). Is also possible to investigate the basal conditions of ice masses. For example, the roughness of a bedrock surface causes a diffraction effect when hit at different angles from the Radar, generating a change in the shape of the returned echoes. Combining this effect with a geologic knowledge we can determine ice motion, geological formations, subglacial debris, basal crevasse, and the presence of sub-ice lakes (e.g., Bailey et al., 1964; Drewry, 1981; Plewes et al., 2001).

Material	**Relative electrical permittivity (ε_r)**	**Electrical conductivity (σ) (mS m^{-1})**	**Velocity (v) (x 10^8 m s^{-1})**	**Attenuation (a) (dB m^{-1})**
Air	1	0	3.0	0
Distilled Water	80	0.01	0.33	0.002
Fresh Water	80	0.5	0.33	0.1
Salt Water	80	3000	0.1	1000
Dry Sand	3-5	0.01	1.5	0.01
Saturated Sand	20-30	0.1-1.0	0.6	0.03-0.3
Silt	5-30	1-100	0.7	1.100
Clay	5-40	2-1000	0.6	1-300
Granite	4-6	0.01-1	1.3	0.01-1
Ice	3-4	0.01	1.67	0.01

Tab. 4 Electrical properties of a variety of common earth surface material

Source: Plewes et al., 2001 Modified from Annan (1999)

4 DATA ANALYSIS

In this part, we will discuss methods, data, and programs that we used for the project. A series of MATLAB scripts were adopted for the analysis of satellite data, kindly provided by Orosei and his research group, and the results obtained were subsequently uploaded to ArcGIS to perform the interpolation, thus creating a 3D model surface of a part beneath Planum Australe.

4.1 RADARGRAMS

Giving the aim of creating a tridimensional model of the subglacial surface beneath the South Polar Cap, a variety of data collected by different instruments in past Martian missions have been used in this work. Thanks to the ability of the MARSIS signals to penetrate to the base of the glacier, the echo from the surface splits into two continuous traces as the spacecraft passes over the deposits. In fact, according to the Fresnel law of reflection, an electromagnetic wave traveling through a material gets reflected when it meets a medium with a different dielectric constant than the previous one. The greater the difference between the constants, the greater the intensity, expressed in decibel, of the reflected signal received by the on-board instrument. Therefore, a series of strong echoes represent the surface of the caps (interface air-ice) and another one the subsurface (interface ice-bedrock). In addition to this, layers of reflectors, due to the presence of dust layers that characterize polar stratified deposits, are also found within the caps. Keeping in mind the concept of remote sensing expressed in the previous chapters, the echoes collected are located based on their travel time (time passed between the emission and the reception of a wave in which it covered the distance spacecraft-surface). For every spacecraft orbit, there is a set of information such as its Keplerian parameters (Latitude and Longitude relative to the ground included) and the power of all the echoes collected with their associated time and relative frequency of the signal. The result of a series of elaborations is a Radar surface cross-section (Radargram), which displays all the reflected signals and their relative

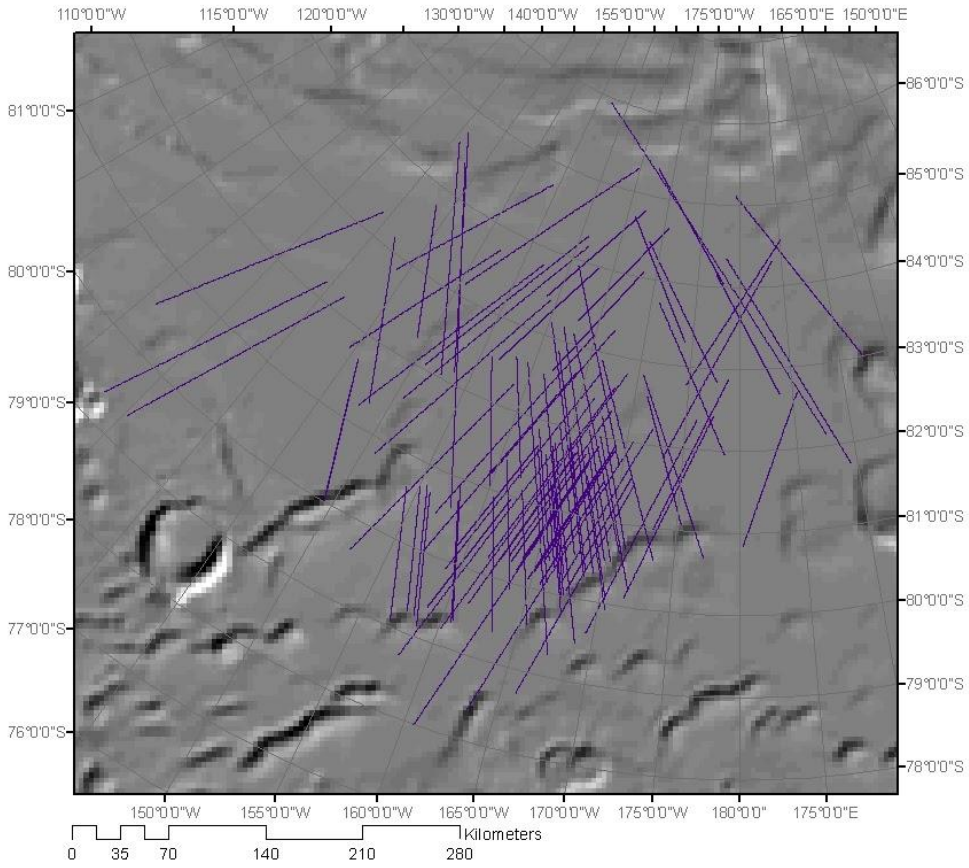

Figure 23 Selected Mars express probe orbits (89) over MOLA digital elevation model

intensity through a scale of shades of gray as shown in figure 24. Note that, in this case, the SAR technique has not been used for image processing, and that these are two-dimensional representations of reflected echoes.

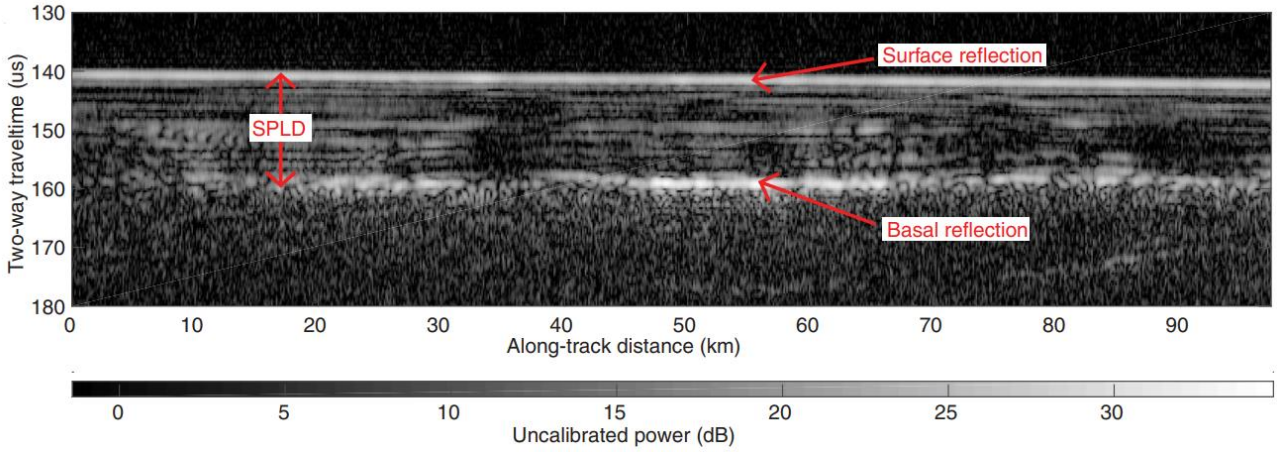

Figure 24 Radargram for MARSIS orbit 10737 in which the horizontal axis is the distance along the ground track of the spacecraft, the vertical axis represents the two-way travel time of the echo, and brightness is a function of echo power. The continuous bright line in the topmost part of the radargram is the echo from the surface interface, whereas the bottom reflector corresponds to the SPLD/basal material interface. Source: Orosei et al.,2018

For our purpose, a MATLAB script has been used to showcase these Images and to georeference each surface point. Unfortunately, not all of the Radargrams were of a quality suitable for interpretation; therefore, a group of 89 orbits has been chosen for this specific work, localized in Ultimi Lobe.

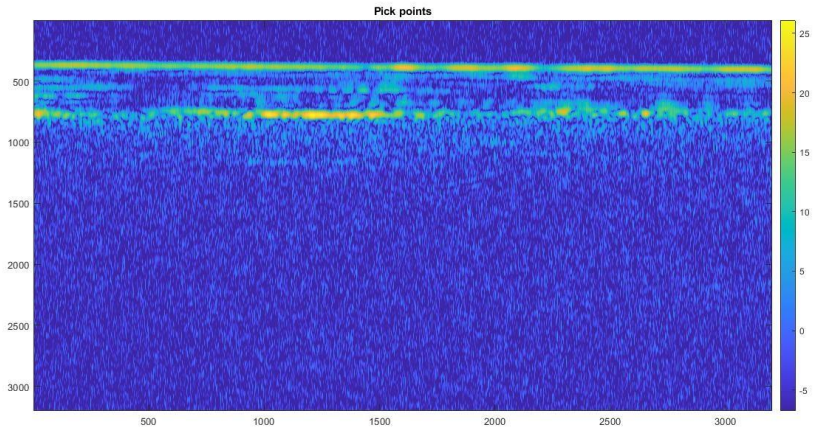

Figure 25 Representation of the Radargram in MATLAB through a color scale (on the right of the image) that goes from blue, for less intense echoes, to yellow, for the most intense echoes. The vertical resolution is eight times higher to make a better visualization of the image. The intensity of the reflected signal has a scale of values relative for each Radargram because it was not possible to calibrate the radar on the ground.

Furthermore, it is important to point out that the sections used belong to the same data set studied by Orosei et al., 2018.

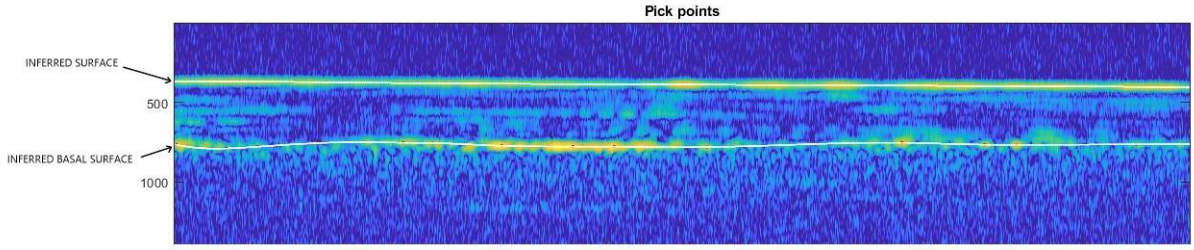

Figure 26 Radargram after the upper and lower surfaces (white lines) of the Cap have been 'drawn'

4.2 DATA PROCESSING CODE PROGRAMMING

To create a surface, we need to know the latitude, longitude, and elevation above a reference ellipsoid of a set of points. It is possible to derive this data set through the study of Radargrams in MATLAB. The written code, which we will briefly describe later, consists of a semi-automatic

procedure in which a user can derive the top and bottom surface of the polar cap represented by a matrix containing the reflection echoes located in space. In fact, as has already been said, the reflected signals with the highest intensity usually correspond, ignoring the presence of internal dust layers, to the air-ice and ice-rock interfaces.

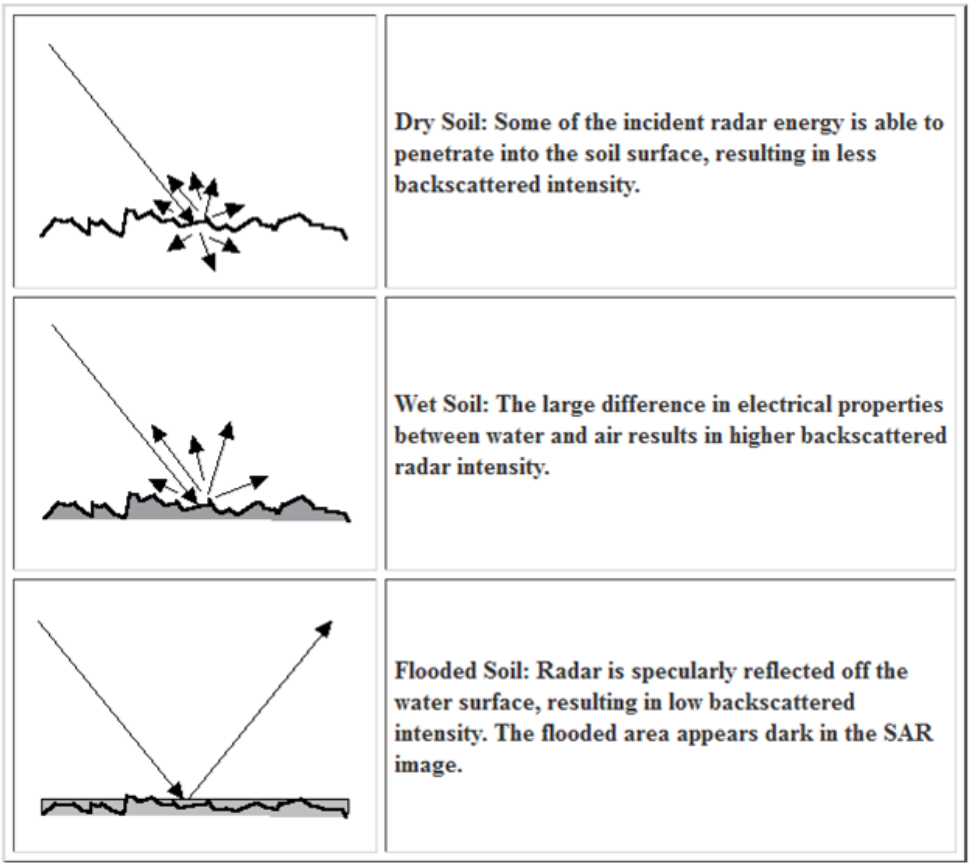

Figure 27 How signals get reflected based on surface roughness. source: http://gis.humboldt.edu/OLM/Courses/GSP_216_Online/lesson7-2/interpreting-radar.html

Different data sources and scripts were used for this study:

1. Radar surface cross-sections of Planum Australe from Mars Advanced Radar for Subsurface and Ionosphere Sounding (MARSIS), including a vertical timescale scale representing the time delay of the echoes.
2. Digital elevation model of the surface acquired by the Mars Orbiter Laser Altimeter (MOLA).
3. Code for retrieving the useful data from each Radargram.
4. Code for retrieving the elevation of the cap surface from the MOLA dataset.

Due to the loss of signal and presence of false reflectors, as a consequence of inhomogeneities within the medium and bedrock roughness (Fig. 27), a user's interaction with the program is required. The basic concept is to derive the bedrock elevation by making the difference between the calculated cap thickness and the elevations derived from the MOLA data.

The first step is then to obtain, through the script (3) for the interpretation of MARSIS data (1) provided by Professor Orosei, a matrix that represents the profile, each corresponding to an orbit of the satellite, of the cap. Using this method, each column will be associated with latitude and longitude, and each row will represent the depth expressed in time delay. The next step is to analyze, each one at a time, the Radargrams displayed. For better outcomes, the user can choose between two images corresponding to two different signal frequencies. In fact, image resolution depends on the signal frequency thus, we can pick the image that gives the best result and shows the lowest noise. The central core of this phase consists of outlining top and bottom surfaces. The user is asked to select a series of points that follow the morphology suggested by the most intense echoes. For each point selected, the program will correct the solution by repositioning the point at the maximum value found by analyzing 16 cells in a row. This number corresponds to the vertical resolution of the Radar, which is 15μs, divided by the time interval of a cell. The analog to digital converter frequency is 2.8MHz, which means that the radar echo samples are separated in time by an interval of $1/2.8\ 10^6$ seconds. Because the radargram is oversampled to highlight detail, this interval must be divided by the oversampling factor (8 as inferred from lines 59-64 of the script). So, the time interval between samples is: $dt = 1 / (8 * 2.86 * 10^6)$. When a sufficient number of points is selected, the program, through a cubic spline interpolation, draws a line representing the surface. The same process is repeated for the basal bedrock and then, the difference between the two lines gives the thickness (obviously, every value has an associated latitude and longitude). Another important step is to convert the number of cells for each column, representing the Glacier thickness located on the planet, in space expressed in meters. Several of the concepts used have already been explained in the section 3.2, but we will repeat them for greater clarity. Knowing the travel time and velocity of a signal emitted by an antenna, the space traveled can be derived from the following formula: $s=c*\Delta t/2$. The speed of light within a medium is lower than in the vacuum and is inversely proportional to the square root of the real part of the permittivity. The dielectric constant of the South Polar Cap varies based on the materials composing it and ranges from 3 to 4 because of the presence of dust particles. For this work, we used an average value of 3.5. We assume that, as has been done by Plaut et al.,

2007, the outlined surface follows a profile expected from MOLA topography. Therefore, for a given georeferenced dataset that we calculated, we retrieved the corresponding altitude obtained by The Mars Orbiter Laser Altimeter through another MATLAB script (4). Having the Cap Heights and its relative thickness, we can calculate the elevation above the ellipsoid.

4.3 THREE-DIMENSIONAL SURFACE MODEL

The MATLAB output is an excel file with subsurface X, Y, and Z coordinates. The set of points created represents the data collected along-track by MARSIS; therefore, we need to use the interpolation method to create a Digital Elevation Model (DEM). We have already mentioned interpolation previously, but it has not yet been explained what it consists of.

4.3.1 INTERPOLATION TECHNIQUES

In the mathematical subfield of numerical analysis, interpolation is a method of constructing new data points within the range of a discrete set of known points. The assumption on which the interpolation is based is that spatially distributed objects are spatially correlated; in a nutshell, things that are close together tend to have similar characteristics. This numerical method has found its utility in the geospatial analysis field, especially for creating Digital elevation models (DEM). DEMs are a useful application for geomorphological interpretations permitting experts to recognize terrain morphologies and estimate their causes. In our case, a DEM is represented as a raster, a grid of georeferenced squares containing an altitude value, also known as a height-map. GIS software gives the possibility to showcase a tridimensional terrain model, located in a proper reference system, based on these height values. Furthermore, this type of program includes numerical methods for interpolation. The most effective techniques for this work are:

- Inverse distance weighted (IDW)
- Kriging
- Natural Neighbor

These approaches rely on some basic statistical principles such as weighted averaging, which will be a recurring theme during the description of interpolation methods. All of the above were tested, but

only the Natural Neighbor, previously used by Plaut et al., 2007 in analogous research, gave decent results.

4.3.1.1 INVERSE DISTANCE WEIGHTED

The IDW technique computes an average value for unsampled locations using values from nearby weighted locations. The influence that each known point exerts over an unsampled one varies with the distance between them and depends on the power coefficient λ_i. Therefore, the value of a point is calculated in this way:

$$z(x,y) = \sum_{i=1}^{n} \lambda_i z\,(x_i, y_i) \tag{38}$$

Where n is the numbers of points in the surrounding considered, x_i and y_i are the coordinates of the known points. The weights are normed:

$$\sum_{i=1}^{n} \lambda_i = 1 \tag{39}$$

And depends on distance:

$$\lambda_i = \frac{\frac{1}{d_{iJ}^2}}{\sum_{i=1}^{n} {}^{1}\!/_{d_{i_J}^2}} \tag{40}$$

The symbol j refers to the unsampled location. As suggested by the exponential (2 is the most used) above the distances, the proportion between space and weight is nonlinear, which means that near points exert a stronger influence on a specific location. Despite its simplicity, the results were not

optimal because the inverse distance weighted method needs a rather uniform point distribution and suffers data clusters (Gimond M. ‘Intro to GIS and Spatial analysis’).

4.3.1.2 KRIGING

The kriging method uses the same weighted average of IDW except for the power coefficient determination. Whilst the inverse distance weighted technique considers only distances between objects, the kriging one takes into account the known points' spatial distribution. To quantify the dataset spatial autocorrelation, thus giving a value to λ_i, we need to create a fitted model to the measured points, calculate the distance to the prediction location, and estimate the spatial relationships among the measured values around the foresight position. Predictions are possible through a fitting model that estimates the general trend between the values of pairs of known points and their relative distances; therefore, defining the autocorrelation behavior. That being said, the first thing is to create an experimental semivariogram (also referred to as 'variogram') by the definition of γ.

$$\gamma = \frac{(z_2 - z_1)^2}{2} \tag{41}$$

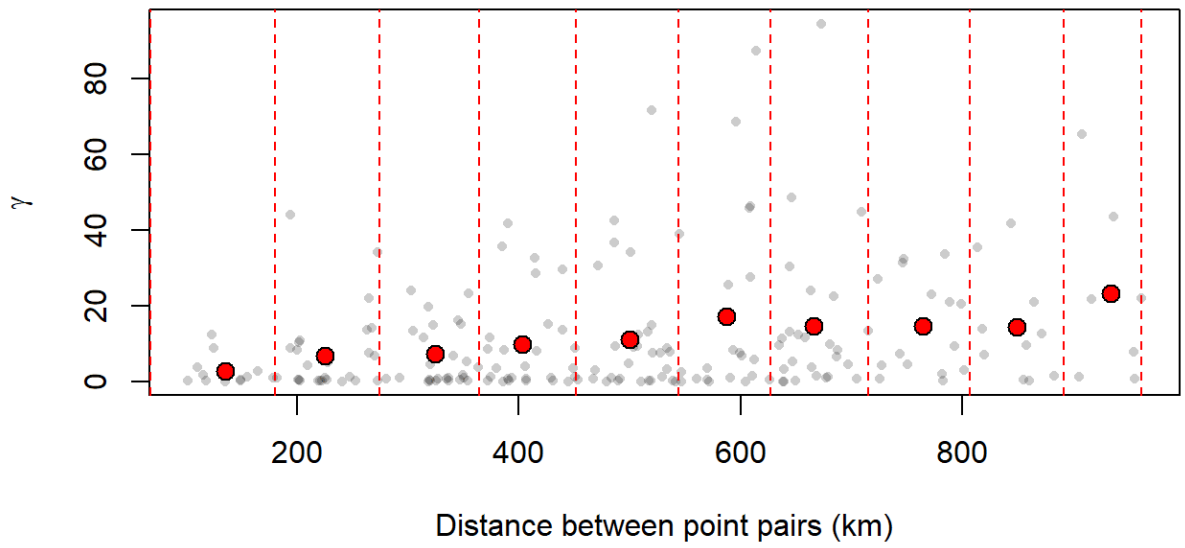

Figure 28 Sample experimental variogram plot. The dashed red line represents the intervals (lags) inside of which the average of the values is made (red points). Source: https://mgimond.github.io/Spatial/spatial-interpolation.html

We can compute γ for all point pairs then plot these values as a function of the distances that separate these points to understand how values change with range (Fig. 28). Inevitably there will be an extensive number of points that are difficult to handle, so we discretize the x-axis into regular intervals, the so-called lags, and calculate the average value within each. The points that summarize the cloud are the sample experimental variogram estimates for each.

Like in linear regression, it is necessary to find a fitting model for this plot to make predictions for the unknown positions, therefore, covering the value-distance relation for those x values that are not present on the graph. There are many mathematical models optimal for this purpose, and every software uses its own set. One thing to notice from the variograms is that the closer the two points are, the lower is their value difference. After we have uncovered the dependence or autocorrelation in the data, it is possible to make a prediction using the fitted mode (Fig. 29)l.

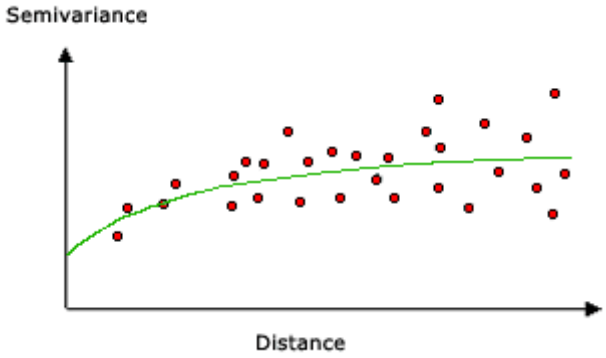

Figure 29Autocorrelation model (green line) based on the Exponential model. Source: https://pro.arcgis.com/en/pro-app/latest/tool-reference/3d-analyst/how-kriging-works.htm

Thereafter, the empirical semivariogram is set aside. In conclusion, whilst IDW uses only spatial distances for the power coefficient determination, the Kriging method uses the variogram model to compute the weights of neighboring points based on the distribution of those values. But despite its complexity, this interpolation technique did not give satisfactory results, differing little, qualitatively, from the method of inverse distance weighted interpolation.

4.3.1.3 NATURAL NEIGHBOR

Natural Neighbor is a method relatively easy to understand but rather difficult for a calculator to compute. The interpolation is made through the widely cited weight average, where the power

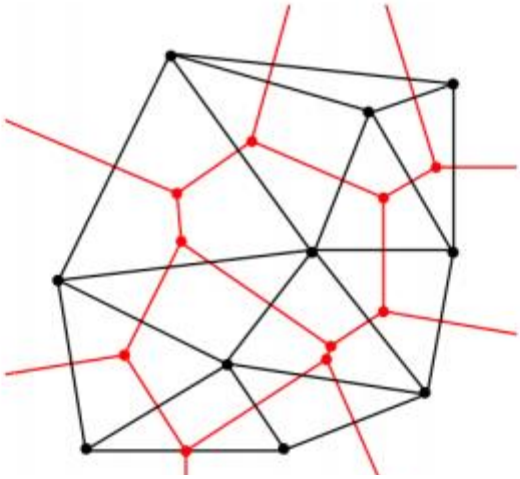

Figure 30 Voronoi diagram (red lines) built on Delaunay triangulation (black lines). Source: Hemsley, 2009

coefficient determination makes use of the Voronoi diagrams. A Voronoi diagram of a set of points is a composition of Voronoi cells (or polygons) surrounding those points, each of which describes an area of maximum proximity to the embedded point. To create these polygons, we must draw a segment between pairs of neighbor points following the Delaunay triangulation rule and then trace the bisector of each line. The intersections between the bisectors form the vertices of the polygons (Fig.30).

To weigh a new point, calling it x, we must draw a new Voronoi cell around the new location following the same principles as just described. This new surface (a volume in a tridimensional space) will be superimposed to the old diagram, therefore, it will intersect with the closest known points' Voronoi polygons. These intersection surfaces define the power coefficient.

$$\lambda_{p_i}(x) = \frac{\omega_{p_i}(x)}{\Sigma_i \omega_{p_i}(x)}$$

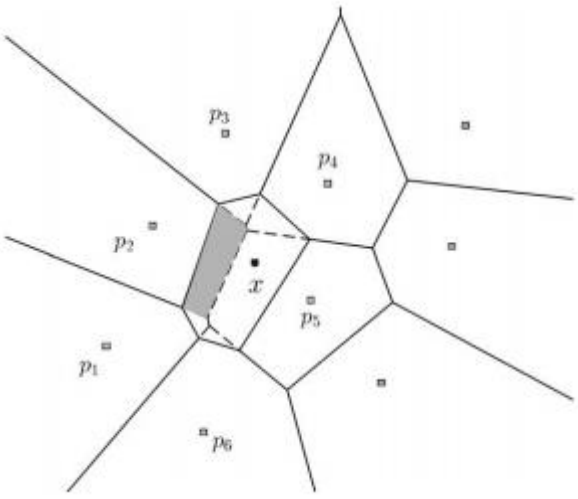

Figure 31 Example of a natural region in 2D. The natural neighbors of x are p1,...,p6. The natural region $\omega_{p_2}(x)$is shown in grey. Source: Boissonnat & Cazals, 2002

Where $\omega_{p_i}(x)$ is the shared area between x and a point $\boldsymbol{p_i}$ and $\Sigma_i \omega_{p_i}(x)$ is the sum of all the intersected area i.e., the area of the Voronoi cell of $\boldsymbol{x}$. In conclusion, as aforesaid, this was the technique used for the work.

5 GEOMORPHOLOGIC AND TOPOGRAPHIC ANALYSIS OF THE BEDROCK SURFACE

The whole process we used gave us two main models of the Ultimi Lobe region: 1) the local ice-sheet thickness and 2) the bedrock topography. It is important to underline that these models are far from being faithful reproductions of the exact morphometry of the southern ice sheet and the underlying bedrock. The presence of noise and false reflectors in the radargrams and low density of elevation points in certain zones allow us only to give an overall interpretation of the geomorphologies present on the basal plane and to use them to better understand some peculiar features that locally characterize the ice-sheet at the surface.

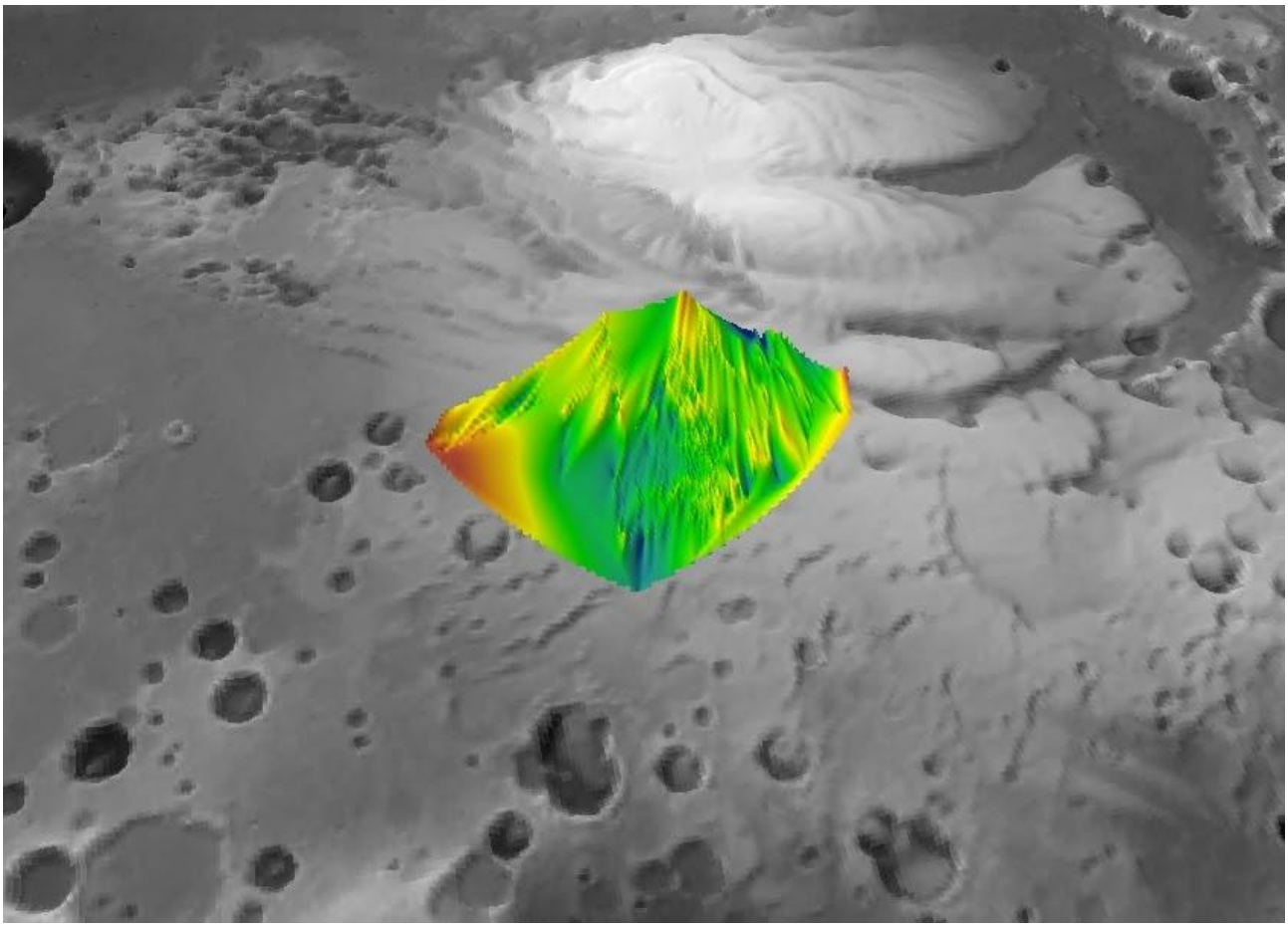

Figure 32 Our interpolated DEM (colored) above the MOLA digital elevation model (greyscale).

5.1 OVERALL MORPHOMETRIC AND TOPOGRAPHIC DESCRIPTION

The obtained bedrock surface extends from around 129°W to 163°E in longitude and from about 86°S to 78°S in latitude, covering an area of indicatively 152000 km^2 (Fig. 33). The wide-scale slope of this surface loses altitude from the highest to the lowest latitude (i.e., Northward). This result is consistent with the evidence that the southern ice-cap lies on a plateau characterized by an elevation higher than the surrounding terrain, as suggested by Fishbaugh and Head (2001). In particular, the bedrock elevation ranges from about 2 kilometers to 1 kilometer above the reference ellipsoid ('Mars 2000'). The average elevation value is 1386 km. As expected, ice-cap thickness is also generally decreasing toward the equatorial latitudes, namely moving to the Ultimi Lobe margins. Specifically, the ice-sheet thickness in the investigated area goes from around 1.8 km to less than 200 meters, with some uncertainties due to low density mapped radar points (Fig. 34 and 35). The average local thickness of the ice sheet is about 1373 km.

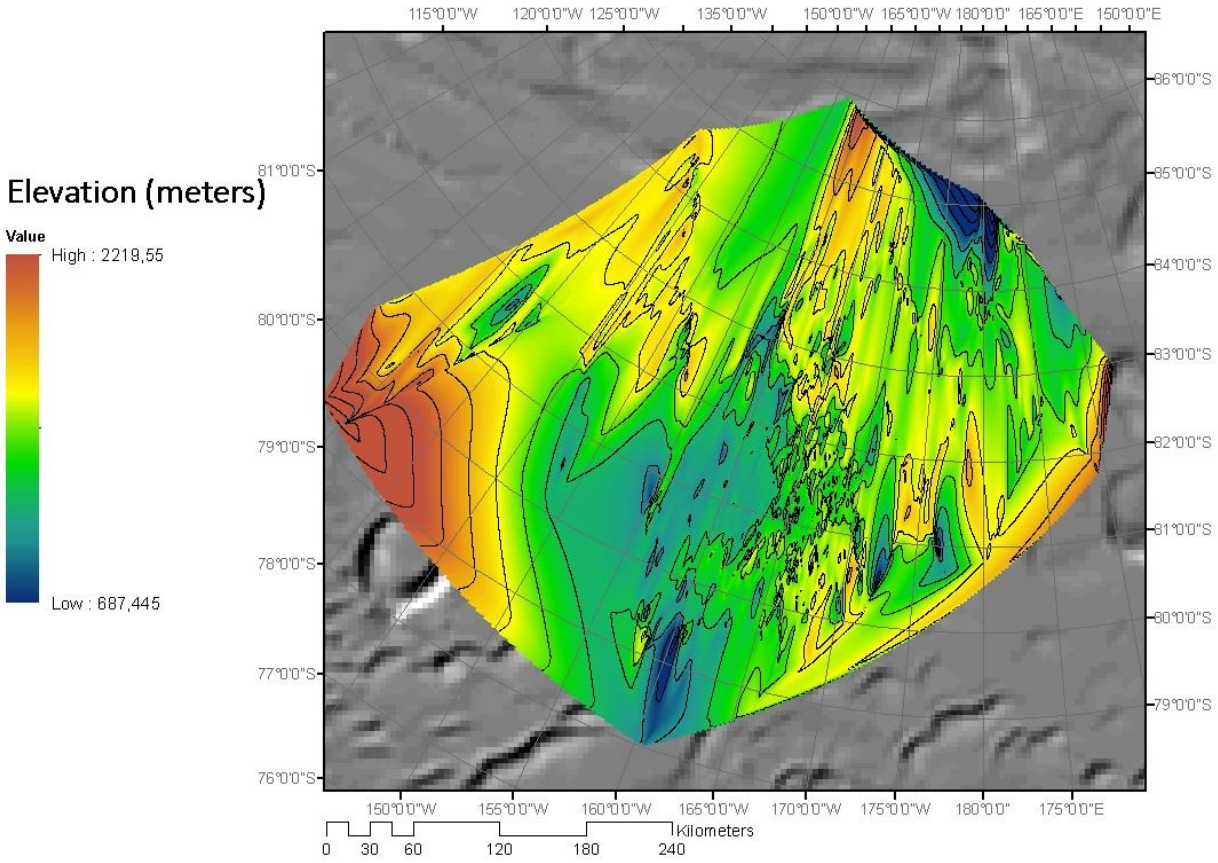

Figure 33 Digital Elevation Model interpolated in ArcGIS through Natural Neighbor method.

The bedrock surface is uneven, characterized by high-topographic features mostly on its eastern side and low-topographic features on its western side, whereas part of the narrow-scale morphologies in the central area is likely due to radar artifacts. A wide elongated depression occurs in the eastern part of the investigated area and extends from SE to NW (see Section 5.3). This depression follows fairly closely the topographic trend of the overlying ice-sheet, suggesting that some of the morphologies present at the base of the polar cap recur on the surface. Concerning this last point, a valuable observation is focused on some low topographies that are in coincidence with peculiar morphological features highlighted by Grima et al. (2011) at the surface and known as “Large Asymmetric Polar Scarps” (LAPS) (see following Section 4.2).

The analyzed dataset includes the lake district studied by Orosei et al. (2018), located around 193°E and 81°S in a 20 km wide area (see Section 5.4).

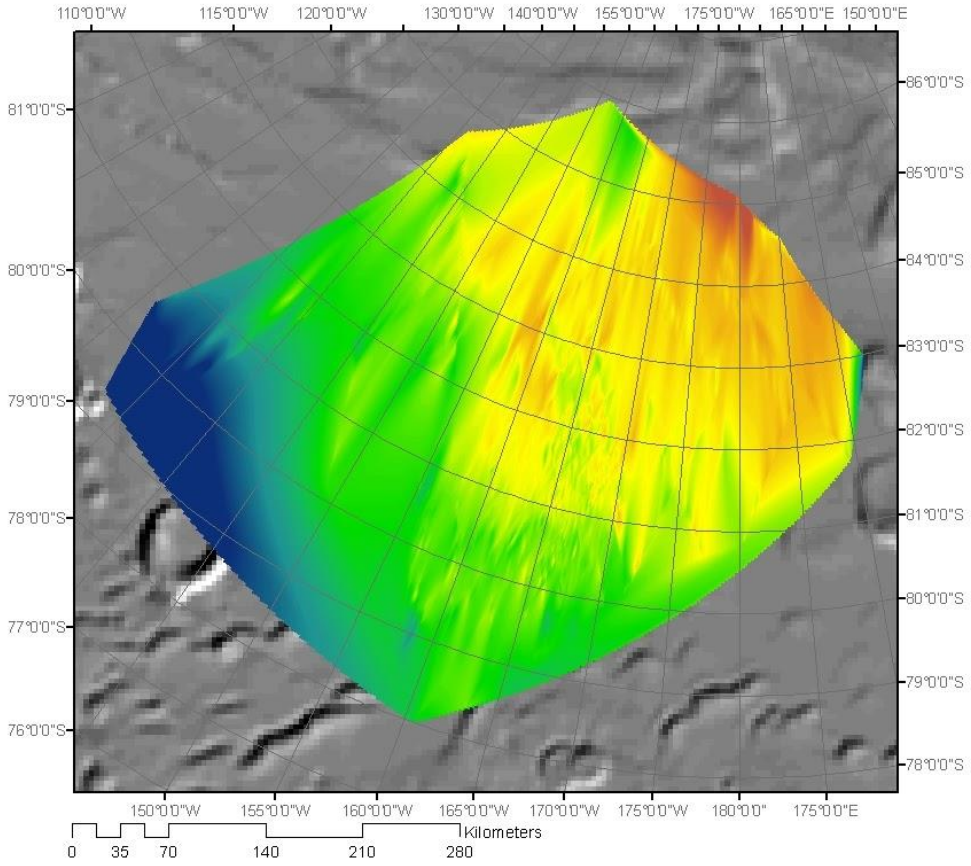

Figure 34 Representation of the thickness of the investigated area through color scale

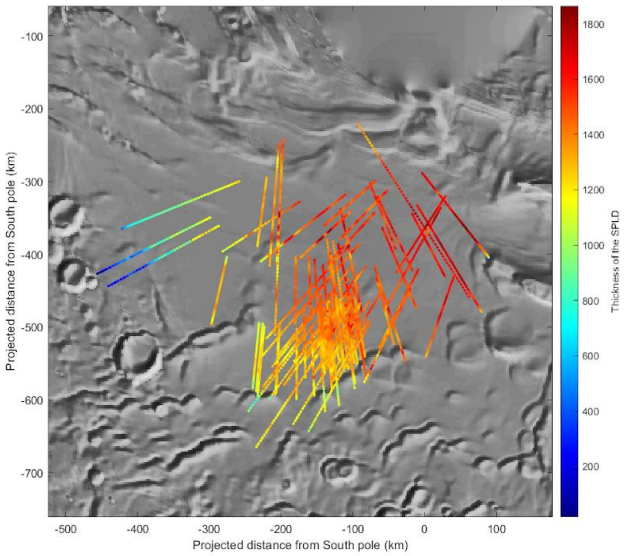

Figure 35 Ice Cap thickness values for each orbit

5.2 NEW EVIDENCE ABOUT LAPS FORMATION

A recurring characteristic of the elevation model of the bedrock is the presence of a series of discrete pits and depressions. It is reasonable to assume that these structures are not artifacts because they have a regular profile and are mostly present in correspondence of non-isolated orbits, ensuring a high density of mapped points and thus high reliability of the model. Most of these depressions are in correspondence at the surface with the aforesaid LAPS affecting the SPLD. As previously described (see section 2.2.2.3), these scarps, widely distributed among the Ultimi Lobe region (UL), are distinguished by their kilometric size and asymmetric profile. According to Grima et al. (2011), there are three possible interpretations behind their formation: 1) Uneven deposition of ice that filled an existing crater (or bedrock formation); however, this solution would not explain the spatial repetition and alignment of the LAPS; 2) Barchan dunes. Given the striking similarities of the LAPS morphology with Earth's barchan dunes (Howard 2000) and the heavy transport of dust by Martian wind in the UL region, together with sublimation, a long-term abrasion of the SPLD surface could be the cause for this kind of shapes (as described for the spiral troughs that characterize the polar caps of Mars by katabatic winds). This process could also explain the affinity between the LAPS orientations. Unlike the spiral troughs surrounding the north polar cap, however, the above

morphologies are not necessarily oriented toward the Sun and are all found in a single portion of the southern ice-cap (and not over most of it, as expected for dunes); 3) Tectonic scenario. According to topographic and SHARAD analysis, the LAPSs profile is similar to listric normal faults (Fig. 36), characterized by a steeply dipping scarp facing a gentle flexure that flattens with elevations. On Earth, these faults occur in extension zones (e.g., rift) where there is a main detachment fracture following a curved path rather than a planar path. Their hanging-wall surface is concave upwards, with its dip angle decreasing with depth, thus creating a syn-tectonic rollover anticline. This effect is a consequence of the gradual bending of its strata moving along the normal fault, with the horizontal component of movement increasing with depth.

The profiles of the LAPSs, shown by SHARAD and MARSIS, have a shape typical of those portions of the crust affected by extensional movements.

Figure 36 LAPS profile collected by SHARAD. Vertical scale multiplied by 30 to emphasize the subsurface echoes. Source: Grima et al.,2011

As a result, Grima et al. (2011) have thought that some listric faults locally crosscut the UL ice sheet, resulting in surface to LAPS morphologies. According to the authors, the regional UL ice-

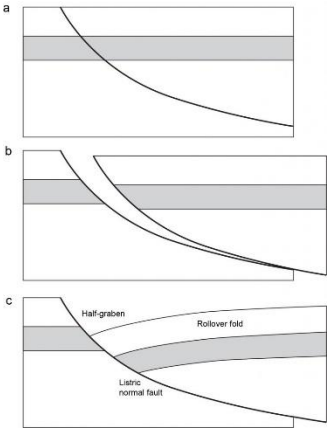

Figure 37 schematization of listral fault formation. Source: https://openeducationalberta.ca/introductorystructuralgeology/chapter/l-tectonic-environments-of-faulting/

sheet flow and slide on a geological time scale (maybe favored by the presence of incompetent basal sediments, softening salts, basal sediments mixed with water, etc.) could have provided the extensional stress necessary to form listric normal faults.

About the tectonic scenario, new evidence provided by our analysis allows us to propose two alternative hypotheses on the LAPSs origin. These features coincide with our surveyed low topographies affecting the buried bedrock. According to the modeled data, most of the assumed faults are also oriented in the same direction (they are sub-parallel) and are characterized by exposed steep scarps (i.e., the length of the LAPS may correspond to the exposed fault plans). These elements suggest that (as possible alternatives): 1) Pre-existing topographic depressions in the bedrock (such as impact craters, basins, or valleys) could locally have triggered extensive stress enhanced by gravitational collapse of the overlying icy layers. This allows the formation of tectonic synthetic extensional faults and deformations in the SPLD, able to intersect the surface, forming the LAPSs

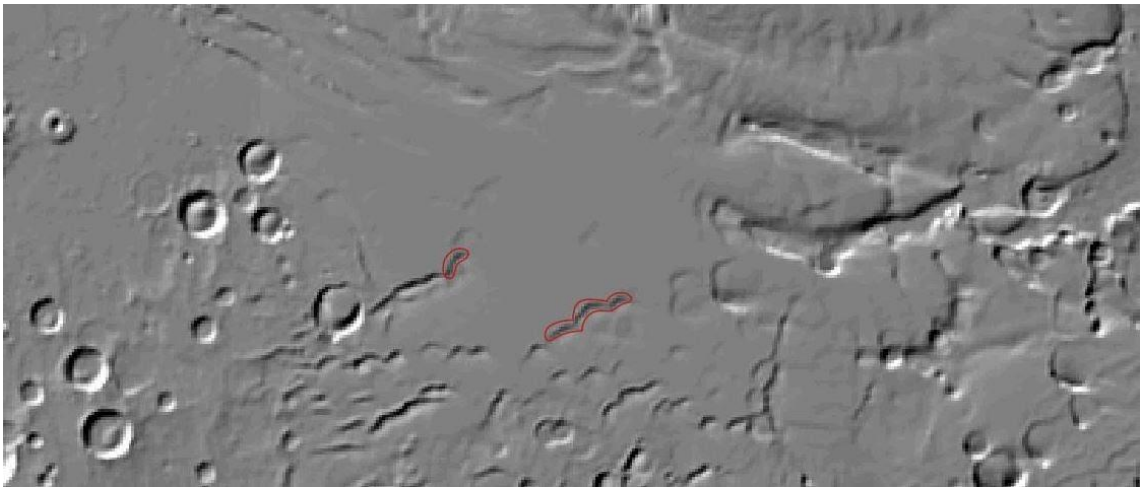

Figure 38 In red are indicated the LAPS observed in our model

scarps; 2) In some cases, the topographic analysis of the modeled bedrock profile at the base of LAPS also shows conformity with the profiles at the surface in the ice. This could suggest that normal faults affect the bedrock as well. A possible explanation is that, in coincidence with the existing bedrock low-topographies, the UL ice-sheet overload caused the rupture through faulting of the scarps confining the bedrock depressions and that these faults elongated up to the ice-sheet surface.

More generally, we could infer that the movement of the ice cap along an uneven crust topography may have led to differential stress from place to place, resulting in leeward in a series of normal

same-oriented faults or system of faults. Alternative hypotheses about the origin of these normal-faults systems are totally unlikely. On Earth, systems of parallel normal faults and listric faults are present in the proximity of passive margins, outlining the transition between oceanic and continental lithosphere, related to extensive crustal motions in the vicinity of rifts. This would mean that the South Pole is crossed by divergent margins, along which two plates have moved away from each other in the past. However, a tectonic plate activity should display a vast range of structures that are nowhere to be found on Planum Australe (for example, horst and graben structures, volcanisms, and so on). Furthermore, the process of relaxation driven by the rise of magma, due to convective movements, causes a thinning of the crust which, for the principle of isostasy, tends to be at lower altitudes than the continental margin. Evidence of this sort does not appear to be present in sufficient numbers to reliably identify tectonic plate margins on the red planet, in general, and at the South Pole, in particular. Only some have theorized that it might be present along the dichotomy boundary, especially in Valles Marineris (Yin 2012).

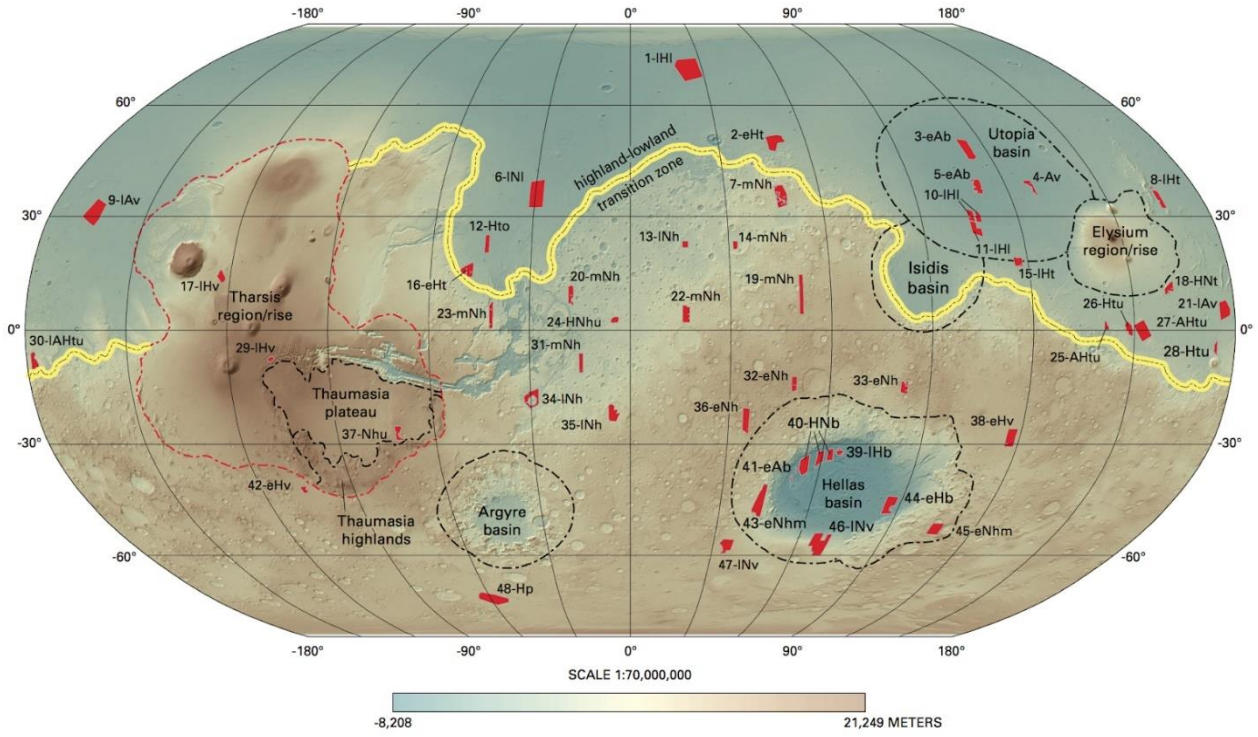

Figure 39 Topographic map of Mars showing the highland-lowland boundary marked in yellow, and the Tharsis rise outlined in red (Tanaka et al., 2014)

Despite the lack of evidence of rifting in the UL region, a local tectonic movement disconnected from the process of oceanic ridge formation may still be plausible.

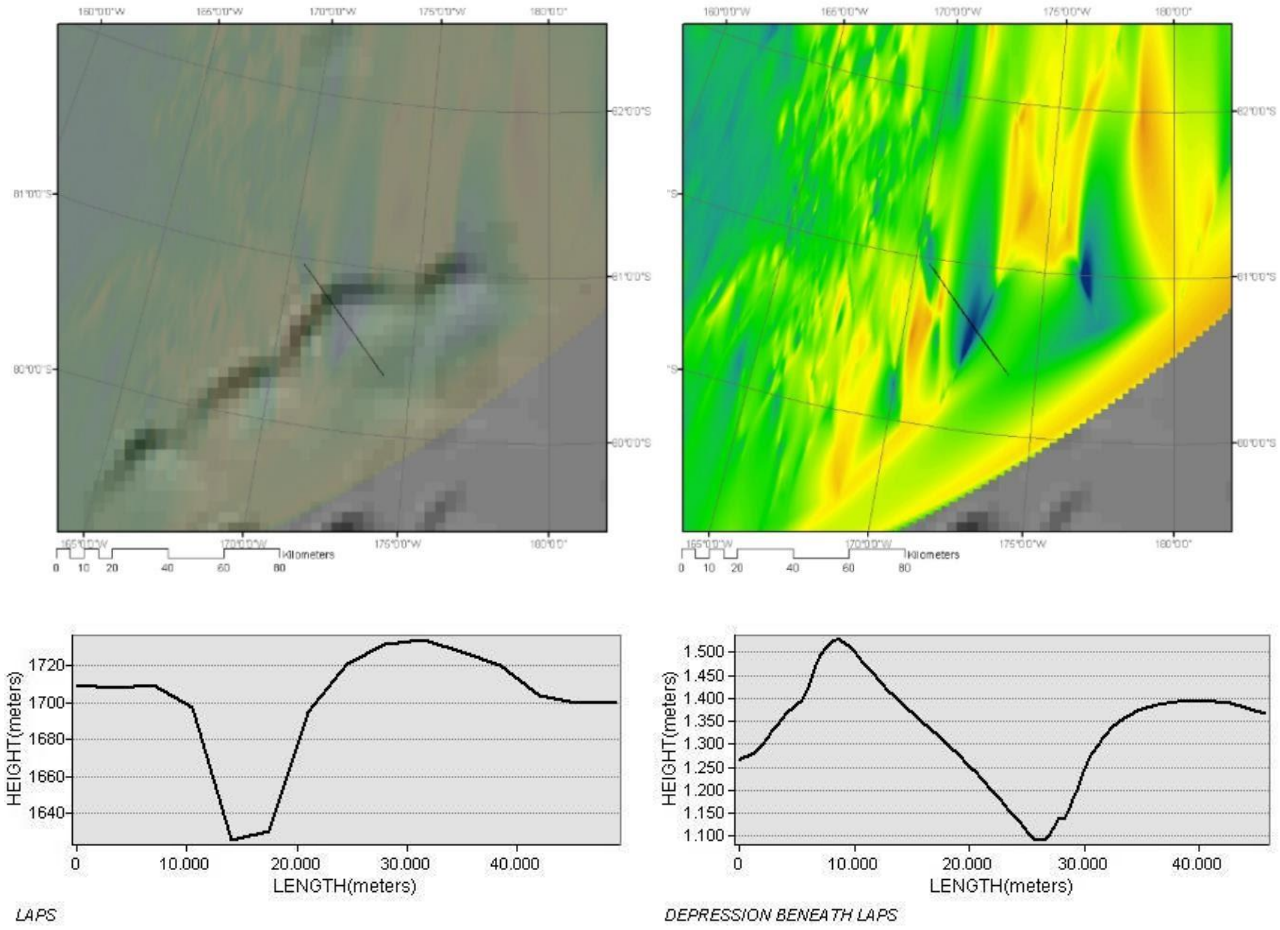

Figure 40 Below are profiles of one LAPS at the surface (left) and the associated depression in the bedrock (right). Above are the respective tracks (black lines, left to right).

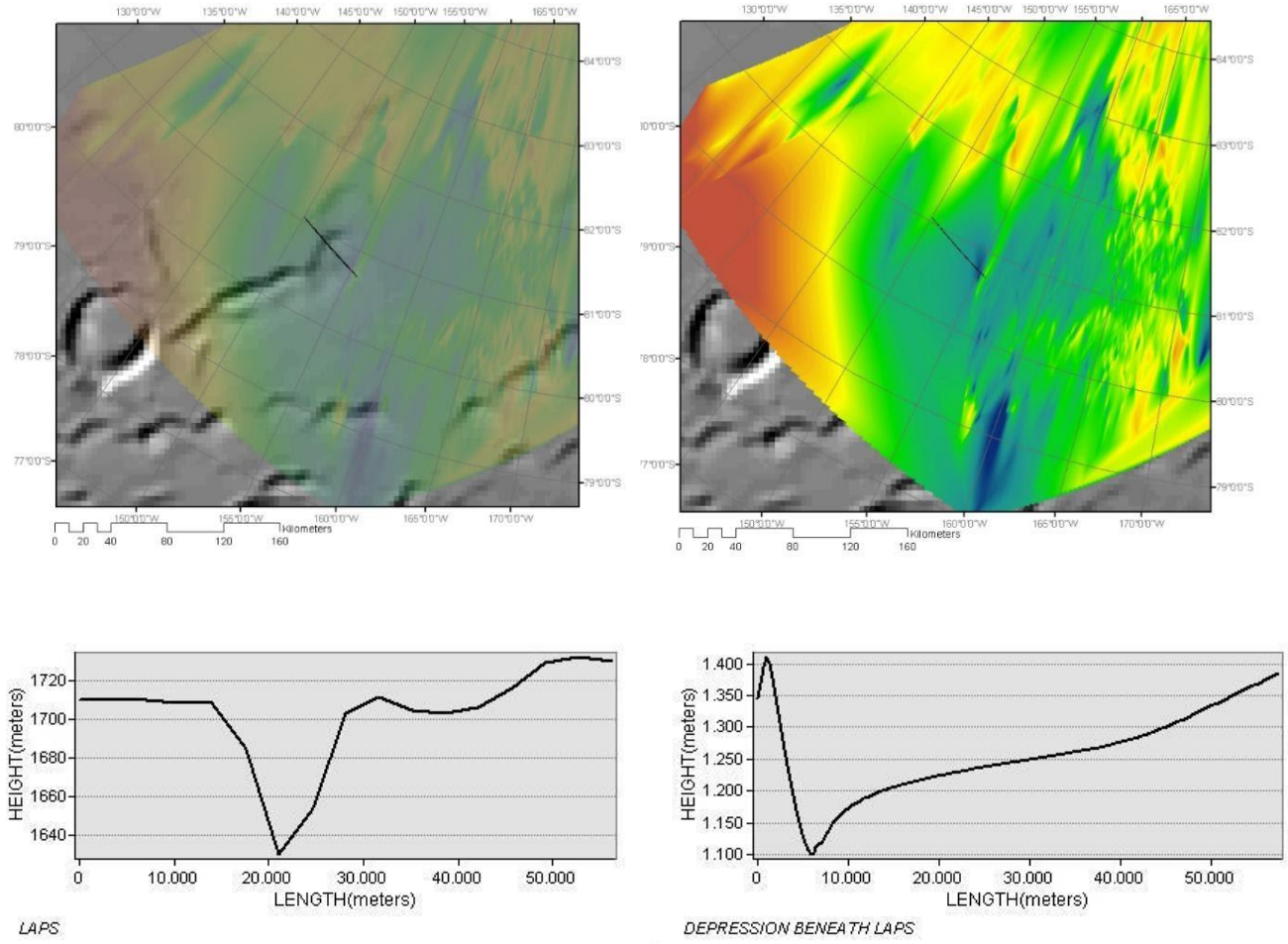

Figure 41 Below are profiles of one LAPS at the surface (left) and the associated depression in the bedrock (right). Above are the respective tracks (black lines, left to right).

5.3 ANALYSIS OF POSSIBLE GLACIAL MORPHOLOGIES

The most peculiar topographic feature at wide-scale arising from the interpolated bedrock surface is a broad depression that extends roughly from 83°S to over 78°S in latitude and from 170°W to about 155°W in longitude (Fig. 42). Although its margins cannot be determined with precision because of the uncertainties of the data, this low-topographic has a roughly elongated shape, about 275 km long and with variable width (it is 63 km wide in its southernmost portion, 93 km in its northernmost part, and 148 km in its central one).

On average, the floor of this depression is less than 1 kilometer lower than the surrounding terrain. At a narrower scale, its surface appears to be characterized by high and low topographic features, extending from SE to NW, showing an elongated shape and parallel to each other. Generally, these

structures have extensions of tens of kilometers (up to almost 90 km maximum), and elevations of few tens of meters up to some hundreds. According to their topographic longitudinal profile (Fig. 47,

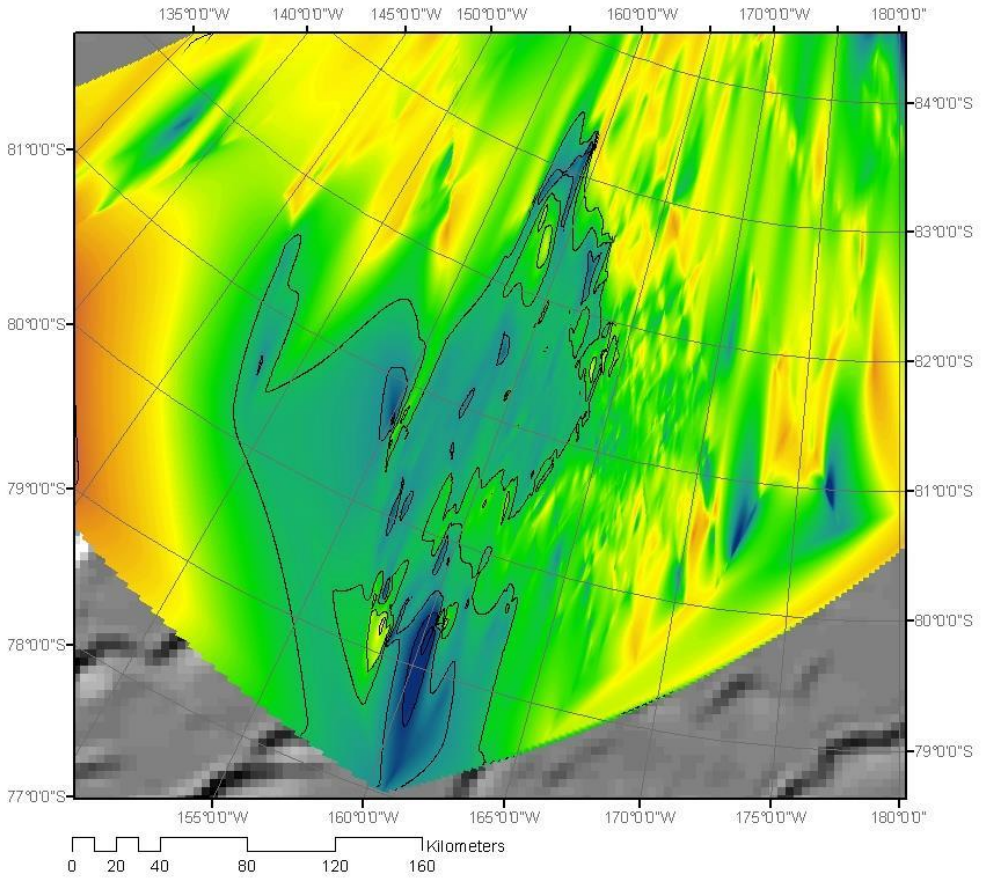

Figure 42 Highlighted by the black line is the depression located in the western portion of the model.

48, 49), the angles of inclination of their scarps do not exceed one radian.

As mentioned before, in general, we cannot exclude that some of these morphological features could be affected by artifacts due to the interpolation algorithm and approximations in the data collection. However, it is reasonable to assume that, given the good number of sampled points in this sector of the investigated area, the observed structures are to a first approximation real.

Given the regional context, we hypothesize that these shapes can be related to glacial processes. In general, at their bottom, the movement of glacial-tongues can create a variety of typical shapes at different scales as a result of erosion, abrasion, and deposition of rock sediments, associated or not with meltwater. The erosion capacity will depend on several factors, such as mainly: 1) The hardness of the transported sediment relative to the basement; 2) The amounts of transported material; 3) The ice and/or water-flow velocity, and 4) The levels of turbulent flow in case of flowing water. Among all these processes, glacial abrasion is the most efficient in eroding and transporting rock particles to

the base of a glacier, moving them across the bedrock surface. About abrasion phenomena, two models describe the degree of erosion glaciers cause as a function of some parameters. 1) Boulton model. The effectiveness of the process is directly proportional to the effective normal pressure (the force per unit area imposed vertically by a glacier on its bed), which is due to the pressure perpendicular to the plane and the basal water pressure that opposes the effect caused by the weight of the glacier through the buoyancy effect. The value will be higher with thick ice and low basal water pressure. 2) The Hallett model. It is based on the idea that the sediments are surrounded by the ice, so the pressure between a clast and the glacier bed is a function of the rate at which the ice flows over it. Therefore, abrasion depends on basal melt rate and the presence of extending glacier flow. In general, glacial erosion is most effective with warm-based glaciers where there is a greater amount of meltwater. In this case, fluvioglacial landforms are coupled with glacial ones.
Mainly through the aforesaid erosion processes, several landforms at different scales can occur. The main and typical structures of glaciers at macroscale are "U-shaped" valleys, which presents steep clear walls that gently bend towards the base ending with a wide flat floor (on the contrary of "V-shaped" fluvial valleys).

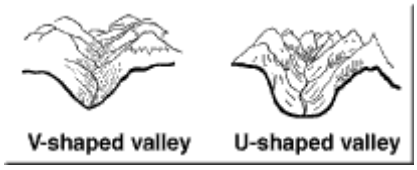

Figure 43 Scheme of V-shaped and U-shaped vallyes

As described before, in correspondence with the most reliable dataset, our bedrock model shows a broad elongated valley. This is characterized by the flattening of the base of the polar cap flanked by walls that increase in steepness as one moves away from the depression, as shown in the figure 45 ("U-shaped"). Thus, we can assume that glacial erosive processes carved it (it could be a glacial valley). At the same time, the valley floor is characterized by high-topographic narrow-scale

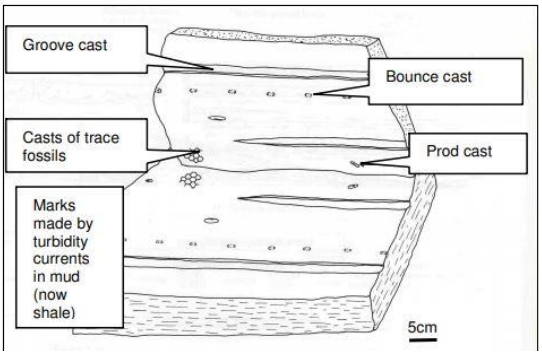

Figure 44 Representation of various types of grooves. Source: https://www.earthlearningidea.com/PDF/179_Sole_marks.pdf

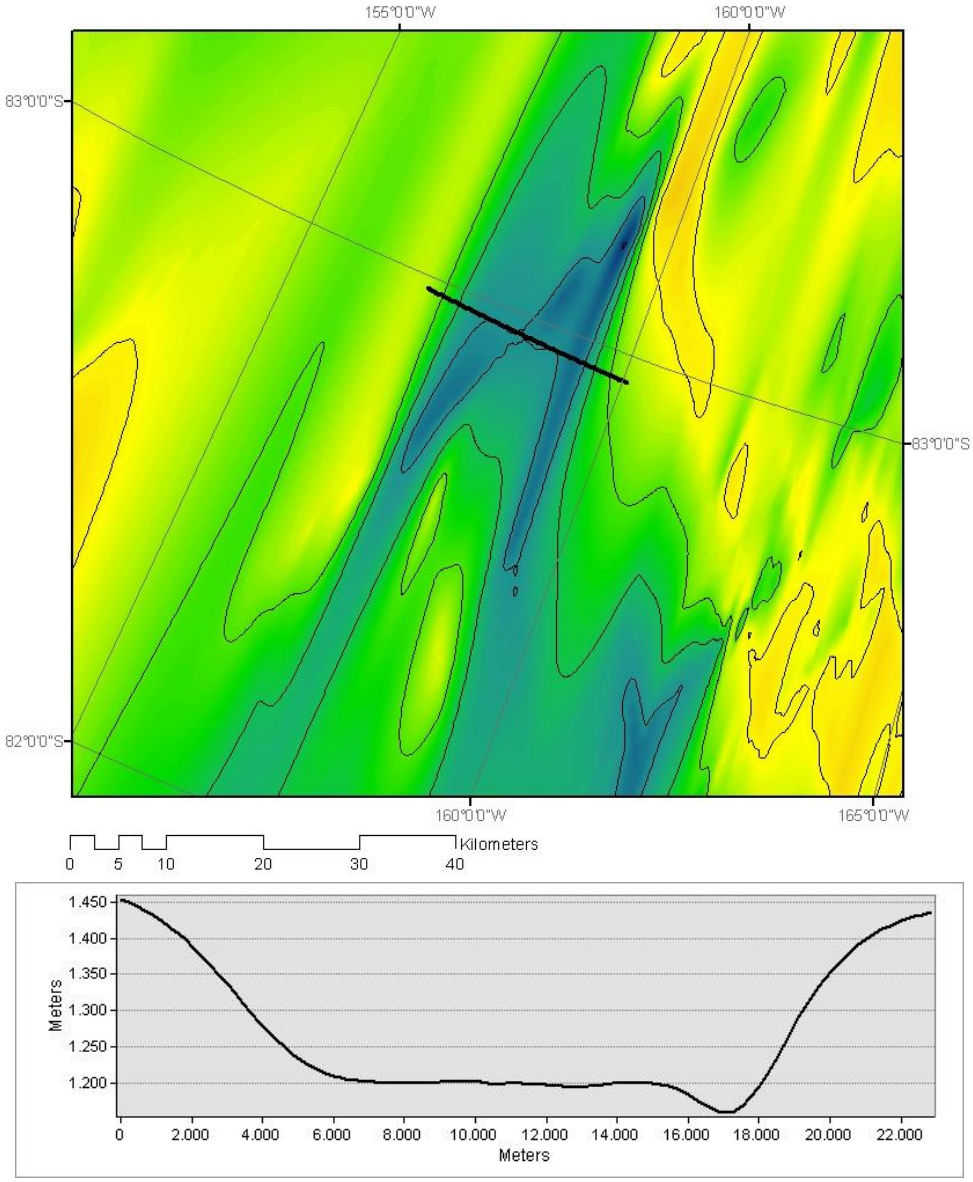

Figure 45 At the bottom is the section of the depression (similar to a U-shaped valley profile) at the top is the trace of the profile (black line, left to right).

morphologies that are all iso-oriented according to the inferred ice-sheet movement. On Earth, it is well known that ice-sheet movement at their base causes transport and subsequent deposition of debris (forming elongated hills, known as drumlins), the formation of striations, scours, groove cast, Roche moutonnée, and so on. Some of these structures could be consistent with the analyzed Mars surface (although we can only identify kilometer-scale morphologies due to the resolution of MARSIS).

In particular, through the observation of the profiles traced along the most representative ones, some similarities can be noted with some of the subglacial structures observed on Earth. Assuming a

South-North sliding direction of the local Ultimi Lobe ice-sheet, and considering that the bedrock surface decreases in altitude toward the equator and that it is slightly inclined in this direction, we can make some considerations, for instance:

1. The topographic profile They can also be observed at large scales and are often indicative of warm-based ice carrying debris that is slowly flowing of selected high-topographic streamlined features (as shown in the figure 47) presents analogies with some morphologies known as 'Whalebacks'. These are rocky knolls smoothed on all sides, elongated along the direction of glacier flow, as a result of abrasion. due to low basal meltwater. The profile is delineated by an upwind portion with a steep slope and a downwind one with a shallow slope. On the other hand, and this time from a depositional perspective, structures with a similar profile can be related to drumlins. Unfortunately, their mechanism of formation is unclear, but the most widely accepted idea is that they are deposits formed when the ice became overloaded with debris. Their scarps are affected by the phenomenon of quarrying (and abrasion), which 'rips' off portions of the downwind portion (Lee) while the upwind part (Stoss) is smoothed. For this to happen, there must be fluctuations in the values of normal effective pressure acting on the ice so that it can melt and then refreeze. Assuming a northward glacier slip orientation, the profile in the figure 48 can be associated with this category of shapes. Alternative hypotheses are 'Roche Moutonnee' and Crag and Tail features. This latter, however, unlike the 'Roche Moutonnee', are larger and have a symmetrical profile. In general, we can say that these morphologies are due to portions of bedrock harder than the rock that surrounds them, therefore characterized by a lower rate of erosion than the glacial bed. Based on the available information, it is impossible to define the exact process at the base of the observed elongated hills in the modeled bedrock. The same morphology can be related to different known landforms, having different explanations of formation. For example, ‘Roche Moutonnee’ develops where the ice is fast-flowing and relatively thin, conditions that are ideal for cavity formation, whereas whalebacks occur only under thicker ice.
2. The elongated hills we observe are also associated with scours (figure 49). Again, as known glacial erosional processes can excavate bedrock, forming features similar to those observed. That could be the case of mega grooves, characterized by large scale (kilometers) linear channels eroding bedrock by the passage of ice, possibly by plucking (the moving of ice can

be coupled with abundant basal meltwater (Bennet, Glacial geology: ice sheets and landforms).

In conclusion, given the context and similarity of some of the terrestrial glacial structures with the morphologies present on our basal surface model, we can infer that a portion of the Ultimi Lobe ice-sheet (in particular, some ice-tongues moving from the ice-cap) was affected by flow and/or basal sliding. In particular, the orientation of what could be morphologies caused by erosion and glacial deposition (protuberances and oblong depressions) inside a possible U-shaped valley indicate that the flow occurred from South-East to North-West. This conclusion is also consistent with the presence of faults related to LAPS, in turn, referred to as ice-sheet flow and/or sliding.

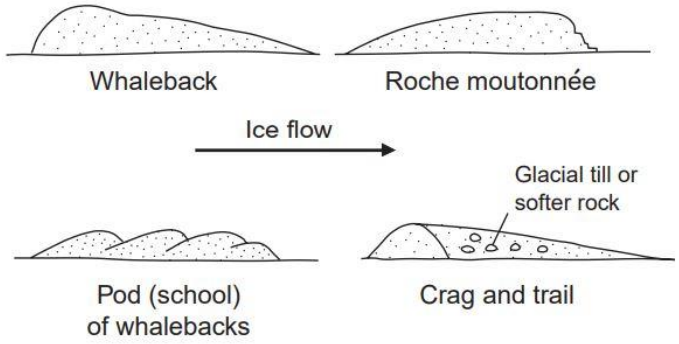

Figure 46 Representation of named glacial morphologies. Source: Glacial geology: ice sheets and landforms, Bennett and Glasser,2011)

Furthermore, if confirmed in future studies, some of the observed structures can be consistent with the presence of water at the base of the ice-cap in geologic periods. According to already cited recent studies (Orosei et al., 2018 and Lauro et al., 2021) this Martian region is the seat of localized buried subglacial water ponds that could be remnants of past ice melting, especially in the topographic lowlands that characterize the observed basement.

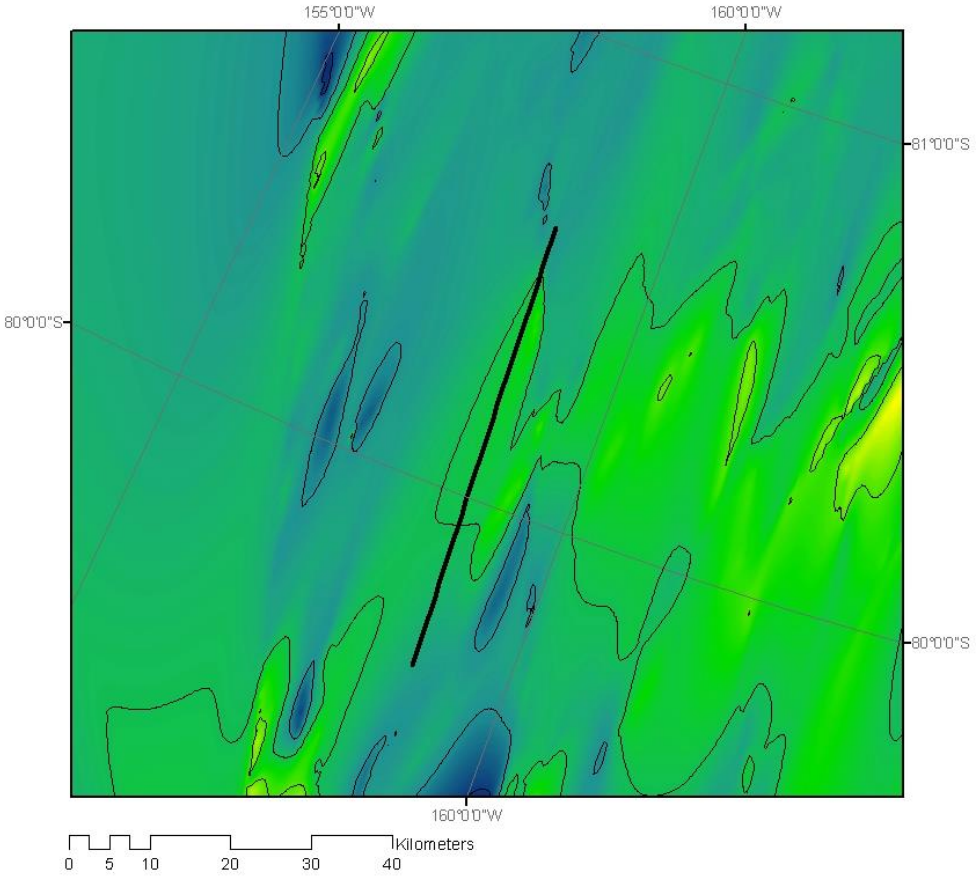

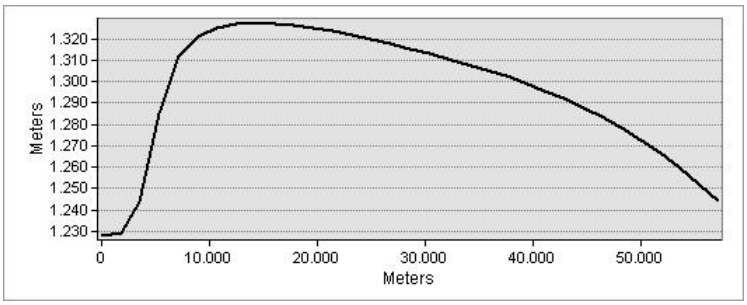

Figure 47 At the bottom is the section of an elongated structure (similar to whalebacks and drumlins) at the top is the trace of the profile (black line, top to bottom).

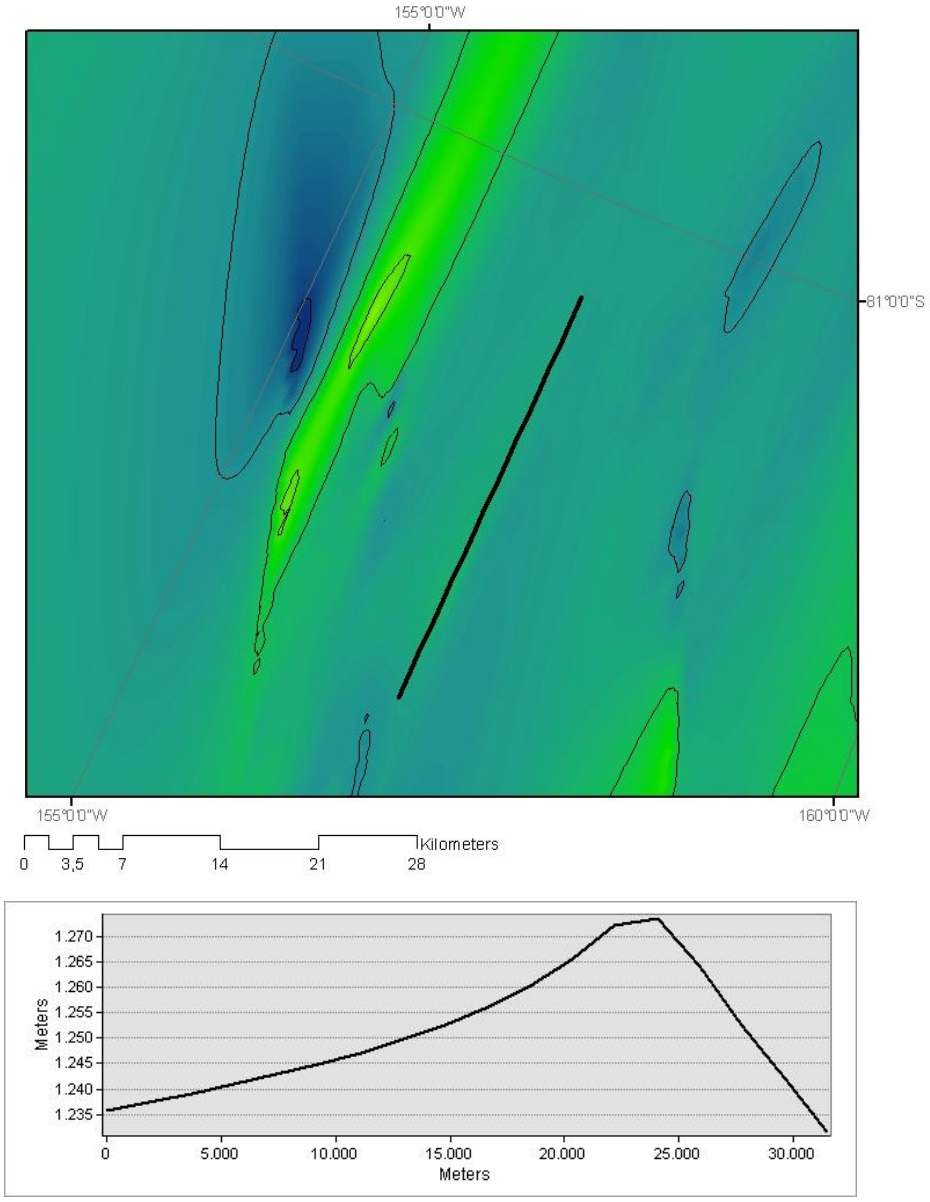

Figure 48 At the bottom is the section of an elongated structure (similar to Roche Moutonnee) at the top is the trace of the profile (black line, top to bottom).

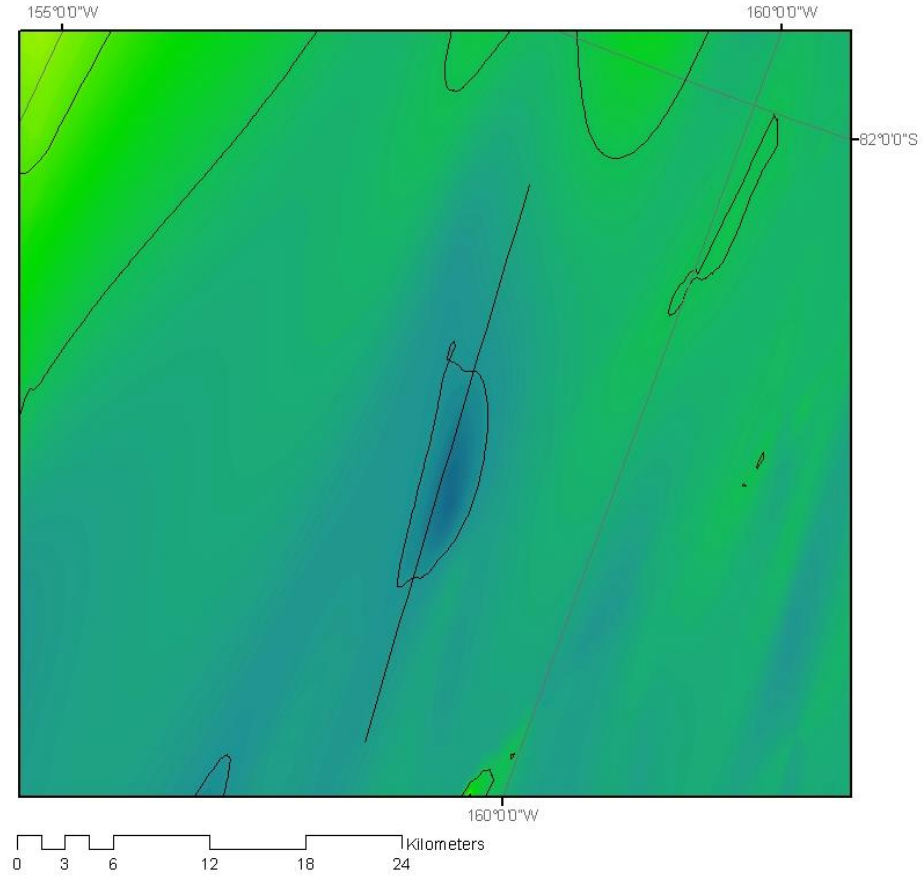

Figure 49 At the bottom is the section of an elongated structure (similar to mega-grooves) at the top is the trace of the profile (black line, top to bottom).

5.4 SOME CONSIDERATIONS ABOUT THE "SUB-GLACIAL LAKE DISTRICT" BEDROCK TOPOGRAPHY

As mentioned, the high reflectivity displayed by MARSIS radargrams indicates the presence of liquid water in the study region of UL (Orosei et al., 2018). In addition to this, a wider network of subglacial lakes close to the first water reservoir has been suggested by Lauro et al. (2021). Through

the observation of our model in the vicinity of the aforesaid area, we can note an uneven topography, with plenty of topographic highs and lows. In particular, although the large along-track footprint (~5 to 9 km) of MARSIS and errors in data collection and analysis does not provide high-resolution models of the bedrock morphologies (strongly limiting its ability to discriminate structures related to subglacial water), we can define some mild depressions (low topographies) in coincidence with the

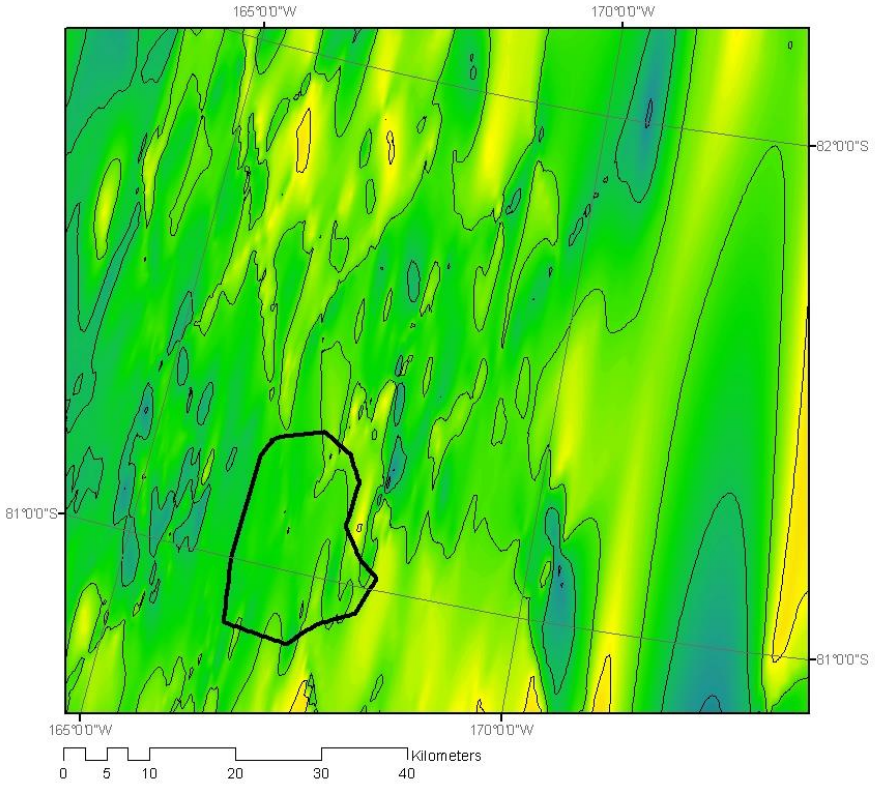

Figure 50 Framing of topographic highs and lows. Black line indicates the lake discovered by Orosei et al. (2018).

inferred lake district.

These bedrock lows surround the lake district and are present in large numbers in the southernmost portion of it. This is consistent with a favorable environment for water reservoirs, whether they exist in the present or not. This network of depressions may have been in the past (but also still now) the ideal place for the accumulation and outflow of subglacial waters. This observation contrasts with the Arnold et al. (2019) study according to which the lake identified by Orosei et al. (2018) would be an isolated basin caused by a local geothermal anomaly (Sori & Bramson, 2019). Nevertheless, further simulations need to be undertaken to improve our understanding of the regional water flow.

Furthermore, the observation of variations in the local thickness of the ice above the “lake-region” seems again in favor of the presence of subglacial water. In particular, the local thickness of the ice-sheet above the lake district is decreasing relative to its surroundings and shows a relative depression. This is consistent with what is observed on the ice-cap surface on Earth in correspondence with some subglacial lakes (e.g., Vostok lake in Antarctica, e.g., Siegert and Ridley, 1998).

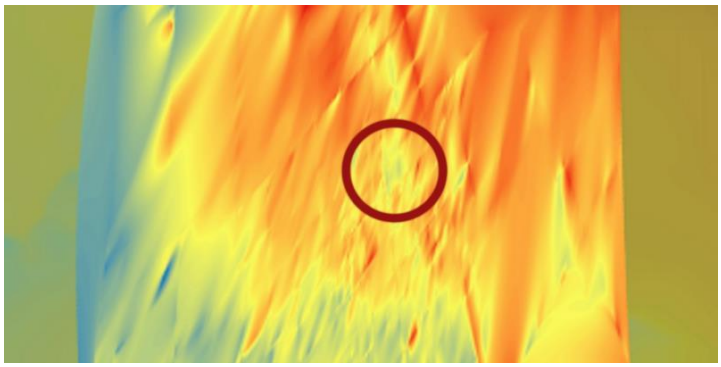

Figure 51 The red circle indicates the relative location to the lake (Orosei et al., 2018). The blue coloration of the map indicates relatively lower thickness values than the red and yellow colors

More in-depth studies are needed to better understand what this area might be hiding, and which kind of geological processes characterized it. However, given the consistency between the observed evidence all suggesting the same result, the presence of water under the UL ice-sheet seems to be confirmed by our morphological study of the buried bedrock.

6 CONCLUSIONS AND FUTURE PROSPECTS

The creation of a Digital Elevation Model surface obtained from the analysis of MARSIS radargrams through an innovative semi-automatic mapping algorithm allowed us to expand the knowledge about the South Pole of Mars. In particular, this work aimed to analyze and interpret a portion of the bedrock topography and morphology under the southern ice-sheet in the Ultimi Lobe region. Through this model, several never observed geological structures have been discovered, allowing us to correlate them with some terrestrial processes in glacial environments and to advance some hypotheses about geological events that may have occurred in the past in the UL region.
Overall, the innovative objectives achieved by the present work are as following:

- The creation of a three-dimensional model of the bedrock subsurface in the Ultimi Lobe region using a new algorithm developed by the undersigned and the application of some scripts used to retrieve data from past space missions. This algorithm is tailored to MARSIS data processing and can be used to examine data collected in areas not investigated in this work. Besides, the same principle behind the script could be used to analyze data from other instruments that use the remote radar echo-sounding technique. Furthermore, images and data retrieved through this method may find their application in the training of machine learning algorithms to improve the analysis of this type of data.
- The highlighting of a correlation between the LAPS tectonic structures studied by Grima et al. (2011) and the subsurface bedrock topography. The presence of low-topographies below a group of LAPS analyzed in our work may suggest that they have generated by extensive stress under the gravitational pull, giving rise to distensive structures within the ice-sheet (i.e., listric faults). Another hypothesis is that the weight of the ice-cap itself caused the collapse of pre-existing scarps in the bedrock, propagating normal faults in the ice-cap. We can also suppose that the sliding of a portion of the ice-cap over the underlying rough topography, may have been triggered the stress.
- The definition of macroscale glacial-like structures on the western portion of our DEM surface. In particular, the presence of a possible glacial valley and a series of elongated-streamlined morphologies (SE-NW oriented) on its floor may suggest a past glacial motion northward. On Earth, the formation of the aforesaid morphologies mostly requires the

presence of meltwater at the ice-sheet base, as Orosei et al. (2018) and Lauro et al. (2021) highlighted in the UL region.

- The definition of the first high-resolution topography around the areal portion surrounding the subsurface "lake district" (Orosei et al., 2018; Lauro et al., 2021). Although it is a first-order result to improve with further analyses, the model highlights several topographic lows consistent with the accumulation of water, contrary to Arnold et al. (2019) and Sori & Bramson (2019) assumptions. Besides, the model shows local thinning of the ice-sheet in correspondence of the same region, as observed, for example, in Antarctica (e.g., Siegert and Ridley, 1998).

In their overall view and net of errors and approximations, all the above-mentioned results seem to indicate that the UL region was affected by sliding of the ice sheet, as suggested by previous works in other parts of the southern pole (e.g., in Promethei Lingula; Guallini et al., 2012). This process could be favored by the presence of water at the base of the ice-sheet under past climate conditions and that locally find some correspondence at present.

The present work can be the starting point for further studies necessary to verify the obtained results and to better understand the inferred geological processes. For example, one could simulate water runoff by calculating hydraulic potential around the "lake district" and through a more in-depth analysis of topographic lows in the region. It is also possible to expand the study area. As already mentioned, the implemented semi-automatic method could be used with radargrams from unconsidered orbits and thus create a model covering a larger area. Also, an improvement in the quality of the buried bedrock could be obtained through the use of 'cleaner' radar signals by the use of more efficient automatic mapping algorithms.

BIBLIOGRAPHY

Albee, A. L., Arvidson, R. E., Palluconi, F., & Thorpe, T. (2001). Overview of the Mars global surveyor mission. *Journal of Geophysical Research: Planets*, *106*(E10), 23291-23316.

Anguita, F., Babín Vich, R. B., Benito, G., Gómez Ortiz, D., Collado, A., & Rice, J. W. (2000). Chasma Australe, Mars: Structural framework for a catastrophic outflow origin. *Icarus (New York, NY 1962)*, *144*, 302-310.

Arnold, N. S., Conway, S. J., Butcher, F. E., & Balme, M. R. (2019). Modeled subglacial water flow routing supports localized intrusive heating as a possible cause of basal melting of Mars' south polar ice cap. *Journal of Geophysical Research: Planets*, *124*(8), 2101-2116.

Arcone, S. A., Lawson, D. E., & Delaney, A. J. (1995). Short-pulse radar wavelet recovery and resolution of dielectric contrasts within englacial and basal ice of Matanuska Glacier, Alaska, USA. *Journal of Glaciology*, *41*(137), 68-86.

Bailey, J. T., Evans, S., & Robin, G. D. Q. (1964). Radio echo sounding of polar ice sheets. *Nature*, *204*(4957), 420-421.

Barlow, N. (2014). Mars: An introduction to its interior, surface and atmosphere. Cambridge University press.

Bass, D. S., Herkenhoff, K. E., & Paige, D. A. (2000). Variability of Mars' north polar water ice cap: I. Analysis of Mariner 9 and Viking Orbiter Imaging data. Icarus, 144(2), 382-396.

Bennett, M. M., & Glasser, N. F. (Eds.). (2011). *Glacial geology: ice sheets and landforms*. John Wiley & Sons.

Boissonnat, J. D., & Cazals, F. (2002). Smooth surface reconstruction via natural neighbour interpolation of distance functions. *Computational Geometry*, *22*(1-3), 185-203.

Brothers, T. C., Holt, J. W., & Spiga, A. (2015). Planum Boreum basal unit topography, Mars: Irregularities and insights from SHARAD. Journal of Geophysical Research: Planets, 120(7), 1357-1375.

Byrne, S., & Ingersoll, A. P. (2003). A sublimation model for Martian south polar ice features. *Science*, *299*(5609), 1051-1053.

Carr, M. H. (1981). The Surface of Mars: Yale University Press. New Haven, Connecticut.

Chicarro, A., Martin, P., & Trautner, R. (2004, August). The Mars Express mission: an overview. In *Mars Express: The Scientific Payload* (Vol. 1240, pp. 3-13).

Choudhury, B.J., and A.T.C. Chang. 1979. Two-stream theory of reflectance of snow. IEEE Transactions on Geoscience Electronics GE17:63–68.

Cutts, J. A., & Lewis, B. H. (1982). Models of climate cycles recorded in Martian polar layered deposits. Icarus, 50(2-3), 216-244.

Dollfus, A., Ebisawa, S., & Crussaire, D. (1996). Hoods, mists, frosts, and ice caps at the poles of Mars. Journal of Geophysical Research: Planets, 101(E4), 9207-9225.

Dowdeswell, J.A. and S. Evans (2004). Investigations of the form and flow of ice sheets and glaciers using radio-echo sounding. Reports on Progress in Physics 67, 1821–1861.

Drewry, D. J. (1981). Radio echo sounding of ice masses- Principles and applications. *Remote sensing in meteorology, oceanography and hydrology. (A 82-42134 21-43) Chichester, Sussex, England, Ellis Horwood, Ltd.*, 270-284.

Fishbaugh, K. E., & Head III, J. W. (2000). Current Issues in Mars Polar Research: Using MOLA Data to Computer the Martian Polar Caps. *mpse*, (1057), 38.

Fishbaugh, K. E., & Head III, J. W. (2001). Comparison of the north and south polar caps of Mars: New observations from MOLA data and discussion of some outstanding questions. *Icarus*, *154*(1), 145-161.

Fishbaugh, K. E., & Head III, J. W. (2001). Comparison of the north and south polar caps of Mars: New observations from MOLA data and discussion of some outstanding questions. Icarus, 154(1), 145-161.

Fishbaugh, K. E., Hvidberg, C. S., Beaty, D., Clifford, S., Fisher, D., Haldemann, A., ... & Ammann, W. J. (2008). Introduction to the 4th Mars Polar Science and Exploration Conference special issue: Five top questions in Mars polar science.

Fisher, D. A. (1993). If Martian ice caps flow: Ablation mechanisms and appearance. *Icarus*, *105*(2), 501-511.

Fisher, D. A. (2000). Internal layers in an "accublation" ice cap: A test for flow. *Icarus*, *144*(2), 289-294.

Folkner, W. M., Yoder, C. F., Yuan, D. N., Standish, E. M., & Preston, R. A. (1997). Interior structure and seasonal mass redistribution of Mars from radio tracking of Mars Pathfinder. Science, 278(5344), 1749-1752.

Forget, F., Hourdin, F., & Talagrand, O. (1998). CO2Snowfall on Mars: Simulation with a General Circulation Model. *Icarus*, *131*(2), 302-316.

Fujita, S., & Mae, S. (1993). Relation between ice sheet internal radio-echo reflections and ice fabric at Mizuho Station, Antarctica. *Annals of Glaciology*, *17*, 269-275.

Fujita, S., Mae, S., & Matsuoka, T. (1993). Dielectric anisotropy in ice Ih at 9.7 GHz. *Annals of Glaciology*, *17*, 276-280.

Fujita, S., Matsuoka, T., Ishida, T., Matsuoka, K., & Mae, S. (2000). A summary of the complex dielectric permittivity of ice in the megahertz range and its applications for radar sounding of polar ice sheets. In *Physics of ice core records* (pp. 185-212). Hokkaido University Press.

Gimond, M. 'Intro to GIS and Spatial analysis'. https://mgimond.github.io/Spatial/index.html

Glen, J. W., & Paren, J. G. (1975). The electrical properties of snow and ice. *Journal of Glaciology*, *15*(73), 15-38.

Greve, R. (2008). The polar ice caps of Mars. *低温科学*, *66*, 139-148.

Grima, C., Costard, F., Kofman, W., Saint-Bézar, B., Servain, A., Rémy, F., ... & Seu, R. (2011). Large asymmetric polar scarps on Planum Australe, Mars: Characterization and evolution. *Icarus*, *212*(1), 96-109.

Grima, C., Kofman, W., Mouginot, J., Phillips, R. J., Hérique, A., Biccari, D., ... & Cutigni, M. (2009). North polar deposits of Mars: Extreme purity of the water ice. Geophysical Research Letters, 36(3).

Guallini, L., F. Brozzetti & L. Marinangeli (2012), Large-scale deformational systems in the South Polar Layered Deposits (Promethei Lingula, Mars): "Soft-sediment" and Deep-Seated Gravitational Slope Deformations Mechanisms, Icarus, Volume 220, Issue 2, Pages 821-843, ISSN 0019-1035, https://doi.org/10.1016/j.icarus.2012.06.023.

Hale, A. S., Bass, D. S., & Tamppari, L. K. (2005). Monitoring the perennial Martian northern polar cap with MGS MOC. Icarus, 174(2), 502-512.

Hansen, C. J., Thomas, N., Portyankina, G., McEwen, A., Becker, T., Byrne, S., ... & Mellon, M. (2010). HiRISE observations of gas sublimation-driven activity in Mars' southern polar regions: I. Erosion of the surface. *Icarus*, *205*(1), 283-295.

Head III, J. W., & Pratt, S. (2001). Extensive Hesperian-aged south polar ice sheet on Mars: Evidence for massive melting and retreat, and lateral flow and ponding of meltwater. Journal of Geophysical Research: Planets, 106(E6), 12275-12299.

Head, J. W., Hiesinger, H., Ivanov, M. A., Kreslavsky, M. A., Pratt, S., & Thomson, B. J. (1999). Possible ancient oceans on Mars: evidence from Mars Orbiter Laser Altimeter data. *Science*, *286*(5447), 2134-2137.

Heggy E. et al., in 4th International Conference on Mars Polar Science and Exploration (Lunar and Planetary Institute, Houston, TX, 2006), abstr. 8105.

Hemsley, R. (2009). Interpolation on a magnetic field. *Tech. Rep.*

Herkenhoff, K. E., & Plaut, J. J. (2000). Surface ages and resurfacing rates of the polar layered deposits on Mars. *Icarus*, *144*(2), 243-253.

Howard, A. D. (2000). The role of eolian processes in forming surface features of the Martian polar layered deposits. *Icarus*, *144*(2), 267-288.

Howard, A. D., Cutts, J. A., & Blasius, K. R. (1982). Stratigraphic relationships within Martian polar cap deposits. *Icarus*, *50*(2-3), 161-215.

Hvidberg, C. S., Fishbaugh, K. E., Winstrup, M., Svensson, A., Byrne, S., & Herkenhoff, K. E. (2012). Reading the climate record of the Martian polar layered deposits. Icarus, 221(1), 405-419.

Ivanov, A. B., & Muhleman, D. O. (2000). The role of sublimation for the formation of the northern ice cap: Results from the Mars Orbiter Laser Altimeter. *Icarus*, *144*(2), 436-448.

James, P. B., & Cantor, B. A. (2001). Martian north polar cap recession: 2000 Mars Orbiter Camera observations. Icarus, 154(1), 131-144.

Jordan, R., Picardi, G., Plaut, J., Wheeler, K., Kirchner, D., Safaeinili, A., ... & Cicchetti, A. (2009). The Mars express MARSIS sounder instrument. *Planetary and Space Science*, *57*(14-15), 1975-1986.

Kieffer, H. H. (1979). Mars south polar spring and summer temperatures: A residual CO2 frost. *Journal of Geophysical Research: Solid Earth*, *84*(B14), 8263-8288.

Kieffer, H. H., & Titus, T. N. (2001). TES mapping of Mars' north seasonal cap. Icarus, 154(1), 162-180.

Kieffer, H. H., Chase, S. C., Martin, T. Z., Miner, E. D., & Palluconi, F. D. (1976). Martian north pole summer temperatures: Dirty water ice. *Science*, *194*(4271), 1341-1344.

Kolb, E. J., & Tanaka, K. L. (2001). Geologic history of the polar regions of Mars based on Mars Global Surveyor data: II. Amazonian Period. *Icarus*, *154*(1), 22-39.

Kreslavsky, M. A., & Head, J. W. (2005). Mars at very low obliquity: Atmospheric collapse and the fate of volatiles. Geophysical research letters, 32(12).

Langevin, Y., Poulet, F., Bibring, J. P., Schmitt, B., Douté, S., & Gondet, B. (2005). Summer evolution of the north polar cap of Mars as observed by OMEGA/Mars express. Science, 307(5715), 1581-1584.

Laskar, J., & Robutel, P. (1993). The chaotic obliquity of the planets. Nature, 361(6413), 608-612.

Laskar, J., Correia, A. C. M., Gastineau, M., Joutel, F., Levrard, B., & Robutel, P. (2004). Long term evolution and chaotic diffusion of the insolation quantities of Mars. Icarus, 170(2), 343-364.

Laskar, J., Levrard, B., & Mustard, J. F. (2002). Orbital forcing of the

Lauro, S. E., Pettinelli, E., Caprarelli, G., Guallini, L., Rossi, A. P., Mattei, E., ... & Orosei, R. (2021). Multiple subglacial water bodies below the south pole of Mars unveiled by new MARSIS data. *Nature Astronomy*, *5*(1), 63-70.

Liu, C., Ye, H., & Jin, Y. Q. (2014, August). Inversion of dielectric constant of Mars south polar region using the MARSIS data. In *2014 XXXIth URSI General Assembly and Scientific Symposium (URSI GASS)* (pp. 1-3). IEEE.

Malin, M. C., & Edgett, K. S. (2001). Mars global surveyor Mars orbiter camera: interplanetary cruise through primary mission. Journal of Geophysical Research: Planets, 106(E10), 23429-23570.

Martinec, J. 1977. Expected snow loads on structures from incomplete hydrological data. Journal of Glaciology 19 (81):185–195.

Mattei, E., Lauro, S. E., Vannaroni, G., Cosciotti, B., Bella, F., & Pettinelli, E. (2014). Dielectric measurements and radar attenuation estimation of ice/basalt sand mixtures as martian Polar Caps analogues. *Icarus*, *229*, 428-433.

Mellon, M. T., & Jakosky, B. M. (1995). The distribution and behavior of Martian ground ice during past and present epochs. Journal of Geophysical Research: Planets, 100(E6), 11781-11799.

Mesick, K. E., & Feldman, W. C. (2020). Variability in Mars' North Seasonal CO2 Polar Cap Observed by the Mars Odyssey Neutron Spectrometer from MY 26-34. *LPI*, (2326), 2755.

mgimond.github.io/Spatial/index.html

Mischna, M. A., Richardson, M. I., Wilson, R. J., & McCleese, D. J. (2003). On the orbital forcing of Martian water and CO2 cycles: A general circulation model study with simplified volatile schemes. Journal of Geophysical Research: Planets, 108(E6).

Mouginot, J., Kofman, W., Safaeinili, A., Grima, C., Hérique, A., & Plaut, J. J. (2009). MARSIS surface reflectivity of the south residual cap of Mars. *Icarus*, *201*(2), 454-459.

Mouginot, J., Kofman, W., Safaeinili, A., Hérique, A., Plaut, J., Picardi, G., & Grima, C. (2008). Thickness of south polar residual cap of mars by MARSIS. *cosp*, *37*, 2117.

Nye, J. F., Durham, W. B., Schenk, P. M., & Moore, J. M. (2000). The instability of a south polar cap on Mars composed of carbon dioxide. *Icarus*, *144*(2), 449-455.

Ojha, L., Nerozzi, S., & Lewis, K. (2019). Compositional constraints on the north polar cap of Mars from gravity and topography. Geophysical Research Letters, 46(15), 8671-8679.

Orosei, R., Lauro, S. E., Pettinelli, E., Cicchetti, A., Coradini, M., Cosciotti, B., ... & Soldovieri, F. (2018). Radar evidence of subglacial liquid water on Mars. *Science*, *361*(6401), 490-493.

Paige, D. A., Herkenhoff, K. E., & Murray, B. C. (1990). Mariner 9 observations of the south polar cap of Mars: Evidence for residual CO2 frost. *Journal of Geophysical Research: Solid Earth*, *95*(B2), 1319-1335.

Pellikka, P., & Rees, W. G. (Eds.). (2009). *Remote sensing of glaciers: techniques for topographic, spatial and thematic mapping of glaciers*. CRC press.

Picardi, G., Plaut, J. J., Biccari, D., Bombaci, O., Calabrese, D., Cartacci, M., ... & Federico, C. (2005). Radar soundings of the subsurface of Mars. science, 310(5756), 1925-1928.

Plaut, J. J., Picardi, G., Safaeinili, A., Ivanov, A. B., Milkovich, S. M., Cicchetti, A., ... & Clifford, S. M. (2007). Subsurface radar sounding of the south polar layered deposits of Mars. *science*, *316*(5821), 92-95.

Plewes, L. A., & Hubbard, B. (2001). A review of the use of radio-echo sounding in glaciology. *Progress in Physical Geography*, *25*(2), 203-236.

Putzig, N. E., Smith, I. B., Perry, M. R., Foss II, F. J., Campbell, B. A., Phillips, R. J., & Seu, R. (2018). Three-dimensional radar imaging of structures and craters in the Martian polar caps. *Icarus*, *308*, 138-147.

Rees, W. G. (2005). *Remote sensing of snow and ice*. CRC press.

Reynolds, J. M. (1997). *An introduction to applied and environmental geophysics*. Chichester: Wiley.

Saunders, R. S., Arvidson, R. E., Badhwar, G. D., Boynton, W. V., Christensen, P. R., Cucinotta, F. A., ... & Mase, R. A. (2004). 2001 Mars Odyssey mission summary. *Space Science Reviews*, *110*(1-2), 1-36.

Seeber, G. (2003). Satellite Geodesy, 2nd completely revised and extended edition. *Walter de Gruyter GmbH & Co. KG*, *10785*, 303-304.

Sibson, R. (1981). "A brief description of natural neighbor interpolation (Chapter 2)". In V. Barnett (ed.). *Interpreting Multivariate Data*. Chichester: John Wiley. pp. 21–36.

Siegert, M. J., & Ridley, J. K. (1998). An analysis of the ice-sheet surface and subsurface topography above the Vostok Station subglacial lake, central East Antarctica. *Journal of Geophysical Research: Solid Earth*, *103*(B5), 10195-10207.

Smith, D. E., & Zuber, M. T. (1999, September). The relationship of the MOLA topography of Mars to the mean atmospheric pressure. In *Bulletin of the American Astronomical Society* (Vol. 31, p. 1178).

Smith, D. E., Zuber, M. T., Frey, H. V., Garvin, J. B., Head, J. W., Muhleman, D. O., ... & Banerdt, W. B. (2001). Mars Orbiter Laser Altimeter: Experiment summary after the first year of global mapping of Mars. *Journal of Geophysical Research: Planets*, *106*(E10), 23689-23722.

Smith, D. E., Zuber, M. T., Solomon, S. C., Phillips, R. J., Head, J. W., Garvin, J. B., ... & Lemoine, F. G. (1999). The global topography of Mars and implications for surface evolution. *science*, *284*(5419), 1495-1503.

Sori, M. M., & Bramson, A. M. (2019). Water on Mars, with a grain of salt: Local heat anomalies are required for basal melting of ice at the south pole today. *Geophysical Research Letters*, *46*(3), 1222-1231.

Stevens, K. W. (2007). The Encyclopedia of Astrobiology, Astronomy, and Spaceflight: An Alphabetical Guide to the Living Universe. *Reference Reviews*.

Tanaka, K. L., & Kolb, E. J. (2001). Geologic history of the polar regions of Mars based on Mars Global Surveyor Data: I. Noachian and Hesperian Periods. *Icarus*, *154*(1), 3-21.

Tanaka, K. L., & Scott, D. H. (1987). *Geologic map of the polar regions of Mars*. The Survey.

Thomas, P. C., Malin, M. C., Edgett, K. S., Carr, M. H., Hartmann, W. K., Ingersoll, A. P., ... & Sullivan, R. (2000). North–south geological differences between the residual polar caps on Mars. *Nature*, *404*(6774), 161-164.

Thomas, P. C., Malin, M. C., Edgett, K. S., Carr, M. H., Hartmann, W. K., Ingersoll, A. P., ... & Sullivan, R. (2000). North–south geological differences between the residual polar caps on Mars. *Nature*, *404*(6774), 161-164.

Torge, W., & Müller, J. (2012). *Geodesy*. Walter de Gruyter.

Touma, J., & Wisdom, J. (1993). The chaotic obliquity of Mars. Science, 259(5099), 1294-1297.

Wackernagel, H. (2013). *Multivariate geostatistics: an introduction with applications*. Springer Science & Business Media.

Ward, W. R. (1973). Large-scale variations in the obliquity of Mars. Science, 181(4096), 260-262.

Ward, W. R. (1992). Long-term orbital and spin dynamics of Mars. Mars, 298-320.

Warren, S. G., & Wiscombe, W. J. (1980). A model for the spectral albedo of snow. II: Snow containing atmospheric aerosols. Journal of the Atmospheric Sciences, 37(12), 2734-2745.

Weber, J. R., & Andrieux, P. (1970). Radar soundings on the Penny ice cap, Baffin Island. *Journal of Glaciology*, *9*(55), 49-54.

Yin, A. (2012). Structural analysis of the Valles Marineris fault zone: Possible evidence for large-scale strike-slip faulting on Mars. *Lithosphere*, *4*(4), 286-330.

Zuber, M. T., Smith, D. E., Solomon, S. C., Abshire, J. B., Afzal, R. S., Aharonson, O., ... & Head, J. W. (1998). Observations of the north polar region of Mars from the Mars Orbiter Laser Altimeter. *science*, *282*(5396), 2053-2060.

Zurek, R. W., & Smrekar, S. E. (2007). An overview of the Mars Reconnaissance Orbiter (MRO) science mission. *Journal of Geophysical Research: Planets*, *112*(E5).

APPENDIX

Here below are listed respectively the code implemented by me, two scripts for reading and analysis of MARSIS data and the script for reading the MOLA dataset.

Analisi_radargrammi.m

```
close  all
clearvars
clc

% MARSIS data files are expected to be located in the same directory as the
% script, so that their list can be compiled by issuing the DOS command
% "dir"


filelist = dir;

% scan through the list of files

for i = 1:length(filelist)

% check if the current file is a MARSIS data  files

     if contains( filelist( i ).name, '_SS3_TRK_RAW_M.DAT' )

% read data from file using a dedicated function; only some of  the
% variables in the files are loaded in the program; the complete list can
% be found in the script MARSIS_R_SS3_TRK_RAW.m

          f0 = read_MARSIS_RDR( filelist( i ).name, 'CENTRAL_FREQUENCY' );
          echob1  =  read_MARSIS_RDR(  filelist(  i  ).name,  'ECHO_MODULUS_B1'  );
          echob2 = read_MARSIS_RDR( filelist( i ).name, 'ECHO_MODULUS_B2' );
           lon_0 = read_MARSIS_RDR( filelist( i ).name, 'SUB_SC_LONGITUDE' );
           lat_0 = read_MARSIS_RDR( filelist( i ).name, 'SUB_SC_LATITUDE' );

% data require some cleanup, because the matrixes containing radar echoes
% have sometimes empty columns representing missing echoes; first step is
% finding the index of those columns that are not all  zeroes

          iechob1 = find( sum( echob1 ) );
          iechob2 = find( sum( echob2 )  );

% next step is to remove the empty columns, and also the values  of
% frequency, longitude and latitude corresponding to those empty  columns

          fb1 = f0( 1, iechob1 );
          fb2 = f0( 2, iechob2  );

          echob1 = echob1( :, iechob1 );
          echob2 = echob2( :, iechob2  );

          lonb1 = lon_0( iechob1 );
```

```
        lonb2 = lon_0( iechob2  );

        latb1 = lat_0( iechob1 );
        latb2 = lat_0( iechob2  );

% for the sake of better visualization, echo matrixes are shown  as
% radargrams, which are oversampled to make features more clear, filtered
% to remove some of the background noise, and then converted from a linear
% to a logarithmic scale to enhance weak  echoes

% echo matrixes have 980 rows, which are increased by  a
% factor of 8 through oversampling

        rdrgrmb1 = interpft( echob1, 8 * 980 );
        rdrgrmb2 = interpft( echob2, 8 * 980 );

% usually 80% or more of echo samples are just noise, so we raise the value
% of the lower 50% of the samples to a threshold corresponding to the
% median of echo values

        threshold = median( reshape( rdrgrmb1, 1, [] ) );
        rdrgrmb1( rdrgrmb1 < threshold ) =  threshold;

        threshold = median( reshape( rdrgrmb2, 1, [] ) );
        rdrgrmb2( rdrgrmb2 < threshold ) =  threshold;

% radargrams are now converted in dB to increase the visibility of weak
% echoes

        rdrgrmb1 = 20 .* log10( rdrgrmb1 );
        rdrgrmb2 = 20 .* log10( rdrgrmb2  );

% only the middle strip of the radargram contains echoes, so the upper and
% lower strips are discarded

        rdrgrmb1 = rdrgrmb1( 8 * 350 : 8 * 750, : );
        rdrgrmb2 = rdrgrmb2( 8 * 350 : 8 * 750, : );

% radargrams are displayed
        subplot( 1, 2, 1 ), imagesc( rdrgrmb1 ), colormap  jet
        title( [ filelist( i ).name, ', first band' ], 'Interpreter', 'none' )

        hold off

        subplot( 1, 2, 2 ), imagesc( rdrgrmb2 ), colormap  jet
        title( [ filelist( i ).name, ', second band' ], 'Interpreter', 'none' )

        hold off

%% Study case

       n = input('Press 1 for Low frequency Radargram (Left),Press 2 for High
frequency Radargram (Right): ');

        switch n

            %Evaluation on the Lower frequency Radargram
            case 1
```

```
                fprintf('Click on the image to create the Top surface ')
                [Top_x1, Top_y1] = Surf(rdrgrmb1);
                fprintf('Click on left image to create the Bottom surface  ')
                [Bot_x1, Bot_y1] = Surf(rdrgrmb1);
                %compare the 2 graphs
                plot(Top_x1, Top_y1, 'w','LineWidth',1.5)
                hold on
                plot(Bot_x1, Bot_y1, 'w','LineWidth',1.5)

                %Calculate the thickness of the ice cap, the basal  and
                %superficial elevation of the cap above the ellipsoid
                [Cap_Thickness, Basal_Height, Superficial_Height] =  Thick(Top_y1, ↙
Bot_y1, lonb1, latb1);

                Crdn = Excel(lonb1, latb1, Basal_Height);

               full = fullfile('E:\per_Giacomo\Excell coordinates 2', [filelist( i ).   ⌙
name,'_Coord2.xlsx']);
                xlswrite(full,Crdn);
               full = fullfile('E:\per_Giacomo\Excell coordinates 2', [filelist( i ).   ⌙
name,'_Thick2.xlsx']);
                xlswrite(full,Cap_Thickness);

            %Evaluation on the Higher frequency Radargram
            case 2

                fprintf('Click on the image to create the Top surface ')
                [Top_x2, Top_y2] = Surf(rdrgrmb2);
                fprintf('Click on left image to create the Bottom surface ')
                [Bot_x2, Bot_y2] = Surf(rdrgrmb2);
                %compare the 2 graphs
                plot(Top_x2, Top_y2, 'w','LineWidth',1.5)
                hold on
                plot(Bot_x2, Bot_y2, 'w','LineWidth',1.5)

                %Calculate the thickness of the ice cap, the basal  and
                %superficial elevation of the cap above the ellipsoid
                [Cap_Thickness, Basal_Height, Superficial_Height] =  Thick(Top_y2, ↙
Bot_y2, lonb2, latb2);

                Crdn = Excel(lonb2, latb2, Basal_Height);

               full = fullfile('E:\per_Giacomo\Excell coordinates 2', [filelist( i ).   ⌙
name,'_Coord2.xlsx']);
                xlswrite(full,Crdn);
               full = fullfile('E:\per_Giacomo\Excell coordinates 2', [filelist( i ).   ⌙
name,'_Thick2.xlsx']);
                xlswrite(full,Cap_Thickness);

        end

        % display is paused for a few moments to allow inspection
                pause( 1 )


    end
```

```
end
%% Plotting Function
function [xx, yy] = Surf(rdr)

Col = [];
Rig = [];
click = 0;
punti = 30;

 while click < punti

     delete(subplot(1, 2,  2))
     subplot(1,1,1,gca), imagesc( rdr ), colormap parula
     title('Pick points')
     hold on
     plot(Col, Rig, 'k.')
     Matx = zeros(size(rdr));
     [a, b] = size(Matx);
     [x,y]=ginput(1);
     X = round(x);
     Y = round(y);
     W = (Y-70):(Y+70);

     if min(W) < 1
        W=1:(X+70);
     elseif max(W) > a
            W=(X-70):a;
     end

     for j = W
         Matx(W, X) = rdr(W, X);
     end

     [~, riga] = max(Matx(:,X));
     if riga < W
         riga = Y;
     end
     Col(end + 1) = X;
     Rig(end + 1) = riga;
     click = click + 1;
     plot(Col, Rig, 'r.')
     % Give the possibility to remove the last point chosen by pressing 'z'
     del = input('cancel point? (1) yes, just press return to continue');
     if del == 1
        Col(end) = [];
        Rig(end) = [];
        click = click -  1;
     else
     end

     if click == 15 || click == 20 || click == 25
         beep
         End = input('Are you done? Yes = 1 or No = 2: ');
         if End == 1
             click = punti;
         end
```

```
    end

end

xx = (1:b);
yy = spline(Col,  Rig,xx);
plot(xx, yy, 'w','LineWidth',1.5)
pause(3)

end
%% Calculate thickness and elevations
function [Z, H_bas, H_surf] = Thick(Y_surf, Y_bas, lon,  lat)
%light speed
c = 2.998e5;
%Permittivity
Epsi = 3.5;
%Light speed in our medium
v = c/(Epsi)^(1/2);
%Sampling rate of the Analog to Digital converter
dt = 1/(8*2.8e6);
%Signal travel space for each time interval
ds = (v*dt/2)*1000;
%% Get elevation from MOLA function
%Thickness callculation in Km
Thickness = Y_bas -  Y_surf;
Z = Thickness*ds;
%MOLA elevation function
H_surf = molapolarset(lon,lat,'topography', 512 );
H_bas = H_surf - Z;
end
%% Export Excel
function Coordinates = Excel(lo,la,ze)
Coordinates = zeros(length(ze) + 1,3);
%Longitude
Coordinates(1,1) =  10;
%Latitude
Coordinates(1,2) =  14;
%Z Axys
Coordinates(1,3) =  8;

 for u = 2 : length(ze)+1
     Coordinates(u,1) = lo(1,u-1);
     Coordinates(u,2) = la(1,u-1);
     Coordinates(u,3) = ze(1,u-1);
end
end
```

read_MARSIS_RDR.m

```
function MarsisRdr = read_MARSIS_RDR( RdrFile, ParameterName, StartRecord, StopRecord,  ⌙
```

```
SkipRecords )

if      ~isempty( strfind( RdrFile, '_SS1_TRK_CMP_' ) ) && ~isempty( strfind( RdrFile,
'R_' ) ), disp( 'This type of file cannot be read yet' ),  return
elseif ~isempty( strfind( RdrFile, '_SS3_TRK_CMP_' ) ) && ~isempty( strfind( RdrFile,
'R_' ) ), [ RecordBytes, Parameter, OffsetBytes, OffsetBits, Items, Precision,
OutputPrecision, MachineFormat, ItemBytes, ItemBits ] = MARSIS_R_SS3_TRK_CMP;
elseif ~isempty( strfind( RdrFile, '_SS3_TRK_RAW_' ) ) && ~isempty( strfind( RdrFile,
'R_' ) ), [ RecordBytes, Parameter, OffsetBytes, OffsetBits, Items, Precision,
OutputPrecision, MachineFormat, ItemBytes, ItemBits ] = MARSIS_R_SS3_TRK_RAW;
elseif ~isempty( strfind( RdrFile, '_SS4_TRK_CMP_' ) ) && ~isempty( strfind( RdrFile,
'R_' ) ), disp( 'This type of file cannot be read yet' ),  return
elseif ~isempty( strfind( RdrFile, '_SS5_TRK_CMP_' ) ) && ~isempty( strfind( RdrFile,
'R_' ) ), disp( 'This type of file cannot be read yet' ),  return
else    error( 'read_MARSIS_RDR:FileTypeUnknown', 'File %s does not follow standard
naming conventions, file type could not be determined.', RdrFile  )
end

% The data product file is opened.
fid = fopen( RdrFile, 'r' );

if fid < 0
     error( 'read_MARSIS_RDR:MissingInputFile', ...
            'The required data product file %s could not be opened.', ...
             RdrFile )
end

% The length in bytes of the data product file is retrieved, and divided by
% the length of a file record in bytes to obtain the number of records in
% the file.

fseek( fid, 0, 'eof' );
FileBytes = ftell( fid  );
FileRecords = FileBytes / RecordBytes;

 if round( FileRecords ) ~= FileRecords
     fclose( fid );
     error( 'read_MARSIS_RDR:FractionalNumberOfRecords', ...
           'The data product file %s contains %f records, a non integer number of
records.', ...
             RdrFile, FileRecords )
end

% If the only input argument is the name of a data product file, the
% function returns the number of records contained in that file.
if nargin == 1
     MarsisRdr = FileRecords;
     fclose( fid );
     return
end


% The name of the parameter to be extracted from the data product file is
% compared to the list of parameters in the data product, to determine its% position in the
list.
ParameterIndex = strcmp( Parameter, ParameterName );
ParameterIndex = find( ParameterIndex == 1  );
```

```
 if isempty( ParameterIndex )
     fclose( fid );
     error( 'read_MARSIS_RDR:ParameterNotFound', ...
           'The parameter %s is not listed among those contained in a MARSIS RDR FRM ↙
data product.', ...
            ParameterName )
end

% If input values are not provided, default values are assigned  to
% StartRecord, StopRecord and SkipRecords
if nargin < 3
     StartRecord = 1;
end

if nargin < 4
     StopRecord   = FileRecords;
end

if nargin < 5
     SkipRecords = 1;
end

% StartRecord, StopRecord and SkipRecords are checked for consistency.
if StartRecord < 1 || StartRecord >  FileRecords
     fclose( fid );
     error( 'read_MARSIS_RDR:InvalidValueForStartRecord', ...
           'The first record to be extracted is record %g, which is outside the valid ↙
interval [ 1, %g ].', ...
            StartRecord, FileRecords )
end

 if  StopRecord  < 1  || StopRecord   > FileRecords
     fclose( fid );
     error( 'read_MARSIS_RDR:InvalidValueForStopRecord', ...
           'The last record to be extracted is record %g, which is outside the valid ↙
interval [ 1, %g ].', ...
            StopRecord, FileRecords )
end

 if SkipRecords < 1 || SkipRecords > FileRecords
     fclose( fid );
     error( 'read_MARSIS_RDR:InvalidValueForSkipRecords', ...
           'The number of records to be skipped is %g, which is outside the valid ↙
interval [ 1, %g ].', ...
            SkipRecords, FileRecords )
end

 if  StopRecord  < StartRecord
     fclose( fid );
     error( 'read_MARSIS_RDR:StopRecordBeforeStartRecord', ...
           'The first record to be extracted is record %g and is greater than last ↙
  record to be extracted, which is record %g.', ...
            StartRecord, StopRecord )
end

% the number of records to be extracted fromn the data product file is
```

```
% determined.
Records = length( StartRecord : SkipRecords : StopRecord  );

 if Records == 0
     fclose( fid );
     error( 'read_MARSIS_RDR:NoRecordsExtracted', ...
           'The combination of StartRecord = %g, StopRecord = %g, SkipRecords = %g
does not allow the extraction of records from this data product file.', ...
             StartRecord, StopRecord, SkipRecords )
end

% The requested parameter is extracted from the data product  file.

offset = ( StartRecord - 1 ) * RecordBytes + OffsetBytes( ParameterIndex );
fseek( fid, offset, 'bof' );

pad = fread( fid, OffsetBits( ParameterIndex ), 'ubit1', MachineFormat{ ParameterIndex
} );

size            = [ Items( ParameterIndex ), Records  ];
precision       = [ int2str( Items( ParameterIndex ) ), '*', Precision{ ParameterIndex
}, '=>', OutputPrecision{ ParameterIndex } ];

 if      ( ItemBytes( ParameterIndex ) >= 1 ) && ( ItemBits( ParameterIndex ) == 0 )
     skip       = ( SkipRecords - 1 )  * RecordBytes      + RecordBytes       - Items(
ParameterIndex ) * ItemBytes( ParameterIndex );
 elseif ( ItemBytes( ParameterIndex ) == 0 ) && ( ItemBits( ParameterIndex ) >= 1 )
     skip       = ( SkipRecords - 1 ) * RecordBytes * 8 + RecordBytes * 8   - Items(
ParameterIndex ) *    ItemBits( ParameterIndex );
else


...error( 'read_MARSIS_RDR:WrongParameterFormat', ...
        'The parameter %s is described as being %g bytes long and %g bits long.',

         Parameter{ ParameterIndex }, ItemBytes( ParameterIndex ),  ItemBits(
ParameterIndex ) )
end

machineformat = MachineFormat{ ParameterIndex };

MarsisRdr = fread( fid, size, precision, skip, machineformat );

fclose( fid );
```

MARSIS_R_SS3_TRK_RAW.m

```
function [ RecordBytes, Parameter, OffsetBytes, OffsetBits, Items, Precision,
OutputPrecision, MachineFormat, ItemBytes, ItemBits ] = MARSIS_R_SS3_TRK_RAW

RecordBytes = 15927;

Parameter        = cell( 30, 1  );
Precision        = cell( 30, 1  );
```

```
OutputPrecision = cell( 30, 1  );
MachineFormat     = cell( 30, 1  );

Parameter{ 01  } =            'CENTRAL_FREQUENCY'; OffsetBytes( 01 ) = 00000; OffsetBits( 
01 ) = 0; Items( 01 ) = 002; Precision{ 01 } = 'float32'; OutputPrecision{ 01 } = 
'float32'; MachineFormat{ 01 } = 'ieee-le'; ItemBytes( 01 ) = 4; ItemBits( 01 ) = 0;
Parameter{ 02  } =                         'SLOPE'; OffsetBytes( 02 ) = 00008; OffsetBits( 
02 ) = 0; Items( 02 ) = 001; Precision{ 02 } = 'float32'; OutputPrecision{ 02 } = 
'float32'; MachineFormat{ 02 } = 'ieee-le'; ItemBytes( 02 ) = 4; ItemBits( 02 ) = 0;
Parameter{ 03  } =             'SCET_FRAME_WHOLE'; OffsetBytes( 03 ) = 00012; OffsetBits( 
03 ) = 0; Items( 03 ) = 001; Precision{ 03  } =    'uint32'; OutputPrecision{ 03 } = 
'uint32'; MachineFormat{ 03 } = 'ieee-le'; ItemBytes( 03 ) = 4; ItemBits( 03 ) = 0;
Parameter{ 04  } =              'SCET_FRAME_FRAC'; OffsetBytes( 04 ) = 00016; OffsetBits( 
04 ) = 0; Items( 04 ) = 001; Precision{ 04  } =    'uint16'; OutputPrecision{ 04 } = 
'uint16'; MachineFormat{ 04 } = 'ieee-le'; ItemBytes( 04 ) = 2; ItemBits( 04 ) = 0;
Parameter{ 05  } =                   'H_SCET_PAR'; OffsetBytes( 05 ) = 00018; OffsetBits( 
05 ) = 0; Items( 05 ) = 001; Precision{ 05 } = 'float32'; OutputPrecision{ 05 } = 
'float32'; MachineFormat{ 05 } = 'ieee-le'; ItemBytes( 05 ) = 4; ItemBits( 05 ) = 0;
Parameter{ 06  } =                  'VT_SCET_PAR'; OffsetBytes( 06 ) = 00022; OffsetBits( 
06 ) = 0; Items( 06 ) = 001; Precision{ 06 } = 'float32'; OutputPrecision{ 06 } = 
'float32'; MachineFormat{ 06 } = 'ieee-le'; ItemBytes( 06 ) = 4; ItemBits( 06 ) = 0;
Parameter{ 07  } =                  'VR_SCET_PAR'; OffsetBytes( 07 ) = 00026; OffsetBits( 
07 ) = 0; Items( 07 ) = 001; Precision{ 07 } = 'float32'; OutputPrecision{ 07 } = 
'float32'; MachineFormat{ 07 } = 'ieee-le'; ItemBytes( 07 ) = 4; ItemBits( 07 ) = 0;
Parameter{ 08  } =             'DELTA_S_SCET_PAR'; OffsetBytes( 08 ) = 00030; OffsetBits( 
08 ) = 0; Items( 08 ) = 001; Precision{ 08 } = 'float32'; OutputPrecision{ 08 } = 
'float32'; MachineFormat{ 08 } = 'ieee-le'; ItemBytes( 08 ) = 4; ItemBits( 08 ) = 0;
Parameter{ 09  } =                  'NA_SCET_PAR'; OffsetBytes( 09 ) = 00034; OffsetBits( 
09 ) = 0; Items( 09 ) = 002; Precision{ 09  } =    'uint16'; OutputPrecision{ 09 } = 
'uint16'; MachineFormat{ 09 } = 'ieee-le'; ItemBytes( 09 ) = 2; ItemBits( 09 ) = 0;
Parameter{ 10  } =              'ECHO_MODULUS_B1'; OffsetBytes( 10 ) = 00038; OffsetBits(
 10 ) = 0; Items( 10 ) = 980; Precision{ 10 } = 'float32'; OutputPrecision{ 10 } = 
 'float32'; MachineFormat{ 10 } = 'ieee-le'; ItemBytes( 10 ) = 4; ItemBits( 10 ) = 0;
 Parameter{ 11  } =                'ECHO_PHASE_B1'; OffsetBytes( 11 ) = 03958; OffsetBits(
 11 ) = 0; Items( 11 ) = 980; Precision{ 11 } = 'float32'; OutputPrecision{ 11 } = 
 'float32'; MachineFormat{ 11 } = 'ieee-le'; ItemBytes( 11 ) = 4; ItemBits( 11 ) = 0;
 Parameter{ 12  } =              'ECHO_MODULUS_B2'; OffsetBytes( 12 ) = 07878; OffsetBits(
 12 ) = 0; Items( 12 ) = 980; Precision{ 12 } = 'float32'; OutputPrecision{ 12 } = 
 'float32'; MachineFormat{ 12 } = 'ieee-le'; ItemBytes( 12 ) = 4; ItemBits( 12 ) = 0;
 Parameter{ 13  } =                'ECHO_PHASE_B2'; OffsetBytes( 13 ) = 11798; OffsetBits(
 13 ) = 0; Items( 13 ) = 980; Precision{ 13 } = 'float32'; OutputPrecision{ 13 } = 
 'float32'; MachineFormat{ 13 } = 'ieee-le'; ItemBytes( 13 ) = 4; ItemBits( 13 ) = 0;
 Parameter{ 14  } =     'GEOMETRY_EPHEMERIS_TIME'; OffsetBytes( 14 ) = 15718; OffsetBits(
 14 ) = 0; Items( 14 ) = 001; Precision{ 14 } = 'float64'; OutputPrecision{ 14 } = 
 'float64'; MachineFormat{ 14 } = 'ieee-le'; ItemBytes( 14 ) = 8; ItemBits( 14 ) = 0;
 Parameter{ 15  } =              'GEOMETRY_EPOCH'; OffsetBytes( 15 ) = 15726; OffsetBits(
 15 ) = 0; Items( 15 ) = 023; Precision{ 15  } =     'char'; OutputPrecision{ 15 } = 
 'char'; MachineFormat{ 15 } = 'ieee-le'; ItemBytes( 15 ) = 1; ItemBits( 15 ) = 0;
 Parameter{ 16  } =        'MARS_SOLAR_LONGITUDE'; OffsetBytes( 16 ) = 15749;
 OffsetBits(
 16 ) = 0; Items( 16 ) = 001; Precision{ 16 } = 'float64'; OutputPrecision{ 16 } = 
 'float64'; MachineFormat{ 16 } = 'ieee-le'; ItemBytes( 16 ) = 8; ItemBits( 16 ) = 0;
 Parameter{ 17  } =           'MARS_SUN_DISTANCE'; OffsetBytes( 17 ) = 15757; OffsetBits(
 17 ) = 0; Items( 17 ) = 001; Precision{ 17 } = 'float64'; OutputPrecision{ 17 } = 
```

```
'float64'; MachineFormat{ 17 } = 'ieee-le'; ItemBytes( 17 ) = 8; ItemBits( 17 ) = 0;
Parameter{ 18 } =                'ORBIT_NUMBER'; OffsetBytes( 18 ) = 15765;   OffsetBits(
18 ) = 0; Items( 18 ) = 001; Precision{ 18  } =  'uint32'; OutputPrecision{ 18 } =
'uint32'; MachineFormat{ 18 } = 'ieee-le'; ItemBytes( 18 ) = 4; ItemBits( 18 ) = 0;
Parameter{ 19 } =                 'TARGET_NAME'; OffsetBytes( 19 ) = 15769;   OffsetBits(⌙
19 ) = 0; Items( 19 ) = 006; Precision{ 19  } =    'char'; OutputPrecision{ 19 } = ↙
'char'; MachineFormat{ 19 } = 'ieee-le'; ItemBytes( 19 ) = 1; ItemBits( 19 ) = 0;
Parameter{ 20 } =  'TARGET_SC_POSITION_VECTOR'; OffsetBytes( 20 ) = 15775; OffsetBits(⌙
20 ) = 0; Items( 20 ) = 003; Precision{ 20 } = 'float64'; OutputPrecision{ 20 } =  ↙
'float64'; MachineFormat{ 20 } = 'ieee-le'; ItemBytes( 20 ) = 8; ItemBits( 20 ) = 0;
Parameter{ 21 } =        'SPACECRAFT_ALTITUDE'; OffsetBytes( 21 ) = 15799; OffsetBits(⌙
21 ) = 0; Items( 21 ) = 001; Precision{ 21 } = 'float64'; OutputPrecision{ 21 } =  ↙
'float64'; MachineFormat{ 21 } = 'ieee-le'; ItemBytes( 21 ) = 8; ItemBits( 21 ) = 0;
Parameter{ 22 } =           'SUB_SC_LONGITUDE'; OffsetBytes( 22 ) = 15807; OffsetBits(⌙
22 ) = 0; Items( 22 ) = 001; Precision{ 22 } = 'float64'; OutputPrecision{ 22 } =  ↙
'float64'; MachineFormat{ 22 } = 'ieee-le'; ItemBytes( 22 ) = 8; ItemBits( 22 ) = 0;
Parameter{ 23 } =            'SUB_SC_LATITUDE'; OffsetBytes( 23 ) = 15815; OffsetBits(⌙
23 ) = 0; Items( 23 ) = 001; Precision{ 23 } = 'float64'; OutputPrecision{ 23 } =  ↙
'float64'; MachineFormat{ 23 } = 'ieee-le'; ItemBytes( 23 ) = 8; ItemBits( 23 ) = 0;
Parameter{ 24 } =  'TARGET_SC_VELOCITY_VECTOR'; OffsetBytes( 24 ) = 15823; OffsetBits(⌙
24 ) = 0; Items( 24 ) = 003; Precision{ 24 } = 'float64'; OutputPrecision{ 24 } =  ↙
'float64'; MachineFormat{ 24 } = 'ieee-le'; ItemBytes( 24 ) = 8; ItemBits( 24 ) = 0;
Parameter{ 25 } =  'TARGET_SC_RADIAL_VELOCITY'; OffsetBytes( 25 ) = 15847; OffsetBits(⌙
25 ) = 0; Items( 25 ) = 001; Precision{ 25 } = 'float64'; OutputPrecision{ 25 } =  ↙
'float64'; MachineFormat{ 25 } = 'ieee-le'; ItemBytes( 25 ) = 8; ItemBits( 25 ) = 0;
Parameter{ 26 } =    'TARGET_SC_TANG_VELOCITY'; OffsetBytes( 26 ) = 15855; OffsetBits(⌙
26 ) = 0; Items( 26 ) = 001; Precision{ 26 } = 'float64'; OutputPrecision{ 26 } =  ↙
'float64'; MachineFormat{ 26 } = 'ieee-le'; ItemBytes( 26 ) = 8; ItemBits( 26 ) = 0;
Parameter{ 27 } =      'LOCAL_TRUE_SOLAR_TIME'; OffsetBytes( 27 ) = 15863; OffsetBits(⌙
27 ) = 0; Items( 27 ) = 001; Precision{ 27 } = 'float64'; OutputPrecision{ 27 } =  ↙
'float64'; MachineFormat{ 27 } = 'ieee-le'; ItemBytes( 27 ) = 8; ItemBits( 27 ) = 0;
Parameter{ 28 } =         'SOLAR_ZENITH_ANGLE'; OffsetBytes( 28 ) = 15871; OffsetBits(⌙
28 ) = 0; Items( 28 ) = 001; Precision{ 28 } = 'float64'; OutputPrecision{ 28 } =  ↙
'float64'; MachineFormat{ 28 } = 'ieee-le'; ItemBytes( 28 ) = 8; ItemBits( 28 ) = 0;
Parameter{ 29 } =         'DIPOLE_UNIT_VECTOR'; OffsetBytes( 29 ) = 15879; OffsetBits(⌙
29 ) = 0; Items( 29 ) = 003; Precision{ 29 } = 'float64'; OutputPrecision{ 29 } =  ↙
'float64'; MachineFormat{ 29 } = 'ieee-le'; ItemBytes( 29 ) = 8; ItemBits( 29 ) = 0;
Parameter{ 30 } =       'MONOPOLE_UNIT_VECTOR'; OffsetBytes( 30 ) = 15903; OffsetBits(⌙
30 ) = 0; Items( 30 ) = 003; Precision{ 30 } = 'float64'; OutputPrecision{ 30 } =  ↙
'float64'; MachineFormat{ 30 } = 'ieee-le'; ItemBytes( 30 ) = 8; ItemBits( 30 ) = 0;
```

molapolarset.m

```
function mola = molapolarset( lon, lat, type, ppd )

% extract a set of points from thr MOLA POLAR  dataset

%% Parameters
%
% The parameters below must be set manually by the user. See under the
% heading "Parameters" in the function help page above for a description.
%

molapath = 'E:\per_Giacomo';


%% Validation of input, setting of internal parameters, opening of input files
%
% An error condition occurs if input arrays containing longitudes  and
% latitudes are neither scalar, vectors nor matrixes, or if they don't have
% the same size.
%

slon = size( lon );
slat = size( lat  );

 if max( size( slon ) ) > 2 || max( size( slat ) ) > 2
     error( 'Molaset:TooManyDimensions', ...
          [ 'Input arrays _lon_ and _lat_ cannot have more than two dimensions.\n', ...
            '_lon_ has %d dimensions, _lat_ has %d dimensions.' ],  ...
             max( size( size( lon ) ) ), max( size( size( lat ) ) )  )

end

if any( slon ~= slat )
     error( 'Molaset:ArraySizeMismatch', ...
          [ 'Input arrays _lon_ and _lat_ do not have the same size.\n', ...
            '_lon_ has size ( %d, %d ), _lat_ has size ( %d, %d ).' ], ...
             slon( 1 ), slon( 2 ), slat( 1 ), slat( 2 )  )

end


%
% Input longitudes and latitudes are checked for consistency  with
% topographic conventions.
```

```
%

 if any( any( lon < 0 ) ) || any( any( lon > 360 ) )
     error( 'Molaset:LongitudesOutOfRange', ...
          [ 'Allowed longitude range is [ 0°, 360° ].\n', ...
            'Input longitude range is [ %d°, %d° ].' ], ...
             min( min( lon ) ), max( max ( lon ) ) )

end

 if any( any( lat < -90 ) ) || any( any( lat > 90 ) )
     error( 'Molaset:LatitudesOutOfRange', ...
          [ 'Allowed latitude range is [ -90°, 90° ].\n', ...
            'Input latitude range is [ %d°, %d° ].' ], ...
             min( min( lat ) ), max( max ( lat ) ) )

end


%
% Input data type and resolution are checked and used to set the values of
% a number of internal parameters and to open input  files.
%
%     id             string contained in file names of different types  of
%                    MOLA EGDR data.
%
%     prec           data format of MOLA EGDR data  samples.
%
%     samplebytes    length in bytes of MOLA EGDR data  samples.
%
%     scalingfact    scaling factor for numerical values read from the  MOLA
%                    EGDR data set.
%
%     valueoffset    offset for numerical values read from the MOLA EGDR  data
%                    set.
%
%     n              number of rows and columns in the topographic grid  of
%                    the selected MOLA MEGDR data  set.
%

 if      strcmpi( type, 'counts'     )
     id          = 'c';
     prec        = 'uint8';
     samplebytes = 1;
     scalingfact =  1;
     valueoffset =  0;

 elseif strcmpi(  type, 'radius'     )
     id          = 'r';
     prec        = 'float32';
     samplebytes = 4;
     scalingfact =  1;
     valueoffset = 3396000;

 elseif strcmpi( type, 'topography' )
     id          = 't';
```

```
     prec        = 'uint16';
     samplebytes = 2;
     scalingfact = 0.25;
     valueoffset = -8000;

     else

error( 'MolaPolarSet:TypeNotFound', ...
     [ 'Permitted values for input string _type_ are ''counts'', ''radius'' and ''topography''.\n', ...
            'Input value is %s.' ], ...
            type )

end

if      ppd == 128
     n       = 10240;

elseif ppd == 256
     n       = 11520;

elseif ppd == 512
     n       = 12288;
else

error( 'MolaPolarSet:ResolutionNotFound', ...
     [ 'Permitted values for input variable _ppd_ are 128, 256 and 512.\n', ... 'Input
       value is %d.' ], ...
       ppd )

end


%
% Input files are opened and a check is made to verify that they have been
% opened correctly.
%

fid( 1 ) = fopen( fullfile( molapath, [ 'meg', id, '_n_', num2str( ppd ), '.img' ] ), 'r', 'ieee-be' );
fid( 2 ) = fopen( fullfile( molapath, [ 'meg', id, '_s_', num2str( ppd ), '.img' ] ), 'r', 'ieee-be' );

if any( any( fid < 0 ) )
     error( 'MolaPolarSet:MissingInputFile', ...
          [ 'One of the required MOLA EGDR files is either missing or corrupted.\n', ...

'Value for parameter _molapath_ is %s.' ], ... molapath )

end


%% Definition of the output data topographic grid
%
% The correspondence between input latitudes and row indexes in the MOLA
% EGDR grid is determined, using formulas derived from the inversion of
```

```
% those presented in
% http://pds-geosciences.wustl.edu/mgs/mgs-m-mola-5-megdr-l3-    ↙
v1/mgsl_300x/catalog/dsmap_polar.cat.
% Because polar MOLA EGDR data sets do not cover the entire range of
% latitudes, row indexes for such latitudes will result in null values.
%

[ rows, cols ] = size( lon );

r = zeros( rows, cols );

r( lat > 0 ) = 360 / pi * tan( ( pi/2 - pi / 180 * lat( lat > 0 ) ) / 2 ); r(
lat < 0 ) = 360 / pi * tan( ( pi/2 + pi / 180 * lat( lat < 0 ) ) / 2 );

x = sign( lat ) .* r .* cos( pi / 180 * lon ); y
=                   r .* sin( pi / 180 * lon  );

I = round( ppd * x + n/2 + 0.5 );
J = round( ppd * y + n/2 + 0.5  );

%
% Preallocation of a block of memory large enough to hold the output array
% _mola_ is performed to speed computations. Because polar MOLA EGDR data
% sets do not cover the entire topographic grid, it is convenient  to
% initialize _mola_ to null values for points for which no data exist.
%

mola    = NaN .* ones( rows, cols );


%% Reading of data from input file(s)

for i = 1 : rows

     for j = 1 : cols

         if I( i, j ) >= 1 && I( i, j ) <= n && J( i, j ) >= 1 && J( i, j ) <= n

%              The file position indicator is set at the beginning of  the
%              data value to be retrieved, remembering that each MOLA  EGDR
%              sample is _samplebytes_ bytes long.

             offset = samplebytes * ( ( I( i, j ) - 1 ) * n + J( i, j ) - 1 );

             if     lat( i, j ) > 0

                 fseek( fid( 1 ), offset, 'bof');
                 mola( i, j ) = fread( fid( 1 ), 1, prec );

             elseif lat( i, j ) < 0

                 fseek( fid( 2 ), offset, 'bof');
                 mola( i, j ) = fread( fid( 2 ), 1, prec  );

             end

         end
```

```
     end
end


%
% Input files are closed.
%

for i = 1 : 2
     fclose( fid( i ) );
end


%
% Values stored in the MOLA EGDR planetary radii and topography files are
% expressed in meters minus an offset, which must be added to obtain the
% correct result.
%

mola = scalingfact * mola + valueoffset;
```